Chapter 4 Neutrino Mixing, Mass Hierarchy and CP Violation

LBNE is designed to address the science of neutrino oscillations with superior sensitivity to many mixing parameters in a single experiment, in particular,

1. precision measurements of the parameters that govern $\nu_\mu \rightarrow \nu_e$ and $\overline{\nu}_\mu \rightarrow \overline{\nu}_e$ oscillations; this includes precision measurement of the third mixing angle θ_{13}, measurement of the CP-violating phase $\delta_{\rm CP}$, and determination of the mass ordering (the sign of Δm^2_{32})
2. precision measurements of $\sin^2 2\theta_{23}$ and $|\Delta m^2_{32}|$ in the $\nu_\mu/\overline{\nu}_\mu$ disappearance channel
3. determination of the θ_{23} octant using combined precision measurements of the $\nu_e/\overline{\nu}_e$ appearance and $\nu_\mu/\overline{\nu}_\mu$ disappearance channels
4. search for nonstandard physics that can manifest itself as differences in higher-precision measurements of ν_μ and $\overline{\nu}_\mu$ oscillations over long baselines

4.1 Experimental Requirements Based on Oscillation Phenomenology

The experimental requirements for designing a neutrino oscillation experiment to simultaneously address neutrino CP violation and the mass hierarchy (MH) can be extrapolated as follows from the phenomenology summarized in Chapter 2:

1. *Phenomenology: An appearance experiment is necessary to extract the CP-violating effects.*

   Experimental requirements:

   - The experiment will probe oscillations of $\nu_{\mu,e} \rightarrow \nu_{e,\mu}$.
   - The experiment will identify ν_e and ν_μ with high efficiency and purity in order to tag (or otherwise know) the flavor of the neutrino before and after flavor transformations.
   - The experiment requires E_ν >100 MeV so that it will be possible to perform flavor-tagging of muon neutrinos using the lepton flavor produced in a charged current (CC) interaction ($\nu_\mu + N \rightarrow \mu N' X$).

2. *Phenomenology: In the three-flavor mixing model, the CP-violating Jarlskog invariant arises in the interference term $P_{\sin\delta}$ as given by Equation 2.15; the oscillation scale where the interference term is maximal is that determined by the mixing between the ν_1 and ν_3 states.*

   Experimental requirements:

   - The experimental baseline and corresponding neutrino energy are chosen according to Equation 2.18 such that L/E equals 510 km/GeV to maximize sensitivity to the CP-violating term in the neutrino flavor mixing.
   - Flavor-tagging of muon neutrinos that can be produced either at the source or after flavor-mixing requires $E_\nu > 100$ MeV; therefore, the experimental baselines over which to measure neutrino oscillations are $L > 50$ km*.

3. *Phenomenology: In the three-flavor model $\nu_{\mu,e} \to \nu_{e,\mu}$ oscillations depend on all parameters in the neutrino mixing matrix as well as on the mass differences, as shown in Equations 2.12 to 2.15.*

   Experimental requirements:

   - The precision with which $\delta_{\rm CP}$ can be determined — and the sensitivity to small CP-violating effects or CP violation outside the three-flavor model — requires precision determination of all the other mixing parameters, preferably in the same experiment. The experiment will be designed so as to minimize dependence on external measurements of the oscillation parameters.

4. *Phenomenology: Observation of CP violation requires the explicit observation of an asymmetry between $P(\nu \to \nu)$ and $P(\overline{\nu} \to \overline{\nu})$.*

   Experimental requirements:

   - The experiment will probe the oscillations of both neutrinos and antineutrinos in an unambiguous way.
   - The experiment will be capable of charge tagging in addition to flavor tagging. Charge tagging can be achieved at detection using the lepton charge and/or at production by selecting beams purely of neutrinos or antineutrinos.
   - The experiment will be capable of resolving degeneracies between matter and CP asymmetries in order to determine the MH. This can be achieved by using a baseline greater than 1,000 km or with measurements probing oscillations over a range of L/E values.

*Neutrino experiments using beams from pion decay-at-rest experiments such as DAEδALUS are exceptions since the $\overline{\nu}_\mu$ production spectrum is well known and only the $\overline{\nu}_e$ flavor after oscillations is tagged through inverse-beta decay. The neutrino energies are ~50 MeV below the CC muon-production threshold.

5. *Phenomenology: CP asymmetries are maximal at the secondary oscillation nodes.*

   Experimental requirements:

   - Coverage of the L/E scale of the secondary oscillation nodes improves experimental sensitivity to small values of $\delta_{\rm CP}$ by enabling measurements of the asymmetry at the secondary nodes where the CP asymmetries are much larger and where there is no degeneracy with the matter asymmetries. The experiment will be performed with a wide-band beam to provide sensitivity to the L/E scale of both the first and second oscillation nodes.
   - The experimental baseline will be >150 km, given that muon flavor tagging is required at either production or detection. The secondary oscillation nodes are located at scales set by Equation 2.18 where $n > 1$. The second oscillation maximum is located at scales given by $L/E \sim$1,500 km/GeV.

Based on the experimental requirements prescribed by the neutrino oscillation phenomenology detailed above, pursuit of the primary science objectives for LBNE dictates the need for a very large mass (10 kt to 100 kt) neutrino detector located at a distance greater than 1,000 km from the neutrino source. This large mass coupled with a powerful wide-band beam and long exposures is required to accumulate enough neutrino interactions — $\mathcal{O}$(1,000) events — to make precision measurements of the parameters that govern the subdominant $\nu_\mu \rightarrow \nu_e$ oscillations. At 1,300 km, the baseline chosen for LBNE, both the first and second oscillation nodes are at neutrino energies > 0.5 GeV, as shown in Figure 4.1. This places both neutrino oscillation nodes in a region that is well matched to the energy spectrum of the high-power conventional neutrino beams that can be obtained using the 60 GeV to 120 GeV Main Injector (MI) proton accelerator at Fermilab.

4.2 Simulation of Neutrino Oscillation Experiments

To evaluate the sensitivity of LBNE and to optimize the experiment design, it is important to accurately predict the neutrino flux produced by the neutrino beamline, the neutrino interaction rate at the far detector, and the far detector performance. This is achieved using Monte Carlo (MC) simulations and the GLoBES [1,2] package. The simulations and experimental assumptions that are used to evaluate the sensitivity of LBNE to neutrino mixing parameters, to the neutrino mass hierarchy (MH) and to CP violation are described in this section.

4.2.1 Expected Signal

The LBNE beamline design, described in Section 3.4, is simulated using Geant4 [3]. The simulated ν_μ spectrum (unoscillated flux $\times$ cross section) at 1,300 km obtained from the LBNE beamline using 80-GeV protons from the MI is shown as the black histogram in Figure 4.1. At this baseline,

there is no degeneracy between matter and CP asymmetries at the first oscillation node where the LBNE neutrino beam spectrum peaks. The wide coverage of the oscillation patterns enables the search for physics beyond the three-flavor model because new physics effects may interfere with the standard oscillations and induce a distortion in the oscillation patterns. As a next-generation neutrino oscillation experiment, LBNE aims to study in detail the spectral shape of neutrino mixing over the range of energies where the mixing effects are largest. This is crucial for advancing the science beyond the current generation of experiments, which depend primarily on rate asymmetries.

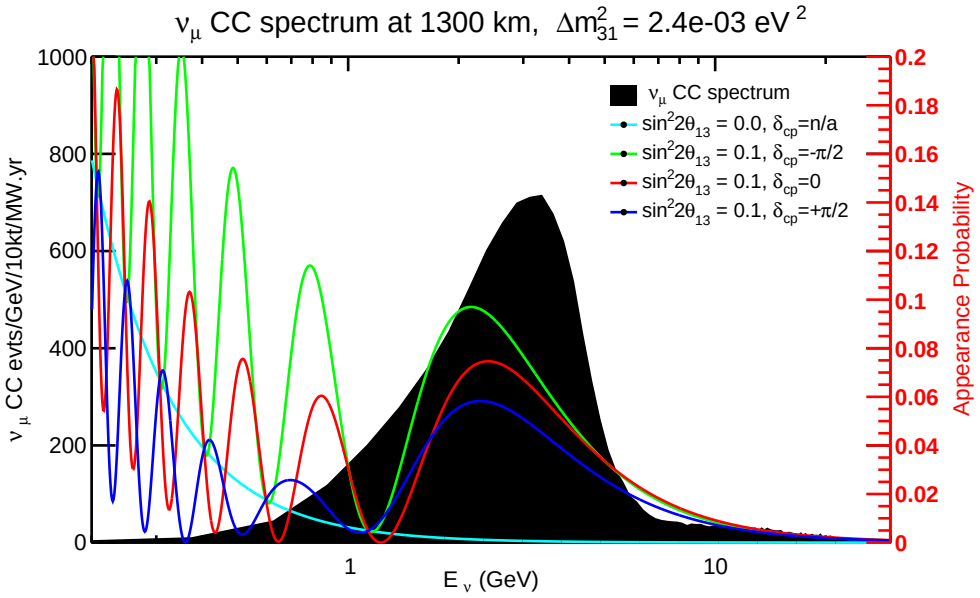

Figure 4.1: The simulated unoscillated spectrum of ν_μ events from the LBNE beam (black histogram) overlaid with the $\nu_\mu \rightarrow \nu_e$ oscillation probabilities (colored curves) for different values of $\delta_{\rm CP}$ and normal hierarchy.

The LBNE reconfiguration study [4] determined that the far detector location at the Sanford Underground Research Facility provides an optimal baseline for precision measurement of neutrino oscillations using a conventional neutrino beam from Fermilab. The 1,300-km baseline optimizes sensitivity to CP violation and is long enough to resolve the MH with a high level of confidence, as shown in Figure 2.7.

Table 4.1 lists the beam neutrino interaction rates for all three known species of neutrinos as expected at the LBNE far detector. This table shows only the raw interaction rates using the neutrino flux from the Geant4 simulations of the LBNE beamline and the default interaction cross sections included in the GLoBeS package [1] with *no detector effects included*. A tunable LBNE beam spectrum, obtained by varying the distance between the target and the first focusing horn (Horn 1), is assumed. The higher-energy tunes are chosen to enhance the ν_τ appearance signal and improve the oscillation fits to the three-flavor paradigm. To estimate the NC event rates based on visible en-

Table 4.1: Raw ν oscillation event rates at the LBNE far site with $E_\nu < 10$ GeV. Assumes 1.8×10^7 seconds/year (Fermilab). *POT* is *protons-on-target*. Oscillation parameters used are: $\theta_{12} = 0.587$, $\theta_{13} = 0.156$, $\theta_{23} = 0.670$, $\Delta m^2_{21} = 7.54 \times 10^{-5}\,\text{eV}^2$, and $\Delta m^2_{31} = +2.47 \times 10^{-3}\,\text{eV}^2$ (normal hierarchy). The NC event rate is for events with visible energy > 0.5 GeV. For comparison, the rates at other neutrino oscillation experiments (current and proposed) are shown for similar exposure in mass and time. No detector effects are included.

Experiment *details*	**Baseline km**	ν_μ **unosc. CC**	ν_μ **osc. CC**	ν_e **beam CC**	ν_μ **NC**	$\nu_\mu \to \nu_\tau$ **CC**	$\nu_\mu \to \nu_e$ **CC** $\delta_{CP} = -\frac{\pi}{2}$,	**0,**	$\frac{\pi}{2}$
LBNE LE	1,300								
80 GeV, 1.2 MW									
1.5 × 10²¹ POT/year									
50 kt · year ν		12721	4339	108	3348	156	605	480	350
50 kt · year $\overline{\nu}$		4248	1392	34	1502	48	51	86	106
LBNE ME	1,300								
120 GeV, 1.2 MW									
1 × 10²¹ POT/year									
50 kt · year ν		19613	12317	72	5808	686	435	399	293
T2K	295								
30 GeV, 750 kW									
9 × 10²⁰ POT/year									
50 kt · year ν		2100	898	41	360	< 1	73	58	39
MINOS LE	735								
120 GeV, 700 kW									
6 × 10²⁰ POT/year									
50 kt · year ν		17574	11223	178	4806	115	345	326	232
50 kt · year $\overline{\nu}$		5607	3350	56	2017	32	58	85	88
NOvA ME	810								
120 GeV, 700 kW									
6 × 10²⁰ POT/year									
50 kt · year ν		4676	1460	74	1188	10	196	168	116
50 kt · year $\overline{\nu}$		1388	428	19	485	2	22	35	41
LBNO	2,300								
50 GeV ∼ 2 MW									
3 × 10²¹ POT/year									
50 kt · year ν		8553	2472	48	2454	570	534	426	336
50 kt · year $\overline{\nu}$		3066	828	15	1140	255	24	45	54
ν-Factory *details*		ν_μ **unosc. CC**	ν_μ **osc. CC**		ν_μ **NC**	$\nu_\mu \to \nu_\tau$ **CC**	$\nu_e \to \nu_\mu$ **CC** $\delta_{CP} = -\frac{\pi}{2}$,	**0,**	$\frac{\pi}{2}$
NuMAX I	1,300								
3 GeV, 1 MW									
0.94 × 10²⁰ μ/year									
50 kt · year μ^+		1039	339		484	28	71	97	117
50 kt · year μ^-		2743	904		945	89	24	19	12
NuMAX II	1,300								
3 GeV, 3 MW									
5.6 × 10²⁰ μ/year									
50 kt · year μ^+		6197	2018		2787	300	420	580	700
50 kt · year μ^-		16349	5390		5635	534	139	115	85

ergies above 0.5 GeV, a true-to-visible energy smearing function based on output from the GENIE neutrino MC generator [5] is used. For comparison, the rates at current neutrino oscillation experiments such as T2K [6], MINOS [7] and NOνA [8] are shown for similar exposure in mass and time and using the same interaction cross sections. The raw interaction rates from other proposed neutrino oscillation experiments such as LBNO [9] and the NuMAX neutrino factory designs [10] are also shown[†]. It is important to note that the duty factors for the JPARC and CERN beams are $\sim 1/3$ and $\sim 1/2$ of NuMI/LBNE respectively. For LBNO, the event rates are obtained using the optimized beam from the HP-PS2 50-GeV synchrotron [11] with an exposure of 3×10^{21} POT/year. The LBNO duty cycle is assumed to be $\sim 10^7$ seconds/year, which corresponds to a beam power of 2 MW. Note that for Stage 1 and Stage 2 of the NuMAX neutrino factory proposal [10], Project X beams [12] at 3 GeV with 1 and 3 MW, respectively, are needed[‡] It is clear that the LBNE beam design and baseline produce high rates of ν_e appearance coupled with large rate asymmetries when CP-violating effects are included. For example, LBNE has significantly higher appearance rates with a Main Injector 1.2-MW beam when compared to Stage 1 of the NuMAX neutrino factory with a 1-MW beam from a 3-GeV linac. The ν_e appearance rates are very similar in LBNE and LBNO with normal hierarchy (NH), but the $\overline{\nu}_e$ appearance rates (NH) in LBNO are $\approx 1/2$ that of LBNE due to the suppression from the larger matter effect (longer baseline) in LBNO.

4.2.2 Detector Simulation using the GLoBES Package

For the sensitivity studies presented here, the GLoBES package [1,2] was used to simulate the detector response using simple smearing and using detector efficiency values based on results from ICARUS and earlier simulation efforts as documented in [13]. The values used in GLoBES are shown in Table 4.2.

Studies from ICARUS have estimated and measured single-particle energy resolutions in liquid argon. Below 50 MeV, the energy resolution of electrons is $11\%/\sqrt{E[\mathrm{MeV}]} + 2\%$. The energy resolution of an electromagnetic shower with energy in the range (50–5000) MeV is $33\%/\sqrt{E(\mathrm{MeV})} + 1\%$ [14] and that of hadronic showers is $\approx 30\%/\sqrt{E(\mathrm{GeV})}$. A significant fraction of the ν_e-CC signal in LBNE in the range of 1 GeV to 6 GeV comes from non-quasi-elastic CC interactions with a large component of the visible energy in the hadronic system. From recent simulations of neutrino interactions in this region it has been determined that $< E_{\mathrm{lepton}}/E_\nu > \approx 0.6$. For this reason, the total ν_e energy resolution for the neutrino oscillation sensitivity calculation is chosen to be $15\%/\sqrt{E(\mathrm{GeV})}$. In a non-magnetized LArTPC, the muon momentum can be obtained from measurements of range and multiple scattering. The muon momentum resolution for partially contained muons is found to be in the range $10 - 15\%$ [15,16] for muons in the 0.5 GeV to 3 GeV

[†]T2K uses a JPARC neutrino beam, MINOS and NOνA use the Fermilab NuMI neutrino beam and LBNO uses a CERN neutrino beam.

[‡]Project X has been superseded by PIP-II as of late 2013; PIP-II is briefly described in Section 3.4.

Table 4.2: Estimated range of the LArTPC detector performance parameters for the primary oscillation physics. Signal efficiencies, background levels, and resolutions are obtained from ICARUS and earlier simulation efforts (middle column) and the value chosen for the baseline LBNE neutrino oscillation sensitivity calculations (right column).

Parameter	Range of Values	Value Used for LBNE Sensitivities
	For ν_e-CC appearance studies	
ν_e-CC efficiency	70-95%	80%
ν_μ-NC misidentification rate	0.4-2.0%	1%
ν_μ-CC misidentification rate	0.5-2.0%	1%
Other background	0%	0%
Signal normalization error	1-5%	1-5%
Background normalization error	2-15%	5-15%
	For ν_μ-CC disappearance studies	
ν_μ-CC efficiency	80-95%	85%
ν_μ-NC misidentification rate	0.5–10%	1%
Other background	0%	0%
Signal normalization error	1-10%	5–10%
Background normalization error	2-20%	10-20%
	For ν-NC disappearance studies	
ν-NC efficiency	70-95%	90%
ν_μ-CC misidentification rate	2-10%	10%
ν_e-CC misidentification rate	1-10%	10%
Other background	0%	0%
Signal normalization error	1-5%	under study
Background normalization error	2-10%	under study
	Neutrino energy resolutions	
ν_e-CC energy resolution	$15\%/\sqrt{E(GeV)}$	$15\%/\sqrt{E(GeV)}$
ν_μ-CC energy resolution	$20\%/\sqrt{E(GeV)}$	$20\%/\sqrt{E(GeV)}$
E_{ν_e} scale uncertainty	under study	under study
E_{ν_μ} scale uncertainty	1-5%	2%

range. The ν_μ total energy resolution in LBNE is, therefore, assumed to be $20\%/\sqrt{E(\mathrm{GeV})}$; the resolution will be significantly better than this for the small subsample of events in which muons are fully contained by the detector.

Figures 4.2 and 4.3 show the predicted spectra of observed signal and background events in LBNE produced from the GLoBES implementation, including the effects of neutrino oscillation. Figure 4.2 shows the ν_μ and $\overline{\nu}_\mu$-CC sample and Figure 4.3 shows the ν_e and $\overline{\nu}_e$-CC appearance sample. Table 4.3 shows the expected LBNE signal and background event rates in ν_μ disappearance and ν_e appearance modes for neutrinos and antineutrinos, for normal (NH) and inverted (IH) hierarchy.

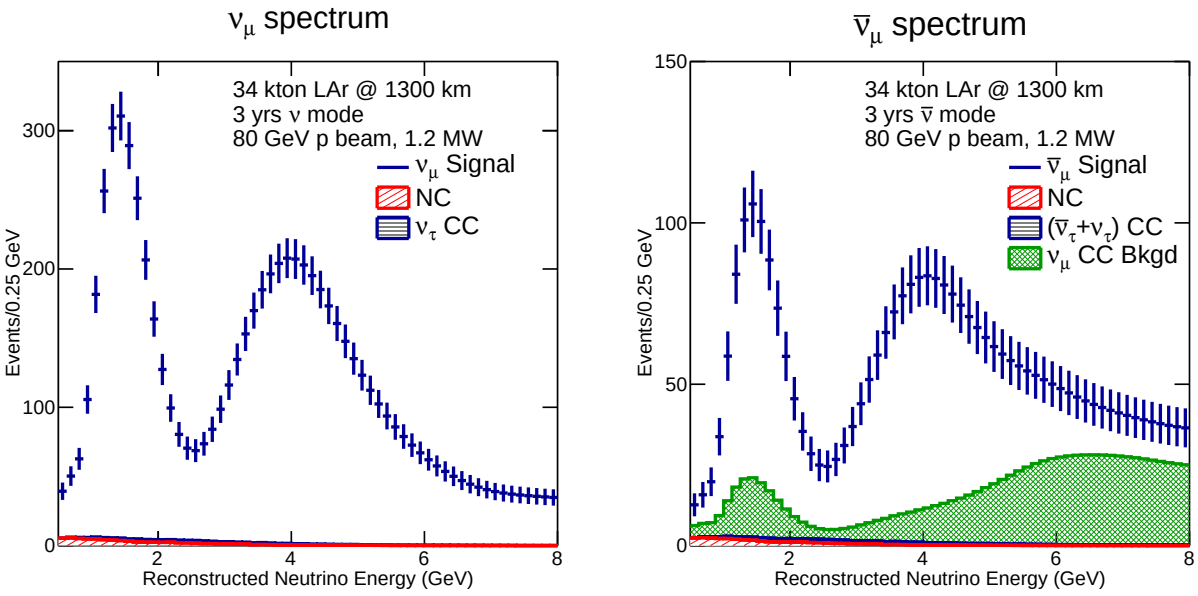

Figure 4.2: The expected reconstructed neutrino energy spectrum of ν_μ or $\overline{\nu}_\mu$ events in a 34-kt LArTPC for three years of neutrino (left) and antineutrino (right) running with a 1.2-MW beam.

Table 4.3: Expected number of neutrino oscillation signal and background events in the energy range 0.5 GeV to 8.0 GeV at the far detector after detector smearing and event selection. The calculation assumes $\sin^2(2\theta_{13}) = 0.09$ and $\delta_{\rm CP} = 0$. The event rates are given per 10-kt LArTPC and three years of running with the improved 80-GeV LBNE beam at 1.2 MW. For signal, the number of ν and $\overline{\nu}$ events are shown separately, while for the background estimates ν and $\overline{\nu}$ events are combined. The MH has negligible impact on ν_μ disappearance signals.

Beam	**Hierarchy**	**Signal Events**	**Background Events**				
		$\nu_x/\overline{\nu}_x$ **CC**	ν_μ **NC**	ν_μ **CC**	ν_e **Beam**	ν_τ **CC**	**Total**
			$\nu_\mu \rightarrow \nu_{x=\mu}$ **(disappearance)**				
Neutrino	-	2056/96	23	N/A	-	18	41
Antineutrino	-	280/655	10	N/A	-	10	20
			$\nu_\mu \rightarrow \nu_{x=e}$ **(appearance)**				
Neutrino	Normal	229/3	21	25	47	14	107
Neutrino	Inverted	101/5	21	25	49	17	112
Antineutrino	Normal	15/41	11	11	24	9	55
Antineutrino	Inverted	7/75	11	11	24	9	55

The rates are given per 10 kt of fiducial LArTPC mass.

The GLoBES implementation used in the sensitivity studies presented here appears to be in good agreement with more recent results from the Fast MC, described in Section A.3. Updated sensitivity and systematics studies are currently underway using the Fast MC for detector simulation, and customized GLoBES-based software for the oscillation fits and propagation of systematics. A full MC simulation of the far detector and automated event reconstruction is being developed; this is

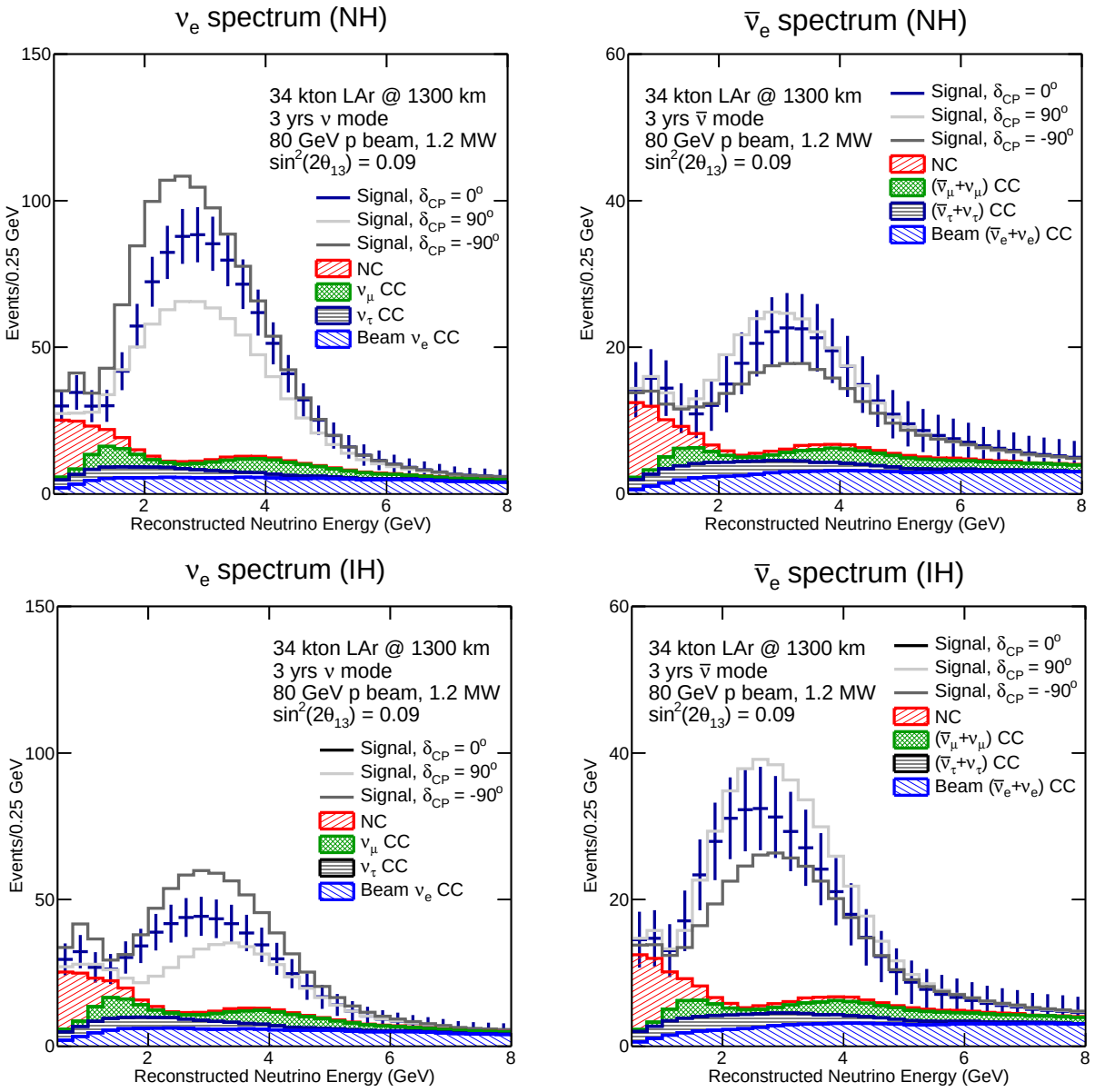

Figure 4.3: The expected reconstructed neutrino energy spectrum of ν_e or $\overline{\nu}_e$ oscillation events in a 34-kt LArTPC for three years of neutrino (left) and antineutrino (right) running with a 1.2-MW, 80-GeV beam assuming $\sin^2(2\theta_{13}) = 0.09$. The plots on the top are for normal hierarchy and the plots on the bottom are for inverted hierarchy.

also described in Appendix A.

4.3 Measurements of Mass Hierarchy and the CP-Violating Phase

The neutrino mass hierarchy (MH) and the value of the CP-violating phase, $\delta_{\rm CP}$, are currently unknown. Knowledge of the MH has significant theoretical, cosmological and experimental implications. A determination of the $\delta_{\rm CP}$ value to be neither zero (0) nor π would constitute the first observation of CP violation in the lepton sector.

The expected performance of a 10-kt LArTPC far detector 1,300 km downstream from a neutrino source is detailed in the LBNE Conceptual Design Report Volume 1 [13]. Estimated sensitivities to the determination of the MH and discovery of CP violation, presented both here and in the CDR, are calculated using the GLoBES package. The detector response assumed in these calculations is summarized in Table 4.2. The sensitivities are obtained by simultaneously fitting the $\nu_\mu \rightarrow \nu_\mu$, $\overline{\nu}_\mu \rightarrow \overline{\nu}_\mu$, $\nu_\mu \rightarrow \nu_e$, and $\overline{\nu}_\mu \rightarrow \overline{\nu}_e$ oscillated spectra, examples of which are shown in Figures 4.2 and 4.3. The ν_τ background is not used in the sensitivity calculations since it is expected that further analysis will reduce this background to negligible levels.

In these calculations, experimental sensitivity is quantified using $\Delta\chi^2$ parameters, which are determined by comparing the predicted spectra for various scenarios. These quantities are defined, differently for neutrino MH and CP-violation sensitivity, to be:

$$\Delta\chi^2_{MH} = |\chi^2_{MH^{test}=IH} - \chi^2_{MH^{test}=NH}|, \tag{4.1}$$

$$\Delta\chi^2_{CPV} = \min\left(\Delta\chi^2_{CP}(\delta^{test}_{\rm CP}=0), \Delta\chi^2_{CP}(\delta^{test}_{\rm CP}=\pi)\right), \text{ where} \tag{4.2}$$

$$\Delta\chi^2_{CP} = \chi^2_{\delta^{test}_{\rm CP}} - \chi^2_{\delta^{true}_{\rm CP}}. \tag{4.3}$$

These sensitivities are evaluated separately for true NH and IH. Since the true value of $\delta_{\rm CP}$ is unknown, a scan is performed over all possible values of $\delta^{true}_{\rm CP}$. The individual χ^2 values are calculated using

$$\chi^2(\mathbf{n}^{true}, \mathbf{n}^{test}, f) = 2\sum_i^{N_{reco}} (n_i^{true} ln \frac{n_i^{true}}{n_i^{test}(f)} + n_i^{test}(f) - n_i^{true}) + f^2, \tag{4.4}$$

where $\mathbf{n}$ are event rate vectors in N_{reco} bins of reconstructed energy and f represents a nuisance parameter to be profiled. Nuisance parameters include the values of mixing angles, mass splittings, and signal and background normalization. The nuisance parameters are constrained by Gaussian priors; in the case of the oscillation parameters, the Gaussian prior has standard deviation determined by taking 1/6 of the 3σ range allowed by the global fit [17].

With the exception of results reported in Section 4.3.1, where more information on the statistical interpretation of MH sensitivity is provided, the sensitivities presented here are for the *typical experiment* with no statistical fluctuations considered. In the absence of statistical fluctuations, the χ^2 value for the *true* spectra is identically zero. Statistical fluctuations are incorporated by

repeatedly varying the contents of each energy bin in each sample by drawing from a Poisson distribution with the expected number of events in that bin as the mean.

This section presents the sensitivities of various LBNE configurations to determination of the MH and CP violation. In particular, a 10-kt far detector and the full-scope 34-kt far detector are considered. In each case, the performance of LBNE with both the 120-GeV beamline design presented in the CDR [18] as well as the upgraded 80-GeV beam described in Section 3.4 is studied. In addition, the sensitivities at different possible stages of LBNE with increases to far detector mass and Main Injector beam upgrades are estimated.

Figure 4.4 summarizes the sensitivities for determining the MH and CP violation ($\delta_{\rm CP} \neq 0$ or π) as a function of the true value of $\delta_{\rm CP}$ with a 10-kt LArTPC. The red band shows the sensitivity that is achieved with an exposure of six years with equal exposures in ν and $\overline{\nu}$ mode in a 1.2-MW beam. The cyan band shows the sensitivity obtained by combining the 10-kt LBNE with T2K and NOνA, where the T2K exposure is 7.8×10^{21} POT in ν mode only and the NOνA exposure is six years (assuming 6×10^{20} POT per year) with equal exposures in ν and $\overline{\nu}$ mode. The bands indicate the sensitivity range corresponding to different levels of signal and background normalization uncertainties and different possible beam designs. The gray curves are the expected sensitivities for the combination of NOνA and T2K. The known mixing parameters are allowed to float in the fit, but are constrained (using a Gaussian prior) by the uncertainties from the 2012 global best fit [17]. The reactor mixing angle, $\sin^2 2\theta_{13}$, is constrained to be 0.094 ± 0.005. The uncertainty is equal to the size of the current systematic uncertainty from the Daya Bay Experiment [19] and is used as a conservative estimate of the precision that will be achieved by the current generation of reactor experiments. Figure 4.5 shows the sensitivities for determining the MH and CP violation as a function of the true value of $\delta_{\rm CP}$ after six years of running in the LBNE 34-kt configuration under the same assumptions.

The sensitivity bands in Figures 4.4 and 4.5 represent the variation in sensitivity as a function of the beam design and normalization uncertainties on the signal and background. The solid curve at the lower end of the red band represents the beamline design described in the LBNE CDR Volume 2 [18] for which there is no near detector. The dashed line above the solid curve represents the sensitivity with the beam design improvements currently under study as described in Section 3.4, still without a near detector. The dashed line at the upper end of the red band represents the case in which both the beam design improvements and a high-resolution, highly capable near detector are implemented. The key design goal of the LBNE near detector and beamline simulation software is to enable a prediction of the far detector unoscillated flux with a precision of $\leq 2\%$. Therefore, the total signal and background normalization uncertainties on the ν_μ disappearance signal are assumed to be 5% and 10%, respectively. The default ν_e appearance signal *uncorrelated* normalization uncertainties for the full-scope LBNE presented in this chapter are assumed to be 1%. The ν_e appearance background uncertainty is expected to be at least as good as the $\sim 5\%$ [20] achieved by the ν_e appearance search in the MINOS experiment.

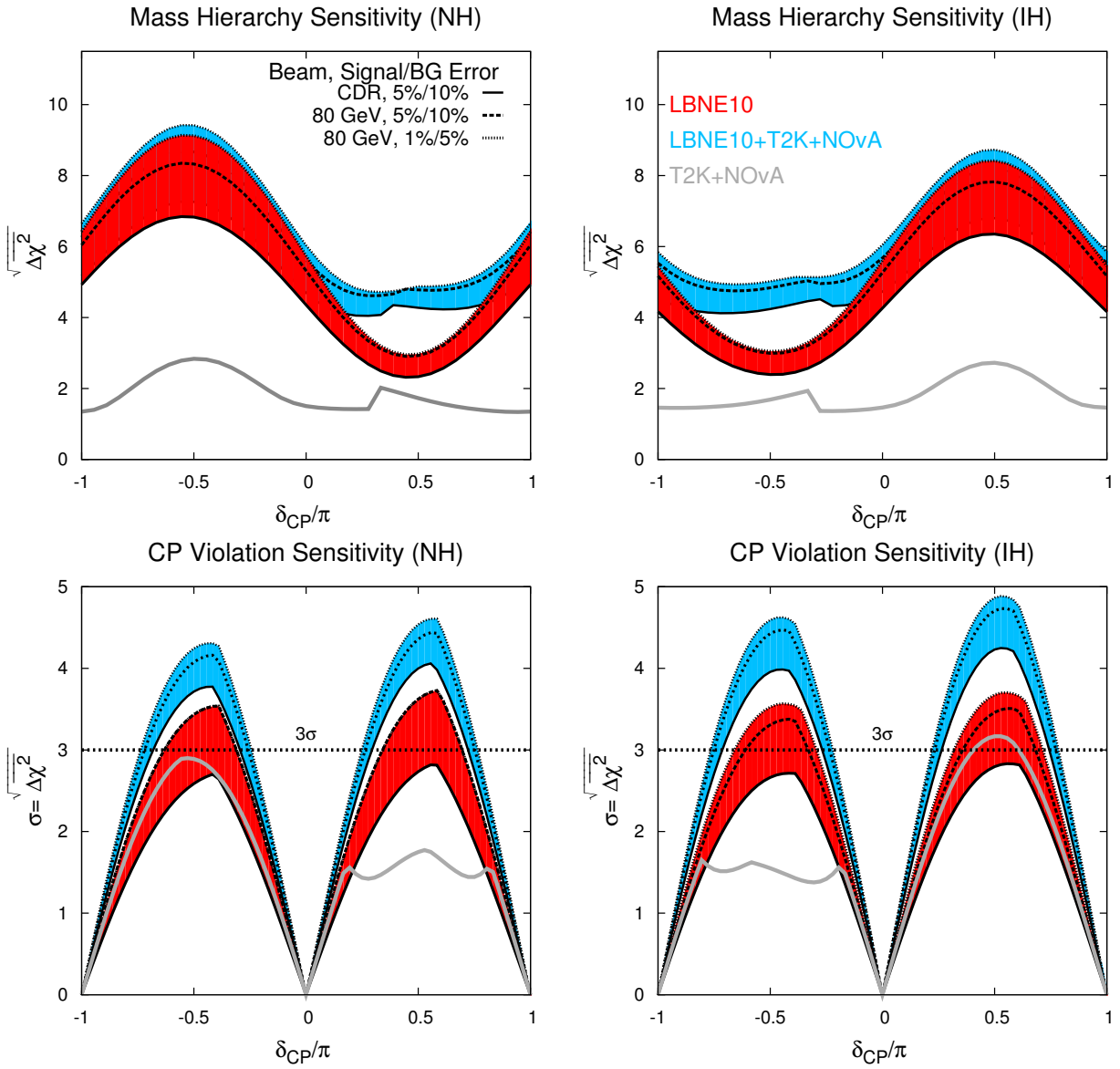

Figure 4.4: The significance with which the mass hierarchy (top) and CP violation ($\delta_{\rm CP} \neq 0$ or π, bottom) can be determined as a function of the value of $\delta_{\rm CP}$. The plots on the left are for normal hierarchy and the plots on the right are for inverted hierarchy. The red band shows the sensitivity that is achieved by a typical experiment with the LBNE 10-kt configuration alone, where the width of the band shows the range of sensitivities obtained by varying the beam design and the signal and background uncertainties as described in the text. The cyan band shows the sensitivity obtained by combining the 10-kt LBNE with T2K and NOνA, and the gray curves are the expected sensitivities for the combination of NOνA and T2K; the assumed exposures for each experiment are described in the text. For the CP-violation sensitivities, the MH is assumed to be unknown.

A detailed discussion of the systematics assumptions for LBNE is presented in Section 4.3.2. In the case that LBNE has no near neutrino detector, the uncertainties on signal and background are expected to be 5% and 10%, respectively, extrapolating from the performance and detailed knowledge of the NuMI beam on which the LBNE beamline is modeled, in situ measurements of

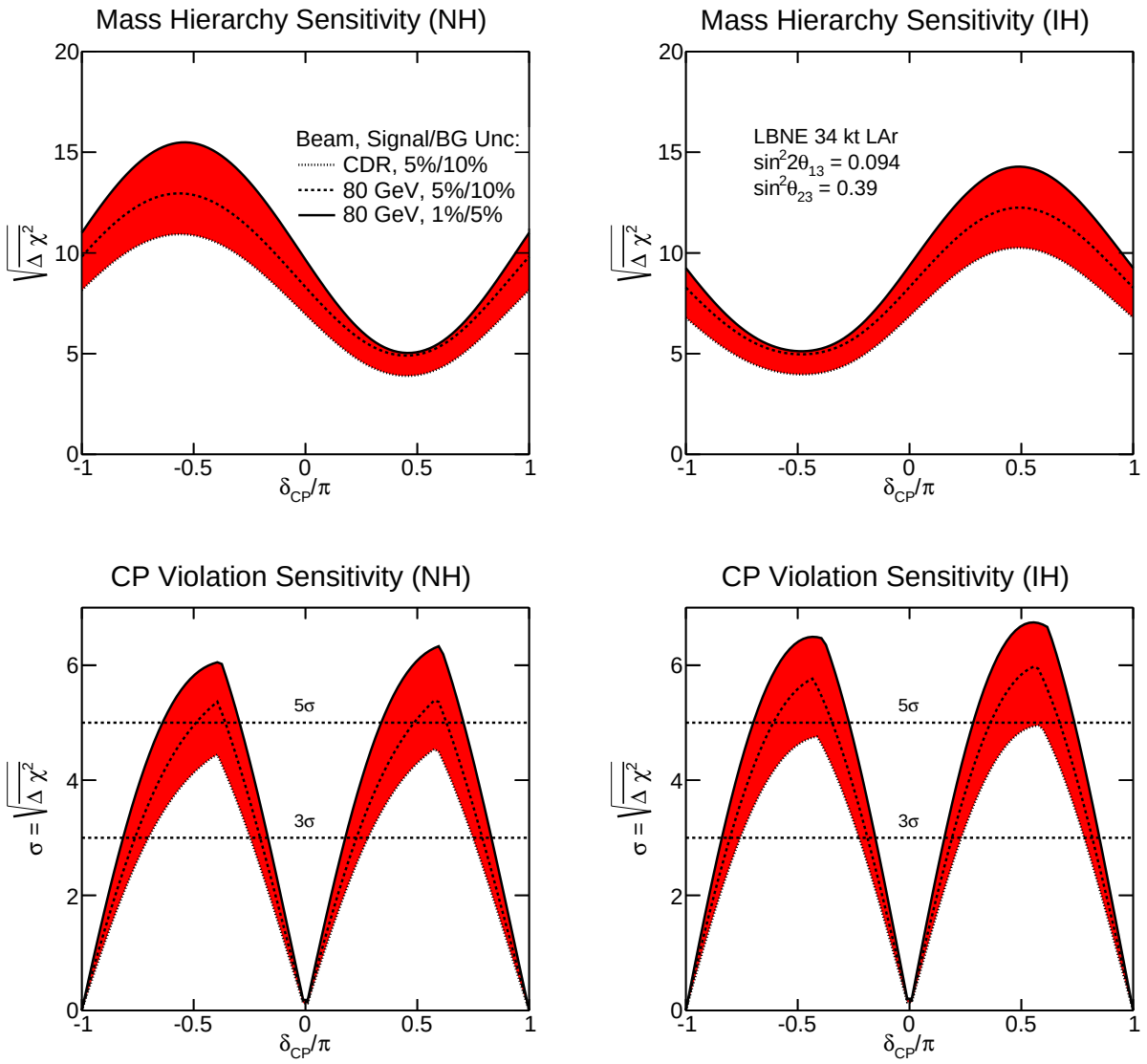

Figure 4.5: The significance with which the mass hierarchy (top) and CP violation ($\delta_{\rm CP} \neq 0$ or π, bottom) can be determined by a typical LBNE experiment with a 34-kt far detector as a function of the value of $\delta_{\rm CP}$. The plots on the left are for normal hierarchy and the plots on the right are for inverted hierarchy. The width of the red band shows the range of sensitivities that can be achieved by LBNE when varying the beam design and the signal and background uncertainties as described in the text.

the muon flux at the near site as described in [13], the expectation of improved hadron production measurements with the NA61 and MIPP experiments, and the experience of previous ν_e appearance experiments as summarized in Table 4.4.

Table 4.4: Summary of achieved systematic error performance in several select prior $\nu_\mu \rightarrow \nu_e$ oscillation experiments. These numbers were extracted from publications and may not correspond exactly to the description in the text. NBB/WBB indicates a narrow/wide band beam. *No ND* indicates there was no near detector, and *ND-FD* indicates a two (near-far) detector experiment with extrapolation of the expected background and signal from the near to the far detector. In the case of T2K, the quoted systematic (*) is actually the total uncertainty on the observed events, which are predominately signal.

Experiment	Year	ν_μ-NC/CC Events	ν_e-CC Events	Background Syst.Error	Comment
BNL E734 [21]	1985	235	418	20%	No ND
BNL E776(NBB) [22]	1989	10	9	20%	No ND
BNL E776 (WBB) [23]	1992	95	40	14%	No ND
NOMAD [24]	2003	$<$300	5500	$< 5\%$	No ND
MiniBooNE [25]	2008	460	380	9%	No ND
MiniBooNE [26]	2013	536	782	5%	SciBooNE
MINOS [20]	2013	111	36	4%	ND–FD
T2K [27]	2013	1.1	26	9%*	ND–FD

4.3.1 Interpretation of Mass Hierarchy Sensitivities

LBNE will be definitive in its ability to discriminate between normal and inverted mass hierarchy for the allowed range of unknown parameters such as $\delta_{\rm CP}$ and $\sin^2\theta_{23}$. To assess the sensitivity of LBNE to this physics, particularly for the case of less favorable parameter values, detailed understanding of statistical significance is essential.

At the true values of $\delta_{\rm CP}$ for which the mass hierarchy asymmetry is maximally offset by the leptonic CP asymmetry, LBNE's sensitivity to the mass hierarchy is at its minimum. Even in this case, with a 34-kt LArTPC operating for six years in a 1.2-MW beam, the $|\Delta\chi^2|$ value obtained in a typical data set will exceed 25, allowing LBNE on its own to rule out the incorrect mass ordering at a confidence level above $1-3.7\times10^{-6}$. Considering fluctuations, LBNE will measure, in $\geq 97.5\%$ of all possible data sets for this least favorable scenario, a value of $|\Delta\chi^2|$ equal to 9 or higher, which corresponds to a $\geq 99\%$ probability of ruling out the incorrect hierarchy hypothesis.

In the mass hierarchy (MH) determination, only two possible results are considered, as the true MH is either normal (NH) or inverted (IH). Reference [28] presents the statistical considerations of determining the sensitivity of an experiment to the MH, framed partly in the context of two separate but related questions:

1. *Given real experimental data, with what significance can the MH be determined?*

2. *When evaluating future experimental sensitivities, what is the probability that a particular experimental design will be able to determine the MH with a given significance?*

Once data are in hand, a number of techniques based either within Bayesian or frequentist statistics make it possible to determine the level of confidence at which one MH hypothesis or the other can be ruled out. In assessing the sensitivity of future experiments, it is common practice to generate a simulated data set (for an assumed true MH) that does not include statistical fluctuations. The expected sensitivity can be reported as $\overline{\Delta\chi^2}$, representative of the mean or the most likely value of $\Delta\chi^2$ that would be obtained in an ensemble of experiments for a particular true MH. With the exception of Figure 4.7, the sensitivity plots in this document have been generated using this method.

However, addressing the expected sensitivity of an experiment per the second question above requires consideration of the effect of statistical fluctuations and variations in systematics. If the experiment is repeated many times, a distribution of $\Delta\chi^2$ values will appear. Studies in [28] and elsewhere (e.g., [29]) show that the $\Delta\chi^2$ metric employed here *does not* follow the commonly expected χ^2 function for one degree of freedom, which has a mean of $\overline{\Delta\chi^2}$ and can be interpreted using a Gaussian distribution with a standard deviation of $\sqrt{|\overline{\Delta\chi^2}|}$. Rather, these studies show that when the observed counts in the experiment are large enough, the distribution of $\Delta\chi^2$ used here approximately follows a Gaussian distribution with a mean and standard deviation of $\overline{\Delta\chi^2}$ and $2\sqrt{|\overline{\Delta\chi^2}|}$, respectively [28].

Figure 4.6 shows the expected distribution of $\Delta\chi^2$ values in LBNE from toy Monte Carlo studies. The interpretation of pairs of distributions, such as those in the various panels of this figure, depends on the information being sought. For example, one is not necessarily interested simply in the fraction of experiments where $\Delta\chi^2$ has the "right" sign. (An experiment that obtains a small value of $\Delta\chi^2$, even with the "right" sign, would not be particularly constraining since there is no way *a priori* to know which is the right sign — this is what the experiment is attempting to measure.) It should also be noted that in general $|\overline{\Delta\chi^2_{\mathrm{MH=NH}}}|$, i.e., true NH, is not necessarily equal to $|\overline{\Delta\chi^2_{\mathrm{MH=IH}}}|$, i.e., true IH, nor do the corresponding distributions necessarily have the same shape. For some ranges in δ_{CP}, for example, the event rate in LBNE is sufficiently different for the two MH hypotheses that the corresponding distributions in $\Delta\chi^2$ are quite distinct.

The plots shown on the left in Figure 4.6 illustrate the case for a true value of $\delta_{\mathrm{CP}} = 0°$, where the $\Delta\chi^2$ distributions for NH and IH scenarios are similar. Shown on the right are the corresponding distributions for the case of $\delta_{\mathrm{CP}} = 90°$, where for NH the matter asymmetry is maximally offset by the CP asymmetry, leading to poorer MH discrimination. For the IH case, these effects go in the same direction, leading to better MH discrimination. The converse is the case for $\delta_{\mathrm{CP}} = -90°$. Since the true value of δ_{CP} is unknown (although a best-fit value and confidence interval

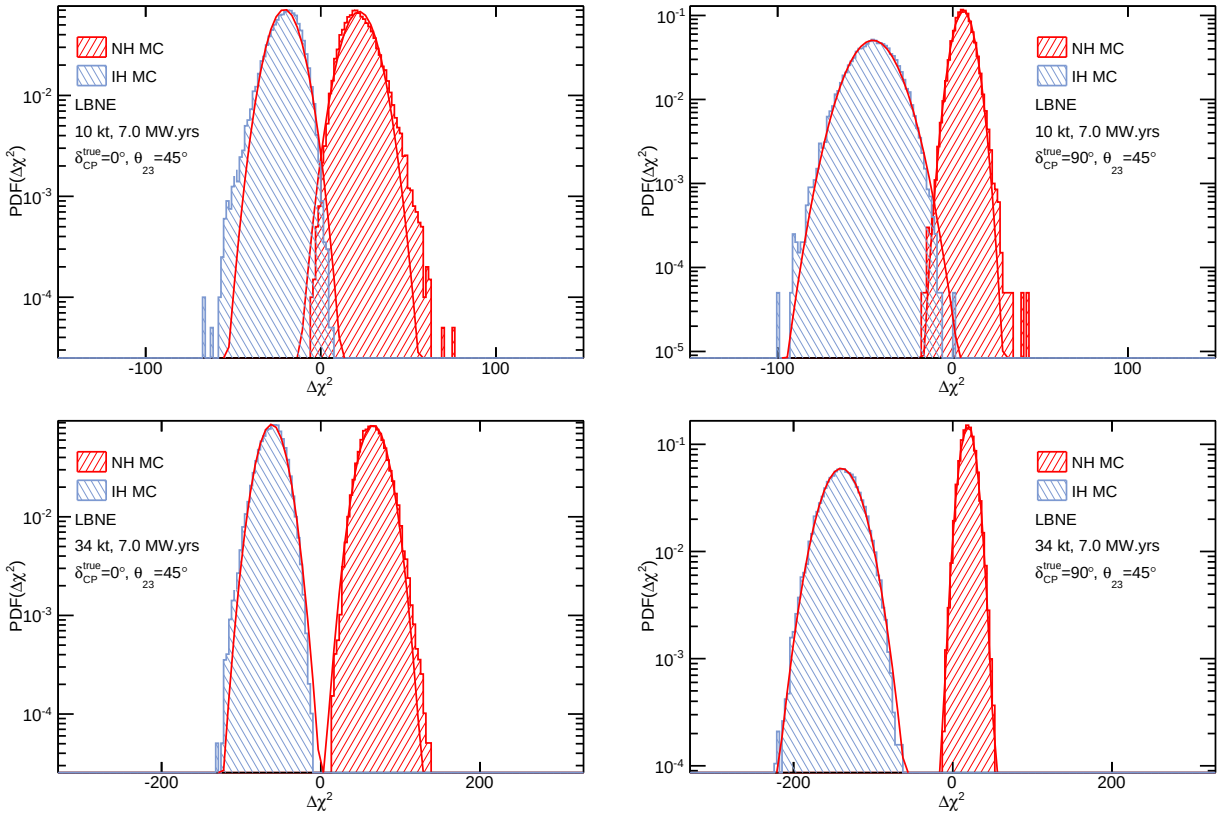

Figure 4.6: $\Delta\chi^2_{\mathrm{MH=NH}}$ (red) and $\Delta\chi^2_{\mathrm{MH=IH}}$ (blue) distributions for LBNE from Toy MC studies. The top set of figures are for a 10-kt detector operating six years in a 1.2-MW beam. The bottom set is for a 34-kt detector operating six years in a 1.2-MW beam. The figures on the left are for $\delta_{cp}^{true} = 0$ and the figures on the right are for $\delta_{cp}^{true} = 90°$. The value of δ_{CP} is unconstrained in the fit.

will emerge from the analysis of the data collected), comparison of a given value of $\Delta\chi^2$ with expected distributions for NH and IH cases for the *same* value of δ_{CP} does not in general provide the appropriate test. For simplicity, following [29], the discussion below focuses on the respective values of δ_{CP} for which the experiment will have poorest sensitivity for NH ($+90°$) and IH ($-90°$) scenarios.

Given the above introduction to the statistical fluctuation issues, it is natural to employ the statistical language of hypothesis testing in projecting LBNE's MH sensitivity. Specifically, α is defined as the desired Type-I error rate — that is, the probability of rejecting a particular hypothesis, e.g., NH, in the case where this is the true hypothesis. One can then ask what the corresponding Type-II error rate β would be, defined as the probability of accepting the hypothesis being tested (NH in this example), when in fact the alternate hypothesis (IH) is true. The pair of α and β would correspond to a particular value of $\overline{\Delta\chi^2}$ chosen (in advance of the experiment) as a criterion for deciding whether to rule out the NH (or IH). Historically, many experiments have characterized their anticipated sensitivity by reporting α for the case of $\beta = 0.5$, which is nothing more than that given by the median value of the test statistic (in this case, $\Delta\chi^2 = \overline{\Delta\chi^2}$) as described above.

Sometimes, the sensitivity is also reported as the square root of $\overline{\Delta\chi^2}$.

Due to the approximate symmetry of the MH ambiguity as a function of $\delta_{\rm CP}$ for the two MH scenarios and the desire to be able to reject exactly one of the two possible mass orderings [29], it is also natural to report a value of α for an experiment such that $\alpha = \beta$ [30,31,29]. In this way, it is possible to express just how *unlucky* an experiment can be while maintaining a corresponding sensitivity α. In the case of LBNE, a reasonable benchmark for comparison corresponds to $\overline{\Delta\chi^2} = 36$. For this case, specifying $\alpha = \beta$ yields $\alpha = 0.0013$, which means that the experiment will have a 0.13% probability of ruling out the true MH hypothesis and of accepting the wrong MH hypothesis.

As described above, and as is evident in the plots presented, such as those in Figures 4.4 and 4.5, the sensitivity of LBNE is strongly dependent on the true value of $\delta_{\rm CP}$; Figure 4.7 shows that it also depends on the true value of $\sin^2\theta_{23}$. While plotting the value of α (for some choice of β, such as $\beta = 0.5$ or $\beta = \alpha$) as a function of these parameters encapsulates the sensitivity, a visually helpful presentation is obtained by plotting the expected mean value, $\overline{\Delta\chi^2}$, as well as ranges of possible values corresponding to the expected distribution in $\Delta\chi^2$. Thus, Figure 4.7 shows the dependence of $\sqrt{|\overline{\Delta\chi^2}|}$ on the true value of $\delta_{\rm CP}$ for the typical LBNE data set, for two possible values of $\sin^2\theta_{23}$, as well as the corresponding expectation bands within which 68% (green) and 95% (yellow) of LBNE sensitivities will fall. These expectation bands give a semi-quantitative picture of the likely range of outcomes for the experiment.

The horizontal dashed lines on Figure 4.7 specify the confidence level of an experiment with a particular value of $\Delta\chi^2$ such that:

$$\mathrm{CL} = P(\text{favored MH}|\text{data}\,x)/(P(\text{favored MH}|\text{data}\,x) + P(\text{unfavored MH}|\text{data}\,x)), \quad (4.5)$$

following the convention in [28], where the notation $P(\mathrm{A}|\mathrm{B})$ represents the probability of A given condition B, and these probabilities are inferred from the corresponding likelihoods via Bayes' Theorem. Alternatively, the $\Delta\chi^2$ values shown in these plots can be approximately translated to sensitivities in terms of α, for whatever choice of β is desired, following, for example, the prescription described in [29].

As seen in Figure 4.7, a typical LBNE data set with a 34-kt detector can determine the MH with $|\overline{\Delta\chi^2}| \geq 25$ for all values of $\delta_{\rm CP}$ (for the left plot, where $\sin^2\theta_{23} = 0.39$). From a Bayesian analysis, the probability that an experiment measuring $|\Delta\chi^2| = 25$ has ruled out the true MH hypothesis is 3.7×10^{-6}, as indicated for the corresponding horizontal dashed line in the plots in this figure. When considering the effect of statistical fluctuations, for the same value of θ_{23}, about 97.5% of experiments will determine the MH with $|\Delta\chi^2| > 9$ for the least favorable value of $\delta_{\rm CP}$, where $|\Delta\chi^2| = 9$ corresponds to a CL of 98.9%.

For the bulk of the range of $\delta_{\rm CP}$, the sensitivity of LBNE is vastly better than for the least favorable value described above. Furthermore, newer data prefer values of θ_{23} closer to maximal [32], which

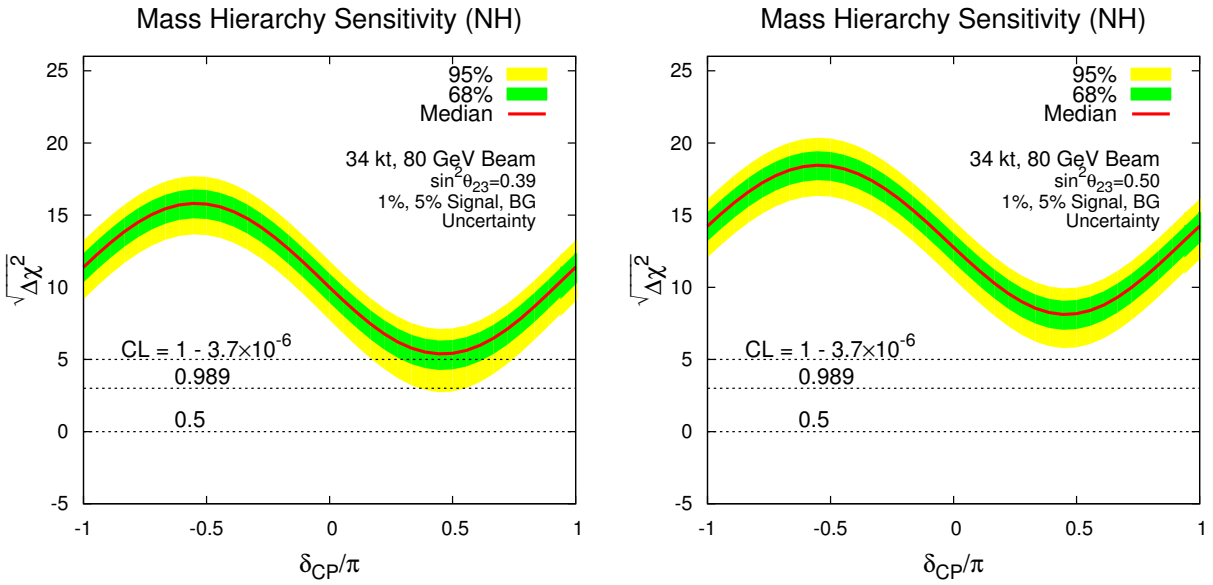

Figure 4.7: The square root of the mass hierarchy discrimination metric $\Delta\chi^2$ is plotted as a function of the unknown value of $\delta_{\rm CP}$ for the full-scope LBNE with 34 kt, 3+3 ($\nu + \overline{\nu}$) years of running in a 1.2-MW beam, for true NH. The red curve represents the most likely experimental value obtained, estimated using a data set absent statistical fluctuations, while the green and yellow bands represent the range of $\Delta\chi^2$ values expected in 68% and 95% of all possible experimental cases, respectively. The horizontal lines indicate the probability that an experiment with that value of $\Delta\chi^2$ correctly determines the MH, computed according to a Bayesian statistical formulation. The plot on the left assumes a value of $\sin^2\theta_{23} = 0.39$ [17], while that on the right assumes $\sin^2\theta_{23} = 0.5$ (maximal ν_μ-ν_τ mixing).

results in significantly enhanced LBNE MH sensitivity. As shown in the right-hand plot of Figure 4.7, if $\sin^2\theta_{23} = 0.5$, the expected MH sensitivity for the typical LBNE experiment at the least favorable $\delta_{\rm CP}$ point is $|\overline{\Delta\chi^2}| \approx 64$, which is significantly larger than the sensitivity of $|\overline{\Delta\chi^2}| \approx 25$ expected for the same value of $\delta_{\rm CP}$ if $\sin^2\theta_{23} = 0.39$. This suggests that a typical LBNE data set will determine the MH with $|\Delta\chi^2|$ well above the benchmark value of 36 mentioned above for even the least favorable values of $\delta_{\rm CP}$.

In addition to detailed LBNE-specific frequentist studies reported in [29], an LBNE-specific update (using both Bayesian and frequentist approaches) to the general statistical studies reported in [28] is in preparation.

4.3.2 Sensitivities and Systematics

The main systematic uncertainties in any experiment are determined by the analysis strategy employed and the performance of the detector. Figure 4.8 outlines the analysis strategy commonly employed to extract oscillation parameters in two-detector long-baseline neutrino oscillation experiments. The measured spectrum of ν_μ events in the near detector, $N_{\rm ND}^{data}(\nu_\mu)$ is extrapolated to the far detector and is used to predict both the ν_μ and ν_e appearance signals in the far detector, $N_{\rm FD}^{expected}(\nu_\mu)$ and $N_{\rm FD}^{expected}(\nu_e)$ respectively. The measured spectrum of ν_e candidates in the near

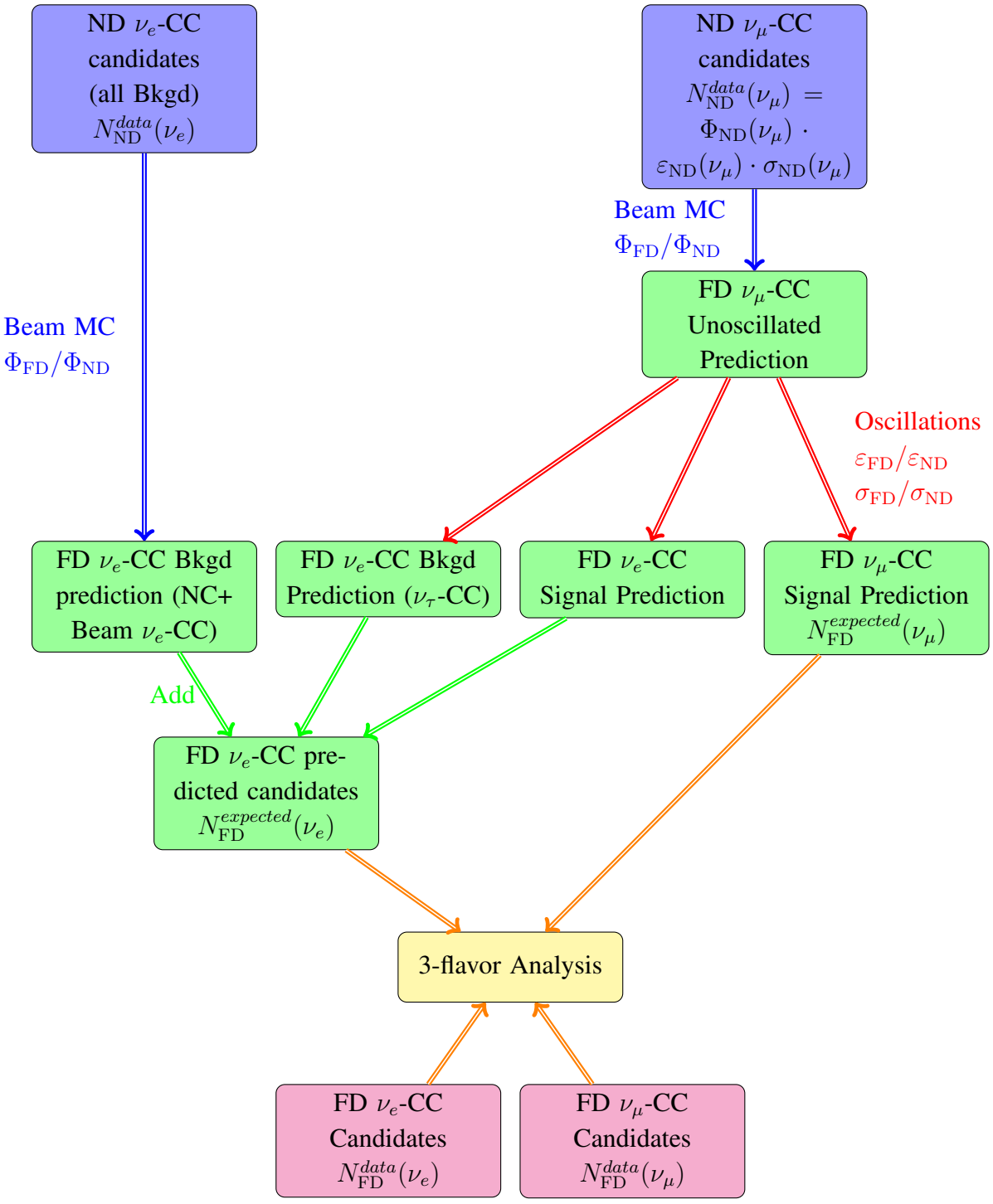

Figure 4.8: Flow chart of the ν_e appearance analysis method in a two-detector long-baseline experiment. Φ refers to the beam flux, ε refers to detector efficiencies and smearing, and σ refers to neutrino interaction modeling. The terms ND and FD refer to the near and far detector, respectively.

detector, $N_{\rm ND}^{data}(\nu_e)$, which comprises mostly the beam ν_e events and NC π^0 misidentified events, is used to predict the background to the ν_e appearance signal in the far detector. In LBNE, neutrino oscillation parameters will be extracted using a fit to four far detector data samples: ν_e, $\overline{\nu}_e$, ν_μ, and $\overline{\nu}_\mu$, which will allow for partial cancellation of uncertainties.

In the current generation of experiments, the measured spectrum of neutrino events in the near detector is a product of beam flux (Φ), detector efficiency and smearing (ε), and neutrino interaction dynamics (σ). To extrapolate the observed spectra in the near detector to the far detector, corrections have to be made for:

1. Differences in the beam flux in the near and far detectors, $\Phi_{\rm FD}/\Phi_{\rm ND}$: The near detector is much closer to the neutrino beamline and sees an extended source of neutrinos from the decay pipe as compared to the far detector, which observes a point source. A beam MC is used to correct for these differences. Uncertainties arise from inaccuracies in the simulation of the hadron production from the target, the focusing of the horns, the material in the beamline (which absorbs hadrons before they can decay), and the decay channel geometry.

2. Differences in near and far detector smearing and efficiencies, $\varepsilon_{\rm FD}/\varepsilon_{\rm ND}$: The largest uncertainties arise from the different event selection efficiencies in the near and far detectors and, in particular, the imperfect modeling of the energy scales of the near and far detectors. Identical near and far detectors allow most of these uncertainties to cancel in the extrapolation in the case of the ν_μ signal prediction. The ν_e signal prediction is extrapolated from $N_{\rm ND}^{data}(\nu_\mu)$; thus there are irreducible residual uncertainties arising from different criteria used to select ν_e and ν_μ candidate events and different detector response functions.

3. Differences in the interactions of neutrinos in the near and far detector, $\sigma_{\rm FD}/\sigma_{\rm ND}$: In the case in which both near and far detectors use the same target nucleus, the differences cancel for extrapolation of the ν_μ signal from the near to the far detector. When using the ν_μ signal in the near detector to predict the ν_e (and ν_τ) signals in the far detector, uncertainties arising from differences in ν_e (ν_τ) and ν_μ interactions, $\sigma_{\rm FD}(\nu_e)/\sigma_{\rm ND}(\nu_\mu)$, dominate. These uncertainties are limited by theoretical uncertainties and are typically smaller at higher energies.

The estimation of the expected signals at the far detector can be summarized thus:

$$N_{\rm ND}^{data}(\nu_\mu) = \Phi_{\rm ND}(\nu_\mu) \otimes \varepsilon_{\rm ND}(\nu_\mu) \otimes \sigma_{\rm ND}(\nu_\mu) \tag{4.6}$$

$$N_{\rm FD}^{expected}(\nu_\mu) = N_{\rm ND}^{data}(\nu_\mu) \otimes \frac{\Phi_{\rm FD}(\nu_\mu)}{\Phi_{\rm ND}(\nu_\mu)} \otimes P(\nu_\mu \to \nu_\mu) \otimes \frac{\varepsilon_{\rm FD}(\nu_\mu)}{\varepsilon_{\rm ND}(\nu_\mu)} \otimes \frac{\sigma_{\rm FD}(\nu_\mu)}{\sigma_{\rm ND}(\nu_\mu)} \tag{4.7}$$

$$
\begin{aligned}
N_{\mathrm{FD}}^{expected}(\nu_e) \;=\; & \underbrace{N_{\mathrm{ND}}^{data}(\nu_\mu) \otimes \frac{\Phi_{\mathrm{FD}}(\nu_\mu)}{\Phi_{\mathrm{ND}}(\nu_\mu)} \otimes P(\nu_\mu \to \nu_e) \otimes \frac{\varepsilon_{\mathrm{FD}}(\nu_e)}{\varepsilon_{\mathrm{ND}}(\nu_\mu)} \otimes \frac{\sigma_{\mathrm{FD}}(\nu_e)}{\sigma_{\mathrm{ND}}(\nu_\mu)}}_{\text{Expected signal events}} \\
& + \underbrace{N_{\mathrm{ND}}^{data}(\nu_e) \otimes \frac{\Phi_{\mathrm{FD}}(\nu_e)}{\Phi_{\mathrm{ND}}(\nu_e)} \otimes P(\nu_e \to \nu_e) \otimes \frac{\varepsilon_{\mathrm{FD}}(\nu_e)}{\varepsilon_{\mathrm{ND}}(\nu_e)} \otimes \frac{\sigma_{\mathrm{FD}}(\nu_e)}{\sigma_{\mathrm{ND}}(\nu_e)}}_{\text{Beam } \nu_{\mathrm{e}} \text{ events}} \\
& + \text{NC background extrapolated from } N_{\mathrm{ND}}^{data}(\nu_e) \\
& + \nu_\tau \text{ background extrapolated from } N_{\mathrm{ND}}^{data}(\nu_\mu)
\end{aligned}
\tag{4.8}
$$

Expected systematic uncertainties on the LBNE ν_e appearance and ν_μ signal samples in the three-flavor fit for LBNE (Table 4.2) are extrapolated from the current performance of the MINOS [20,33] and T2K [27] experiments. The dominant uncertainties on the current ν_e appearance analysis from MINOS and T2K and the expected corresponding uncertainties in LBNE are shown in Table 4.5. The categorization of the dominant experimental uncertainties in Table 4.5 are not always in exact correspondence since T2K and MINOS are very different experiments and deploy different analysis techniques. A detailed description of the expected LBNE performance on each of the dominant uncertainties follows.

Beam flux uncertainties: The LBNE high-resolution near detector is being designed with the goal of accurately measuring the unoscillated beam flux at the near site with a precision $\leq 2\%$ for both shape and absolute normalization. Table 4.6 summarizes the precision that can be achieved using different near detector analysis techniques, described in detail in Section 7.1, to measure the absolute normalization and shape of the different components of this flux. It is important to note that several of these techniques have already been used and *proven to work* in neutrino experiments such as MINOS [34] and NOMAD [35,36]. In particular, the inclusive neutrino charged current (CC) cross-section measurement in the MINOS near detector reported in [34] has already achieved a normalization uncertainty of $\sim 2\%$ in the range of $3 < E_\nu < 9$ GeV using the low-ν_0 method described in Section 7.1. The total systematic uncertainty on the NuMI neutrino flux determination by the MINOS near detector reported in [34] was $\sim 6\%$ and was limited by the detector performance. Recent independent studies on extraction of the neutrino flux using the low-ν_0 method [37] indicate that the technique can be reliably extended down to 1 GeV.

The LBNE near detector is being designed to significantly improve performance relative to the current generation of high-intensity neutrino detectors. A detailed beamline simulation will enable the extrapolation of the LBNE near detector flux measurements to the unoscillated far detector spectrum with high precision using techniques similar to those used by MINOS [38]. The near-to-far ν_μ unoscillated-spectrum extrapolation uncertainties already achieved by MINOS are $< 3\%$ in the MINOS (and also in the LBNE) appearance signal range of $1 < E_\nu < 8$GeV [39,38]. The MINOS extrapolation does not include any independent constraints on the hadron production spectrum from the proton target or information on the horn focusing performance from the muon flux measurements at the near site. The NuMI beamline — the design of which is very similar to

Table 4.5: The dominant systematic uncertainties on the ν_e appearance signal prediction in MINOS and T2K and a projection of the expected uncertainties in LBNE. For the MINOS uncertainties *absolute* refers to the total uncertainty and ν_e is the effect on the ν_e appearance signal only. The LBNE uncertainties are the total *expected* uncertainties on the ν_e appearance signal which include both correlated and uncorrelated uncertainties in the three-flavor fit.

Source of Uncertainty	**MINOS Absolute/ν_e**	**T2K ν_e**	**LBNE ν_e**	**Comments**
Beam Flux after N/F extrapolation	3%/0.3%	2.9%	2%	MINOS is normalization only. LBNE normalization and shape highly correlated between ν_μ/ν_e.
Detector effects				
Energy scale (ν_μ)	7%/3.5%	included above	(2%)	Included in LBNE ν_μ sample uncertainty only in three-flavor fit. MINOS dominated by hadronic scale.
Absolute energy scale (ν_e)	5.7%/2.7%	3.4% includes all FD effects	2%	Totally active LArTPC with calibration and test beam data lowers uncertainty.
Fiducial volume	2.4%/2.4%	1%	1%	Larger detectors = smaller uncertainty.
Neutrino interaction modeling				
Simulation includes: hadronization cross sections nuclear models	2.7%/2.7%	7.5%	$\sim 2\%$	Hadronization models are better constrained in the LBNE LArTPC. N/F cancellation larger in MINOS/LBNE. X-section uncertainties larger at T2K energies. Spectral analysis in LBNE provides extra constraint.
Total	**5.7%**	**8.8%**	**3.6 %**	**Uncorrelated ν_e uncertainty in full LBNE three-flavor fit = 1-2%.**

LBNE's — is expected to operate for more than a decade with improved flux measurements using the much more capable MINERνA detector [40] in both the low-energy and high-energy tunes. MINERνA is designed to measure the absolute NuMI flux with a precision of $\sim 5\%$ or better; data from MINERνA will be used to further improve the accuracy of the LBNE beamline simulation, reducing the uncertainties on the extrapolation of the flux. A new program of hadron production measurements at the NA61/SHINE [41] experiment will also reduce the near-to-far extrapolation uncertainties from the LBNE beamline simulation. The combination of LBNE near detector flux measurements and improved beamline simulation is expected to enable a prediction of the far detector ν_e appearance signal with a precision of $< 2\%$ total normalization and shape uncertainty. Since this uncertainty is highly correlated among the four data samples in the three-flavor fit, the final uncorrelated uncertainty on the ν_e signal sample will be significantly smaller.

Table 4.6: Precisions achievable from in situ ν_μ and ν_e flux measurements in the fine-grained, high-resolution ND with different techniques.

Technique	Flavor	Absolute normalization	Relative flux $\Phi(E_\nu)$	Near Detector requirements
NC Scattering $\boldsymbol{\nu_\mu e^- \to \nu_\mu e^-}$	ν_μ	2.5%	$\sim 5\%$	e ID θ_e Resolution e^-/e^+ Separation
Inverse muon decay $\boldsymbol{\nu_\mu e^- \to \mu^- \nu_e}$	ν_μ	3%		μ ID θ_μ Resolution 2-Track (μ+X) Resolution μ energy scale
CC QE $\boldsymbol{\nu_\mu n \to \mu^- p}$ $\boldsymbol{Q^2 \to 0}$	ν_μ	$3-5\%$	$5-10\%$	D target p Angular resolution p energy resolution Back-Subtraction
CC QE $\boldsymbol{\overline{\nu}_\mu p \to \mu^+ n}$ $\boldsymbol{Q^2 \to 0}$	$\overline{\nu}_\mu$	5%	10%	H target Back-Subtraction
Low-ν_0	ν_μ		2.0%	μ^- vs μ^+ E_μ-Scale Low-E_{Had} Resolution
Low-ν_0	$\overline{\nu}_\mu$		2.0%	μ^- vs μ^+ E_μ-Scale Low-E_{Had} Resolution
Low-ν_0	$\nu_e/\overline{\nu}_e$	1-3%	2.0%	e^-/e^+ Separation (K^0_L)
CC	ν_e/ν_μ	<1%	~2%	e^- ID & μ^- ID p_e/p_μ Resolution
CC	$\overline{\nu}_e/\overline{\nu}_\mu$	<1%	~2%	e^+ ID & μ^+ ID p_e/p_μ Resolution
Low-ν_0/CohPi	$\overline{\nu}_\mu/\nu_\mu$	~2%	~2%	μ^+ ID & μ^- ID p_μ Resolution E_{Had} Resolution

ν_μ energy-scale uncertainty: Both T2K and MINOS use the reconstructed ν_μ event spectrum in the near detector to predict the ν_e appearance signal at the far detector. Therefore the ν_μ energy-scale uncertainty in the near detector is propagated as an uncertainty on the ν_e appearance signal at the far detector. In MINOS — which has a high proportion of non-QE events — the ν_μ energy-scale uncertainty is dominated by uncertainty in the hadronic energy scale (7% for $E_\nu < 3$ GeV) [42] and the muon energy scale (2.5%). Utilization of the low-ν_0 method for energies less than 3 GeV in LBNE reduces the hadronic energy-scale contribution to the uncertainty in the ν_μ energy scale in the near detector. As discussed in Chapter 7, it is expected that both the muon and hadronic energy-scale uncertainties in the near detector will be $<1\%$, so far detector energy-scale uncertainties will

dominate the uncertainty in the ν_μ signal prediction. The high-resolution LArTPC far detector and an active program of hadron test-beam experiments planned for LBNE will reduce far detector hadronic energy-scale uncertainties, which also contribute to uncertainty in the energy scale of the far detector ν_μ signal used in the three-flavor analysis. Extrapolating from MINOS, the LBNE ν_μ energy-scale uncertainty is thus estimated to be $\sim 2\%$.

In MINOS, the 7% ν_μ energy-scale uncertainty resulted in a residual uncertainty of 3.5% on the ν_e signal prediction. In the LBNE full three-flavor analysis, this uncertainty is 100% correlated between the predicted ν_μ and ν_e signal samples; therefore a E_{ν_μ} energy-scale uncertainty of 2% is assigned to the ν_μ signal prediction in LBNE. The residual uncorrelated uncertainty on the ν_e signal prediction is considered to be negligible.

Absolute ν_e energy-scale uncertainties: In Figure 4.9, the MH and CP-violation sensitivity obtained using a rate-only, a shape-only and a rate+shape analysis of ν_e appearance is shown. This study demonstrates that a critical component of LBNE's oscillation sensitivity is an accurate measurement of the shape of the ν_e appearance signal. This measurement depends on the precision

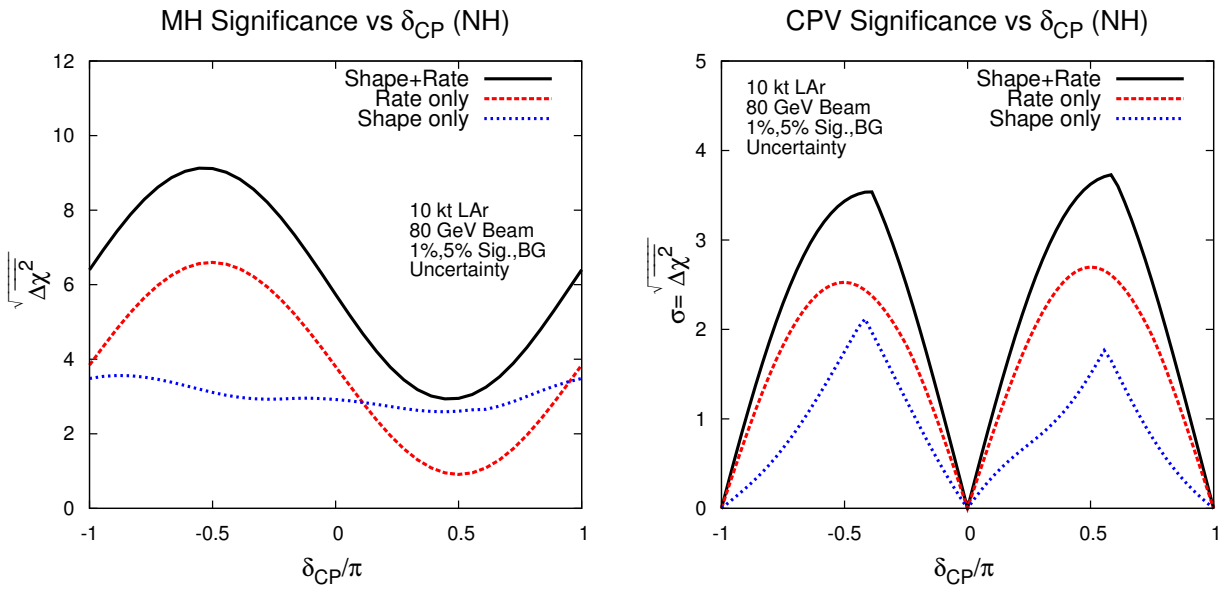

Figure 4.9: The mass hierarchy (left) and CP violation (right) sensitivities from shape, rate, and shape+rate. The sensitivity is for a 10-kt detector, 1.2-MW beam, 3+3 ($\nu + \overline{\nu}$) years, for true normal hierarchy.

with which the detector response to ν_e interactions is understood. The ν_e energy-scale uncertainty, which is not yet included in the current sensitivity calculation with the GLoBES framework, is therefore expected to be an important systematic uncertainty in the LBNE oscillation analysis.

The effect of ν_e energy-scale uncertainty on the ν_e signal normalization, determined by the precision of detector calibration, was 2.7% in MINOS and 3.4% in T2K, where the T2K uncertainty actually includes most far detector effects. LBNE's LArTPC detector technology is expected to

outperform both the MINOS sampling calorimeter and the T2K water Cherenkov detector in reconstruction of the ν_e interaction. For example, the proton produced from the ν_e-QE interaction — the interaction with potentially the best ν_e energy resolution — is clearly visible in a LArTPC [43], whereas it is often below Cherenkov threshold in T2K. An active program of test beam experiments with LArTPCs is currently being planned to address the detector response to electrons and hadrons. Results from the test beam experiments and the projected performance of the in situ calibration will enable LBNE to limit the detector energy-scale uncertainties below the level achieved by the current generation of experiments.

Hadronic energy is expected to contribute more than half of the total energy deposit for many ν_e and ν_μ interactions in LBNE. The hadronic energy scale does not depend on neutrino flavor; since it should be identical for ν_e and ν_μ interactions, this portion of the absolute energy-scale uncertainty is expected to largely cancel in the LBNE three-flavor analysis. This cancellation may be reduced to the extent that event-selection criteria vary the hadronic energy fraction among the samples.

Simulation uncertainties: The simulation uncertainties listed in Table 4.5 refer primarily to uncertainties in modeling neutrino interactions with the target nucleus in the near and far detectors. These uncertainties include ν_e and ν_μ cross-section uncertainties, uncertainties arising from the modeling of the structure of the target nucleus, modeling of final-state interactions within the nucleus, and hadronization model uncertainties arising from the break up of the target nucleus in higher-energy inelastic interactions. The deployment of identical nuclear targets in the MINOS (iron) and LBNE (argon) near and far detectors allows for a larger cancellation of the simulation uncertainties as compared to T2K, which used dissimilar target nuclei in its near detector (carbon) and far detector (oxygen). A high-resolution near detector such as that being designed for LBNE will enable further constraints on the hadronization models by resolving many of the individual particles produced in resonance and deep inelastic interactions, which represent $\sim$75% of LBNE neutrino interactions.

The MINOS ν_e appearance analysis achieved a 2.7% residual uncertainty from simulation after the near-to-far extrapolation. The MINOS simulation uncertainty is dominated by hadronization uncertainties, because cross-section uncertainties largely cancel between the identical nuclei in the near and far detectors. The T2K residual uncertainty after near-to-far extrapolation is 7%. Additionally, the T2K analysis includes more sources of cross-section uncertainties than MINOS and, at the lower T2K energies, larger differences in ν_μ/ν_e cross sections (2.9 %) persist after extrapolating the ν_μ spectrum in the near detector to the ν_e signal prediction in the far.

The LBNE near detector design is required to achieve a cancellation of near-to-far cross-section and hadronization-model uncertainties at the same level as MINOS or better. The ν_e appearance signal in LBNE peaks at 2.5 GeV; these higher energies will result in lower uncertainties from the cross-section effects considered by T2K. In addition, since cross-section variations impact the observed ν_e and ν_μ spectra differently when compared to oscillation effects, the fit to the wide-band spectrum in LBNE could constrain some of these uncertainties further. Therefore, it is expected that

LBNE could reduce the total ν_e appearance simulation uncertainties to a level of 2%. Preliminary results from the LBNE Fast MC simulation (described in Section A.3) indicate that many cross-section uncertainties cancel out when combining the ν_μ disappearance and ν_e appearance signal samples in a three-flavor fit, resulting in a much smaller uncorrelated uncertainty on the ν_e signal sample.

It is important to note that some $\nu/\overline{\nu}$ simulation uncertainties may not cancel out in the near-to-far extrapolation or in the combined fit; in particular, uncertainties due to nuclear models and intra-nuclear effects are different for $\nu/\overline{\nu}$ interactions. New models of intra-nuclear effects are being evaluated to determine the size of these irreducible residual uncertainties. Additionally, there are uncertainties at the level of 1-2% in the cross sections that will not cancel between ν_e and ν_μ [44]. In the absence of theoretical progress, these should also be considered irreducible.

Fiducial volume uncertainties: One of the dominant uncertainties in the MINOS ν_μ disappearance analysis — a high-precision oscillation analysis based on a detailed spectral shape — was the fiducial-volume uncertainty, which included near and far detector reconstruction uncertainties. The uncertainty on the fiducial volume of the MINOS far detector alone was 2.4%. T2K, with a much larger far detector (22.5 kt fiducial), was able to reduce this uncertainty to the 1% level. It is expected that LBNE will be able to achieve this level of uncertainty on the ν_e appearance signal. With the combination of all four signal samples ($\nu_\mu, \overline{\nu}_\mu, \nu_e, \overline{\nu}_e$) in a three-flavor fit, the ν_e uncorrelated portion of this uncertainty is expected to be smaller than 1%.

ν_e appearance background systematic uncertainties: The ν_e appearance normalization uncertainty is expected to be at least as good as the $\sim 5\%$ [20] achieved by the ν_e appearance search in the MINOS experiment, using the technique of predicting intrinsic-beam and neutral current (NC) background levels from near detector measurements. The LBNE far detector should be able to provide additional constraints on the background level by independently measuring NC and ν_τ background.

In Figure 4.10, the MH and CP-violation sensitivities as a function of exposure are evaluated using three different sets of assumptions regarding the uncorrelated ν_e signal/background normalization uncertainties: 1%/5% (the goal of the LBNE scientific program), 2%/5% and 5%/10%. The last is a conservative estimate of the uncertainties that can be achieved in LBNE without unoscillated neutrino beam measurements at the near site. The impact of signal and background normalization uncertainties on the MH sensitivity is small even at high exposures given the large $\nu/\overline{\nu}$ asymmetry at 1,300 km and the fact that much of the sensitivity to the MH comes from analysis of the spectral shapes (Figure 4.9). For CP violation, however, the impact of normalization uncertainties is significant at exposures ≥ 100 kt · MW · years.

Table 4.7 summarizes the LBNE exposures required to reach 3σ and 5σ sensitivity to CP violation for at least 50% of all possible values of $\delta_{\rm CP}$. The exposures vary depending on the assumptions made about the normalization uncertainties that can be achieved in LBNE. The normalization un-

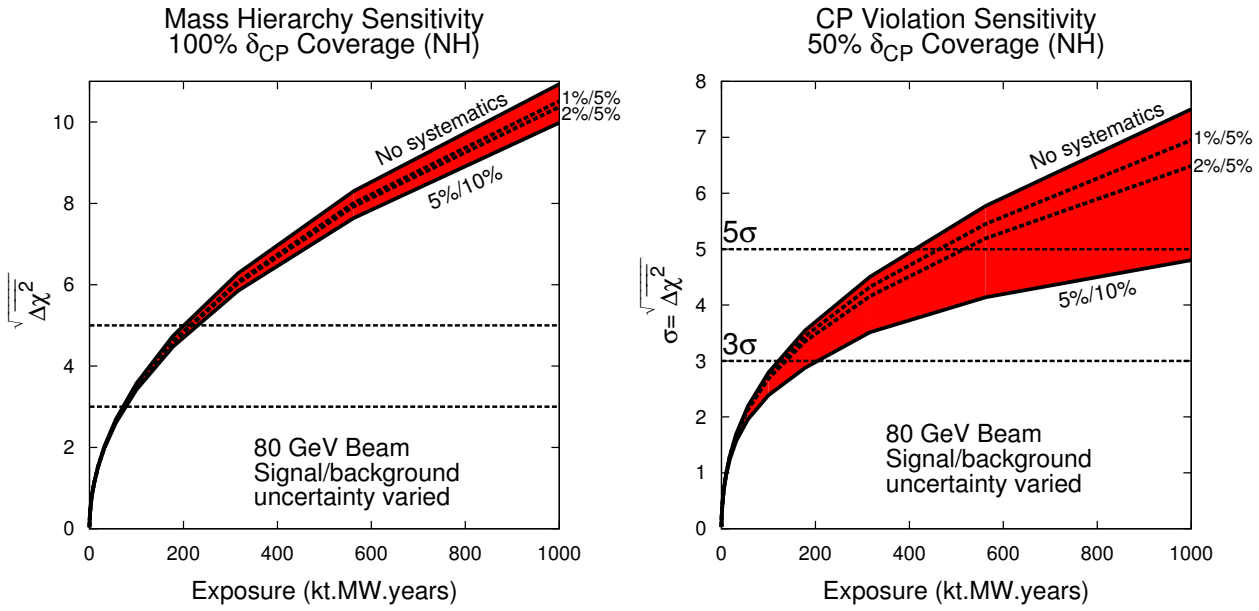

Figure 4.10: The mass hierarchy (left) and CP violation (right) sensitivities as a function of exposure in kt · year, for true normal hierarchy. The band represents the range of signal and background normalization errors.

Table 4.7: The exposures required to reach 3σ and 5σ sensitivity to CP violation for at least 50% of all possible values of $\delta_{\rm CP}$ as a function of systematic uncertainties assumed on the ν_e appearance signal. The uncertainties varied are the uncorrelated signal normalization uncertainty (Sig) and the background normalization uncertainty (Bkgd).

Systematic uncertainty	**CPV Sensitivity**		**Required Exposure**
	$\delta_{\rm CP}$ Fraction	**($\sqrt{\Delta\chi^2}$)**	
0 (statistical only)	50% $\delta_{\rm CP}$	3 σ	100 kt · MW · year
	50% $\delta_{\rm CP}$	5 σ	400 kt · MW · year
1%/5% (Sig/bkgd)	50% $\delta_{\rm CP}$	3 σ	100 kt · MW · year
	50% $\delta_{\rm CP}$	5 σ	450 kt · MW · year
2%/5% (Sig/bkgd)	50% $\delta_{\rm CP}$	3 σ	120 kt · MW · year
	50% $\delta_{\rm CP}$	5 σ	500 kt · MW · year
5%/10% (no near ν det.)	50% $\delta_{\rm CP}$	3 σ	200 kt · MW · year

certainty assumptions range from 1-2%/5% on signal/background to 5%/10%. The uncertainties listed in Table 4.7 and shown in the sensitivity figures pertain to the ν_e appearance signal and background normalization. In Figure 4.9 the sensitivities obtained from the rate only, shape only and rate+shape of the appearance spectrum are shown for a 10-kt detector with an 80-GeV beam. For CP violation (right), the rate information dominates the sensitivity, but the shape information enables the detector to exceed 3σ sensitivity for large CP violation. For the MH sensitivity, Figure 4.9 (left) demonstrates that the sensitivity in the least favorable range of $\delta_{\rm CP}$ values is dominated by the shape information. Further analysis has shown that it is the region of the second oscillation node

that is responsible for this effect. The shape of the signal in this region will enable LBNE to determine the sign of $\delta_{\rm CP}$, which is sufficient to break the degeneracy with MH effects and determine the correct sign of the mass ordering.

Figures 4.11, 4.12, and 4.13 show the variation in sensitivity to CP violation and MH when the true value of the oscillation parameters θ_{13}, θ_{23} and Δm^2_{31} are varied within the 3σ range allowed by the 2012 3ν global fit [17]. These sensitivities are calculated for six years with equal exposures in ν and $\overline{\nu}$ mode in a 1.2-MW beam for the case in which an upgraded 80-GeV beam and a near detector have both been implemented.

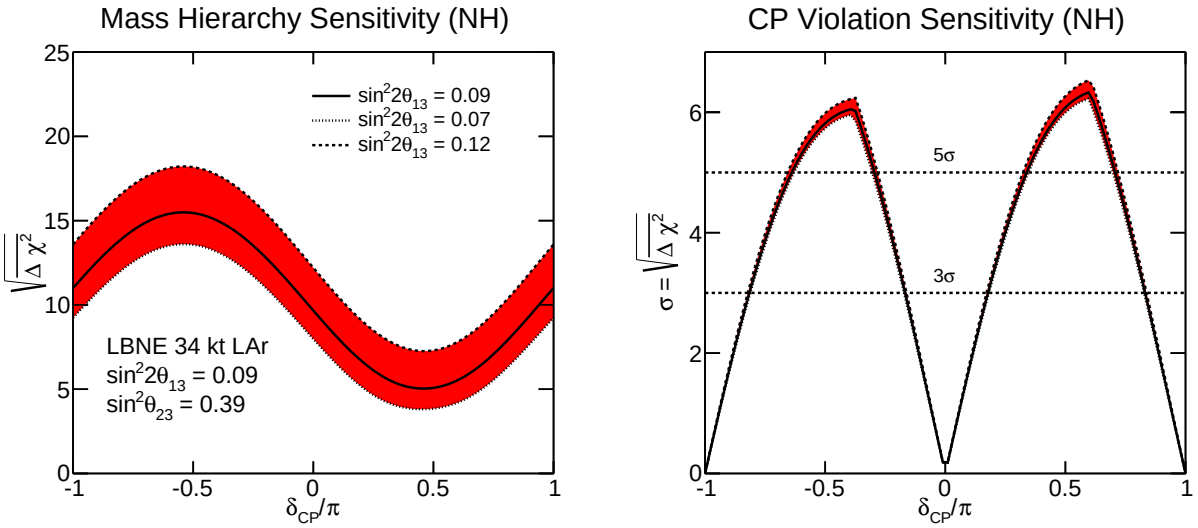

Figure 4.11: The significance with which the mass hierarchy (left) and CP violation, i.e., $\delta_{\rm CP} \neq 0$ or π, (right) can be determined by a typical LBNE experiment as a function of the value of $\delta_{\rm CP}$ for an allowed range of θ_{13} values and for normal hierarchy; assumes a 34-kt far detector.

In comparing Figures 4.11, 4.12 and 4.13, the dependence on the true value of θ_{23} is particularly striking. As $\sin^2\theta_{23}$ increases, the sensitivity to CP violation decreases because the CP asymmetry that LBNE measures is inversely proportional to $|\sin\theta_{23}|$ as demonstrated in Equation 2.20. For the same reason, as θ_{23} increases, the degeneracy between the CP and matter asymmetries is broken, which increases the LBNE sensitivity to neutrino MH. The explicit dependence of MH sensitivity on the value of $\sin^2\theta_{23}$ is shown in Figure 4.14. As this plot makes clear, LBNE resolves the MH with a significance of $\sqrt{\overline{\Delta\chi^2}} > 6$ for nearly all allowed values of $sin^2\theta_{23}$ and $\delta_{\rm CP}$.

4.3.3 Summary of CP-Violation and Mass Hierarchy Sensitivities

For the 10-kt LBNE, the statistical uncertainties are much larger than the systematic uncertainties. Combining the sensitivity from the 10-kt LBNE with expected knowledge from the NOνA and T2K experiments would allow LBNE to achieve a $\geq 4\sigma$ sensitivity for detecting CP violation for 30% of the allowed values of $\delta_{\rm CP}$ and a $\geq 3\sigma$ sensitivity for 50% of these values. It is clear that

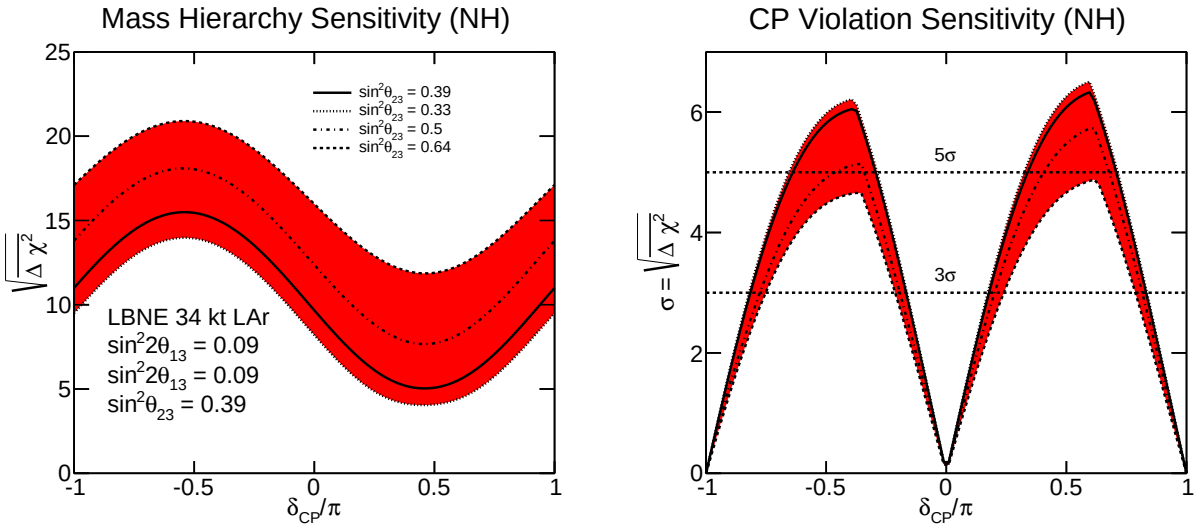

Figure 4.12: The significance with which the mass hierarchy (left) and CP violation, i.e., $\delta_{\rm CP} \neq 0$ or π, (right) can be determined by a typical LBNE experiment as a function of the value of $\delta_{\rm CP}$ for an allowed range of θ_{23} values and for normal hierarchy; assumes a 34-kt far detector.

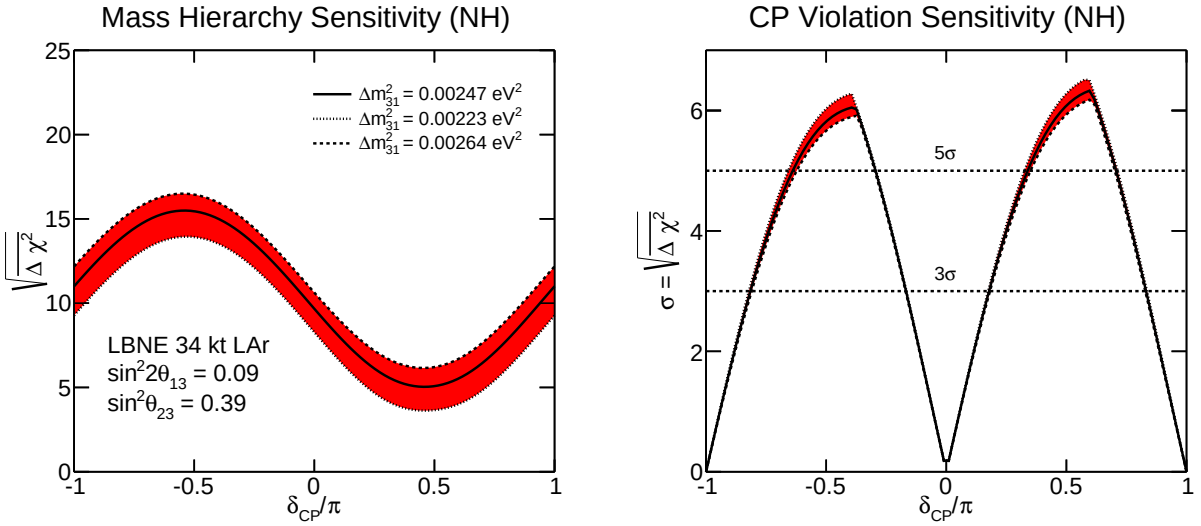

Figure 4.13: The significance with which the mass hierarchy (left) and CP violation, i.e., $\delta_{\rm CP} \neq 0$ or π, (right) can be determined by a typical LBNE experiment as a function of the value of $\delta_{\rm CP}$ for an allowed range of Δm^2_{31} values and for normal hierarchy; assumes a 34-kt far detector.

the 10-kt LBNE sensitivity would be the dominant contribution in the combined sensitivities and would therefore represent a significant advance in the search for leptonic CP violation over the current generation of experiments, particularly in the region where the CP and matter effects are degenerate.

The combination with T2K and NOνA would allow the MH to be determined with a *minimum* precision of $|\overline{\Delta\chi^2}| \geq 25$ over 60% $\delta_{\rm CP}$ values and $|\overline{\Delta\chi^2}| \geq 16$ for all possible values of $\delta_{\rm CP}$. Due to the low event statistics in these experiments, the combination with NOνA and T2K only helps

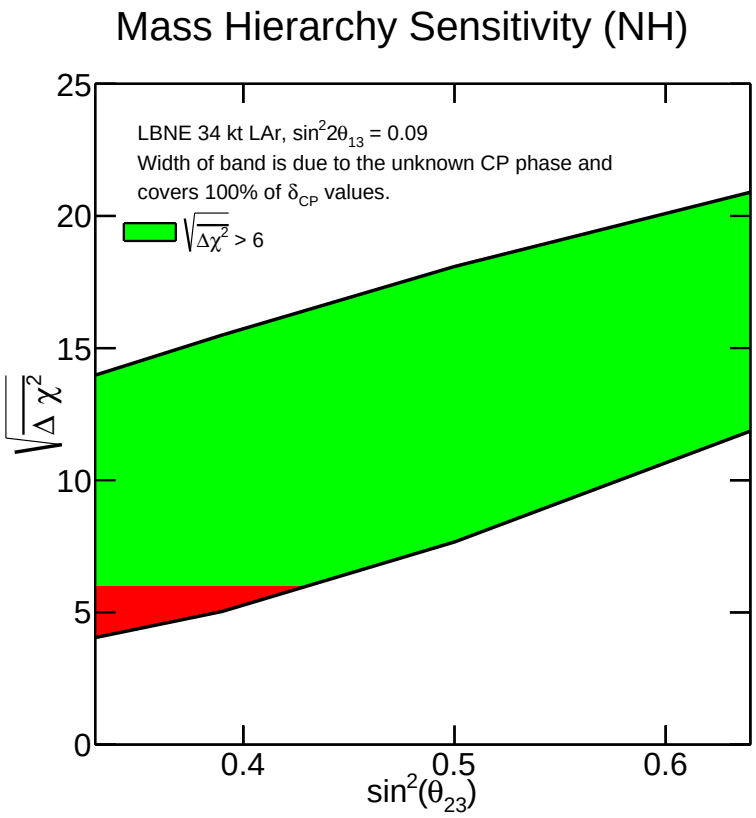

Figure 4.14: The significance with which the MH can be determined by a typical LBNE experiment as a function of the value of $\sin^2\theta_{23}$, for the 3σ allowed range of $\sin^2\theta_{23}$, for true normal hierarchy. The width of the band is due to the unknown value of $\delta_{\rm CP}$ and covers all possible values of $\delta_{\rm CP}$. The green region shows the parameter space for which $\sqrt{\Delta\chi^2} > 6$. Assumes a 34-kt far detector with 6 years of running in a 1.2 MW beam.

the sensitivity in the region of $\delta_{\rm CP} > 0$ (NH) or $\delta_{\rm CP} < 0$ (IH) where there are residual degeneracies between matter and CP-violating effects. As will be discussed in Section 4.6, the combination with atmospheric neutrino oscillation studies can also be used to improve the MH sensitivity in this region for the LBNE 10-kt configuration.

Assuming the normal hierarchy, the most recent global fit of experimental data for the three-neutrino paradigm favors a value of $\delta_{\rm CP}$ close to $-\pi/2$ with $\sin\delta_{\rm CP} < 0$ at a confidence level of $\sim 90\%$ [32] (Figure 4.15). LBNE alone with a 10-kt detector and six years of running would resolve with $\geq 3\sigma$ precision the question of whether CP is violated for the currently favored value of $\delta_{\rm CP}$. With a 34-kt detector running for six years, LBNE, alone will achieve a precision approaching 6σ.

Table 4.8 summarizes the MH and CP sensitivities that can be reached by a typical experiment with the LBNE 10-kt and 34-kt configurations assuming a running time of 3+3 ($\nu + \overline{\nu}$) years with a 1.2-MW beam under a variety of scenarios.

Table 4.8: The mass hierarchy and CP violation sensitivities that can be reached with a typical data set from the LBNE 10-kt and 34-kt configurations with a 1.2 MW beam, no near neutrino detector (ND) unless otherwise stated, and a run time of 3+3 $\nu + \overline{\nu}$ years under a variety of beam and systematic scenarios, for normal hierarchy. Note that the sensitivities for inverted hierarchy are similar but not identical. As discussed in the text, the significance of the MH determination should not be interpreted using Gaussian probabilities.

Scenario ($\sin^2\theta_{23} = 0.39$)	**MH sensitivity**		**CPV sensitivity**	
	δ_{CP} Fraction	**($\sqrt{\Delta\chi^2}$)**	**δ_{CP} Fraction**	**($\sqrt{\Delta\chi^2}$)**
LBNE 10 kt, CDR beam	50%	≥ 4	40%	$\geq 2\sigma$
	100%	≥ 2	-	-
LBNE 10 kt, 80-GeV upgraded beam	50%	≥ 5	23%	$\geq 3\sigma$
	100%	≥ 3	55%	$\geq 2\sigma$
LBNE 10 kt, 80-GeV beam, with ν ND	50%	≥ 5	33%	$\geq 3\sigma$
	100%	≥ 3	60%	$\geq 2\sigma$
+ NOνA (6 yrs), T2K (7.8×10^{21} POT)	75%	≥ 5	30%	$\geq 4\sigma$
	100%	≥ 4	50%	$\geq 3\sigma$
LBNE 34 kt , CDR beam	50%	≥ 7	20%	$\geq 4\sigma$
	100%	≥ 4	50%	$\geq 3\sigma$
LBNE 34 kt, 80-GeV upgraded beam	50%	≥ 8	15%	$\geq 5\sigma$
	100%	≥ 5	35%	$\geq 4\sigma$
LBNE 34 kt, 80-GeV beam, with ν ND	50%	≥ 9	35%	$\geq 5\sigma$
	100%	≥ 5	50%	$\geq 4\sigma$

4.3.4 CP-Violating and Mass Hierarchy Sensitivities with Increased Exposures

Figure 4.16 shows the minimum significance with which the MH can be resolved and CP violation determined by LBNE as a function of increased exposure in units of mass × beam power × time[§]. For this study, the LBNE beamline improvements discussed in Section 3.4 are used with $E_p = 80\,\text{GeV}$, and the signal and background normalization uncertainties are assumed to be 1% and 5%, respectively. Both ν_e and ν_μ appearance signals are used in a combined analysis. Due to the long baseline, the determination of the MH in LBNE to high precision does not require a large exposure; a sensitivity of $\sqrt{\Delta\chi^2} = 5$ for the worst case (NH, $\delta_{CP} = \pi/2$ or IH, $\delta_{CP} = -\pi/2$) requires an exposure of $\sim 200\,\text{kt}\cdot\text{MW}\cdot\text{years}$, but $\sqrt{\Delta\chi^2} = 5$ sensitivity can be reached for 50% of the allowed values of δ_{CP} with an exposure of less than $100\,\text{kt}\cdot\text{MW}\cdot\text{years}$. On the other hand, reaching discovery-level sensitivity ($\geq 5\sigma$) to leptonic CP violation for at least 50% of the possible values of δ_{CP} will require large exposures of $\approx 450\,\text{kt}\cdot\text{MW}\cdot\text{years}$. Figure 4.17 demonstrates the

[§]Time is denoted in years of running at Fermilab. One year of running at Fermilab corresponds to $\approx 1.7\times10^7$ seconds.

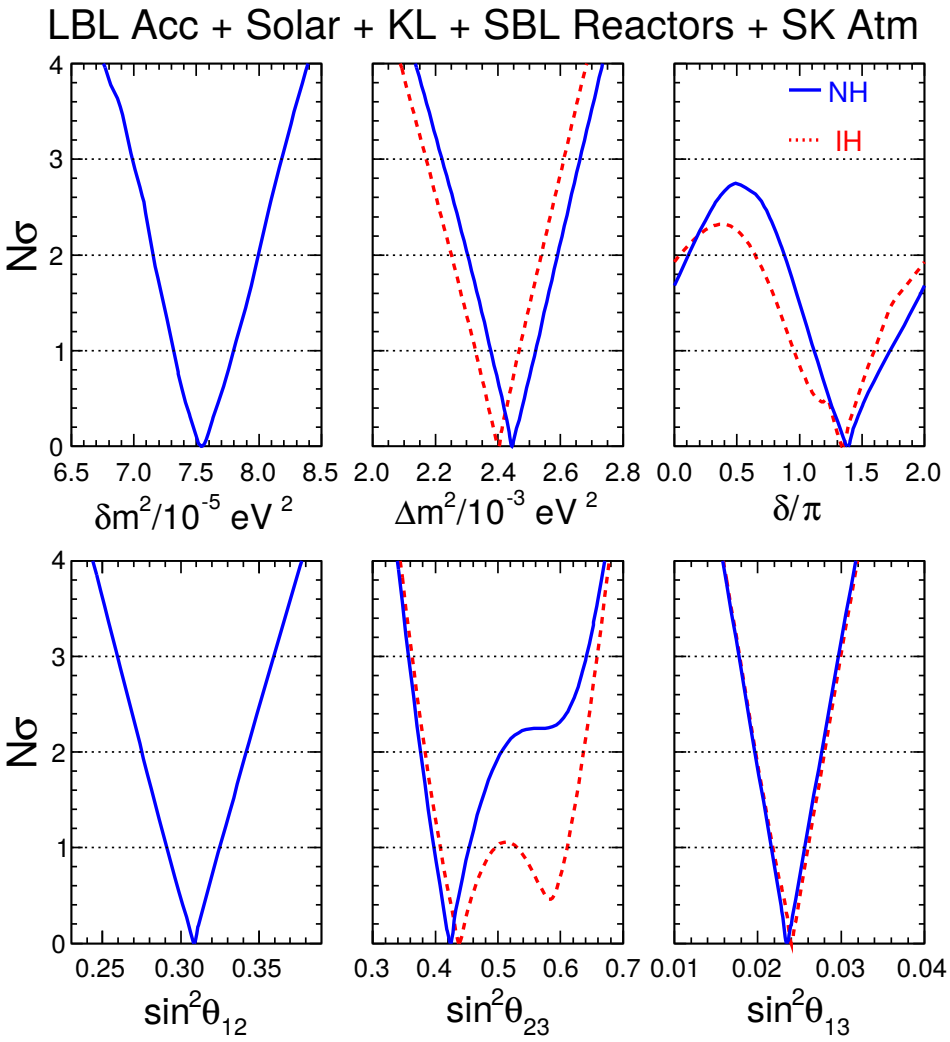

Figure 4.15: Results of the 2013 global analysis from Capozzi *et al.* shown as Nσ bounds on the six parameters governing three ν flavor oscillations. Blue (solid) and red (dashed) curves refer to NH and IH, respectively. Figure is from [32].

sensitivity to CP violation as a function of $\delta_{\rm CP}$ and exposure that can be achieved with various stages of the Fermilab Proton-Improvement-Plan (PIP-II and upgrades to PIP-II). In this study, the PIP-II upgrades are assumed to provide LBNE with 1.2 MW[¶] at 80 GeV, followed by further upgrades in which the booster is replaced with a linac that will provide 2.3 MW from the Main Injector (MI), also at 80 GeV. The study demonstrates that it is possible to reach 5σ sensitivity to CP violation over at least 40% of $\delta_{\rm CP}$ values running for a little over 10 years, starting with the PIP-II MI power and a LArTPC greater than 10 kt, and phasing in more detector mass. Other possible staging scenarios of detector mass and beam power are discussed in Chapter 9.

[¶]The assumed exposures are only accurate to the level of 15% due to incomplete knowledge of the PIP-II final design parameters and running conditions.

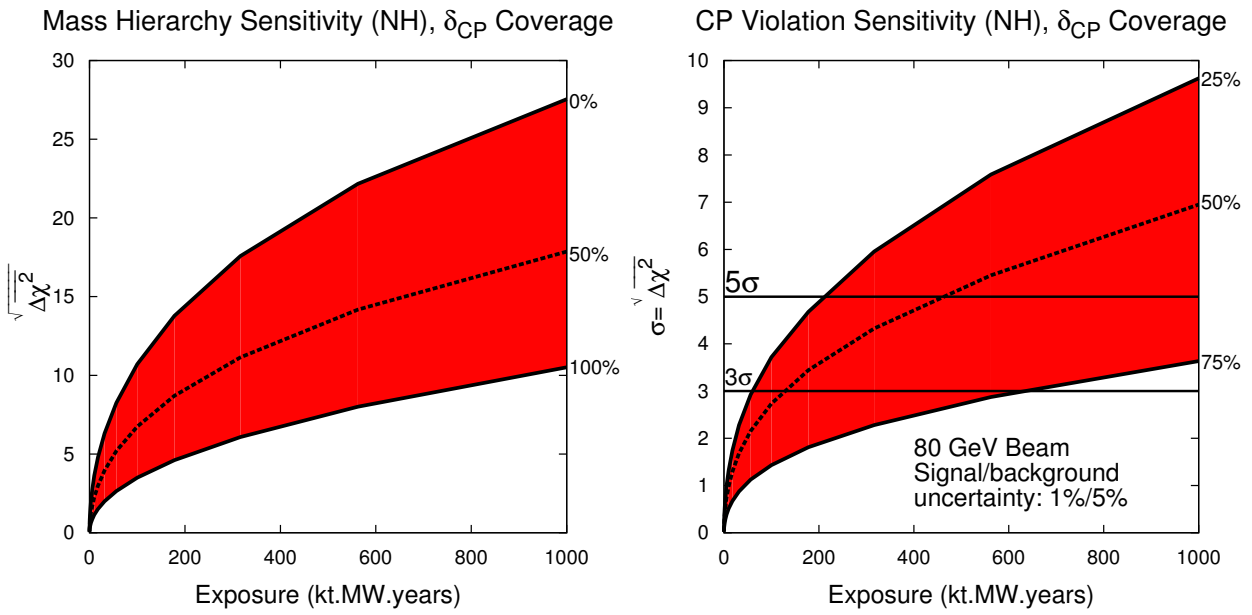

Figure 4.16: The minimum significance with which the mass hierarchy (left) and CP violation (right) can be resolved as a function of exposure in detector mass (kiloton) × beam power (MW) × time (years), for true NH. The red band represents the fraction of $\delta_{\rm CP}$ values for which the sensitivity can be achieved with at least the minimal significance on the y-axis.

Table 4.9: The CP violation sensitivities that can be reached by LBNE alone starting with the LBNE 10-kt configuration with a 1.2-MW beam and a run time of 3+3 ($\nu+\overline{\nu}$) years and phasing in additional far detector mass and beam power upgrades beyond the current PIP-II. In all cases, the sensitivities are calculated using the 80 GeV upgraded beam and 1%/5% signal/background normalization uncertainties, for true normal hierarchy. The sensitivity for each stage includes exposure from the previous stage(s) of the experiment.

Exposure	**Possible Scenario**	**CPV sensitivity**	
		$\delta_{\rm CP}$ Fraction	**($\sqrt{\Delta\chi^2}$)**
60 kt · years 1.2 MW beam	PIP-II, 10 kt, 6 years	60% $\delta_{\rm CP}$	$\geq 2\sigma$
		33% $\delta_{\rm CP}$	$\geq 3\sigma$
+ 200 kt · years 1.2 MW beam	PIP-II, 34 kt, 6 years	40% $\delta_{\rm CP}$	$\geq 5\sigma$
+ 200 kt · years 2.3 MW beam	Booster replaced, 34 kt, 6 years	60% $\delta_{\rm CP}$	$\geq 5\sigma$

4.4 Measurement of θ_{23} and Determination of the Octant

The value of $\sin^2 2\theta_{23}$ is measured to be > 0.95 at 90% CL using atmospheric neutrino oscillations [45]. This corresponds to a value of θ_{23} near 45°, but leaves an ambiguity as to whether the value of θ_{23} is in the lower octant (less than 45°), the upper octant (greater than 45°) or exactly 45°. The value of $\sin^2\theta_{23}$ from the 2013 global fit reported by [32] is $\sin^2\theta_{23} = 0.425^{+0.029}_{-0.027}(1\sigma)$ for normal hierarchy (NH), but as shown in Figure 4.15, the distribution of the χ^2 from the global fit has another local minimum — particularly if the MH is inverted — at $\sin^2\theta_{23} \approx 0.59$. A *maximal* mixing value of $\sin^2\theta_{23} = 0.5$ is therefore still allowed by the data and the octant is still largely

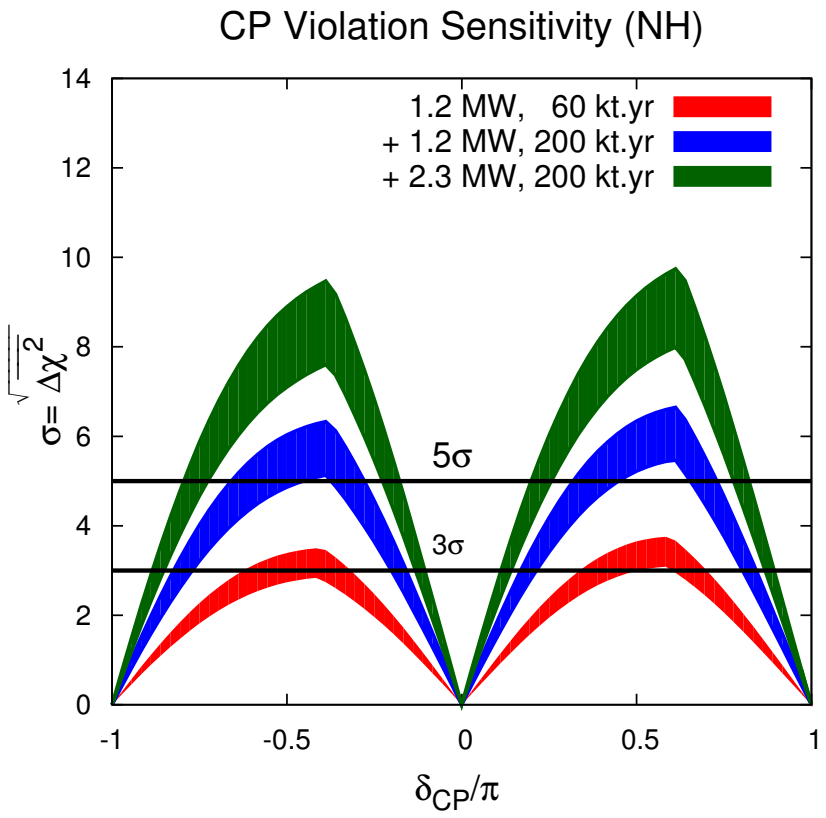

Figure 4.17: The significance with which CP violation — $\delta_{\rm CP} \neq 0$ or π — can be determined as a function of $\delta_{\rm CP}$. The different color curves represent possible exposures from different stages of PIP and detector mass upgrades as follows: 1.2 MW, 60 kt·years (red) + 1.2 MW, 200 kt·years (blue) + 2.3 MW, 200 kt·years (green). The sensitivity for each higher exposure is in addition to that from all lower exposures. The bands represent the range of sensitivities obtained from the improvements to the CDR beamline design.

undetermined. As discussed in Chapter 2, a value of θ_{23} exactly equal to 45° would indicate that ν_μ and ν_τ have equal contributions from ν_3, which could be evidence for a previously unknown symmetry. It is therefore important experimentally to determine the value of $\sin^2\theta_{23}$ with sufficient precision to determine the octant of θ_{23}.

The measurement of $\nu_\mu \rightarrow \nu_\mu$ oscillations is sensitive to $\sin^2 2\theta_{23}$, whereas the measurement of $\nu_\mu \rightarrow \nu_e$ oscillations is sensitive to $\sin^2\theta_{23}$. A combination of both ν_e appearance and ν_μ disappearance measurements can probe both maximal mixing and the θ_{23} octant. With the large statistics and rich spectral structure in a wide-band, long-baseline experiment such as LBNE (Figure 4.2), precision measurements of $\sin^2\theta_{23}$ can be significantly improved compared to existing experiments, particularly for values of θ_{23} near 45°. Figure 4.18 demonstrates the measurement precision of θ_{23} and Δm^2_{31} that can be achieved for different true values of these parameters by a 10-kt LBNE detector. The subdominant $\nu_\mu \rightarrow \nu_e$ appearance signal in a 10-kt detector is limited by statistical uncertainties.

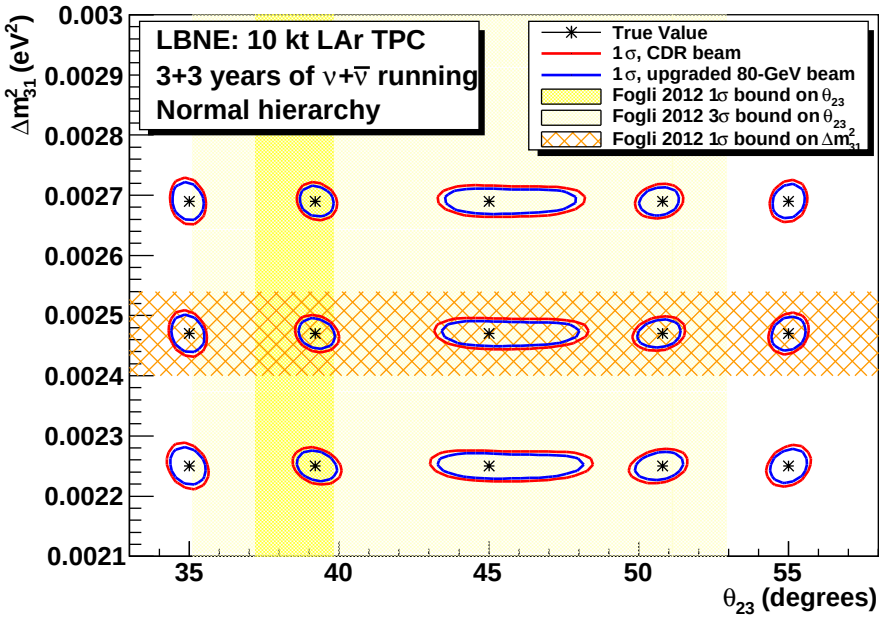

Figure 4.18: The precision with which a simultaneous measurement of θ_{23} and Δm^2_{31} can be determined with 10 kt and 3+3 years of $\nu + \overline{\nu}$ running in a 1.2-MW beam. The yellow bands represent the 1σ and 3σ allowed ranges of θ_{23} and the orange hatched region represents the 1σ allowed range of Δm^2_{31} from [17].

The significance with which a 10-kt LBNE detector can determine the θ_{23} octant is shown in the top plot of Figure 4.19. The $\Delta\chi^2$ metric is defined as:

$$\Delta\chi^2_{octant} \quad = \quad |\chi^2_{\theta_{23}^{test}>45^\circ} - \chi^2_{\theta_{23}^{test}<45^\circ}|, \tag{4.9}$$

where the value of θ_{23} in the *wrong* octant is constrained only to have a value within the *wrong* octant (i.e., it is not required to have the same value of $\sin^2 2\theta_{23}$ as the true value). The individual χ^2 values are given by Equation 4.4. As in the $\Delta\chi^2$ metrics for MH and CP violation, the χ^2 value for the *true* octant is identically zero in the absence of statistical fluctuations. If θ_{23} is within the 1σ bound of the global fit [17], an LBNE 10-kt detector alone will determine the octant with $> 3\sigma$ significance for all values of $\delta_{\rm CP}$. Figure 4.19 (bottom) demonstrates the increasing sensitivity to the θ_{23} octant for values closer to maximal ν_μ-ν_τ mixing that can be achieved with subsequent phases of LBNE coupled with upgrades in beam power from the Main Injector.

With sufficient exposure, LBNE can resolve the θ_{23} octant with $> 3\sigma$ significance even if θ_{23} is within a few degrees of 45°, the value at which the mixing between the ν_μ and ν_τ neutrino states is maximal.

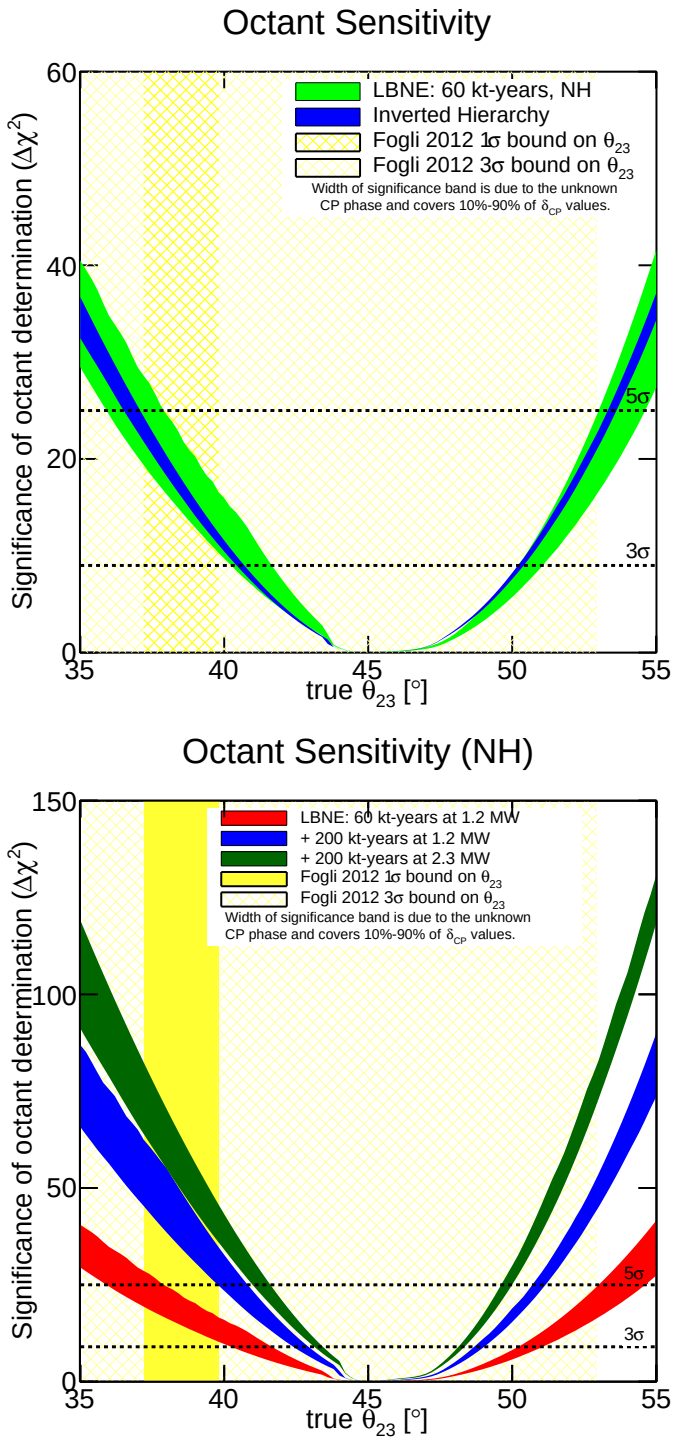

Figure 4.19: Top: significance with which LBNE can resolve the θ_{23} octant degeneracy for 3+3 years of ν+$\overline{\nu}$ running at 1.2 MW with a 10-kt detector. The bands are for normal (green) and inverted (blue) hierarchy. The widths of the bands correspond to the fraction of $\delta_{\rm CP}$ values covered at this significance or higher, ranging from 10% to 90%. The yellow bands represent the 1σ and 3σ allowed ranges of θ_{23} from [17]. Bottom: significance with which LBNE can resolve the θ_{23} octant degeneracy (normal hierarchy) for equal ν+$\overline{\nu}$ running with increased exposure. The colored bands represent increasing exposures as follows: 1.2 MW, 60 kt·year (red) + 1.2 MW, 200 kt·years (blue) + 2.3 MW, 200 kt·years (green). The sensitivity for each higher exposure is in addition to that from all lower exposures.

4.5 Precision Measurements of the Oscillation Parameters in the Three-Flavor Model

The rich oscillation structure that can be observed by LBNE and the excellent particle identification capability of the detector will enable precision measurement in a single experiment of all the mixing parameters governing ν_1-ν_3 and ν_2-ν_3 mixing. As discussed in Chapter 2, theoretical models probing quark-lepton universality predict specific values of the mixing angles and the relations between them. The mixing angle θ_{13} is expected to be measured accurately in reactor experiments by the end of the decade with a precision that will be limited by systematics. The systematic uncertainty on the value of $\sin^2 2\theta_{13}$ from the Daya Bay reactor neutrino experiment, which has the lowest systematics, is currently $\sim 4\%$ [19].

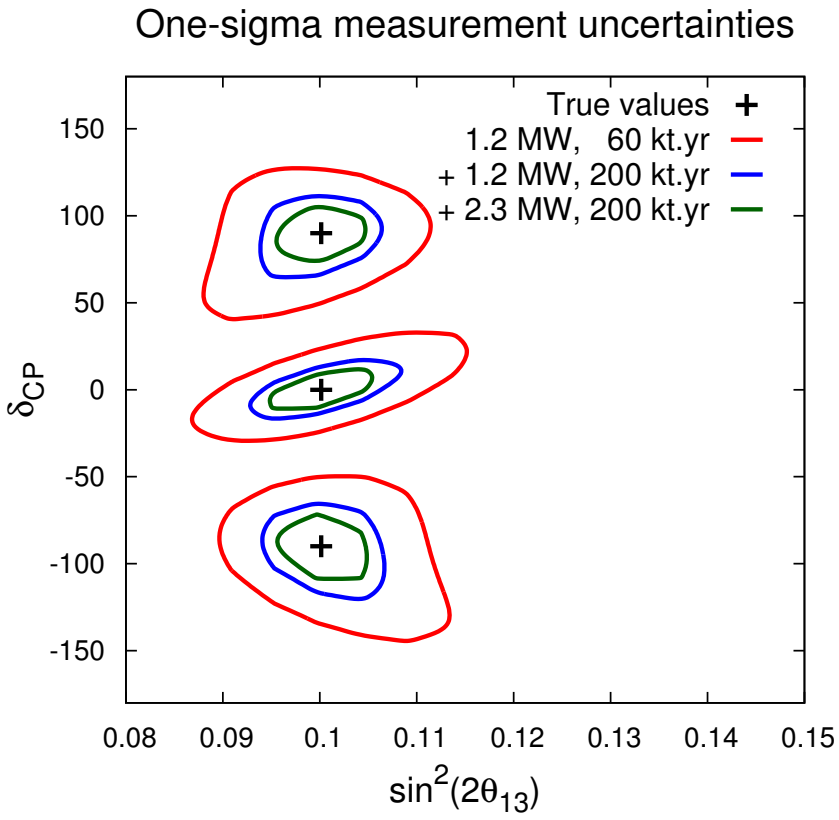

Figure 4.20: Measurement of $\delta_{\rm CP}$ and θ_{13} in LBNE with different exposures, for true normal hierarchy (NH). The different color curves represent one-sigma contours for three possible exposures from different stages of PIP and detector mass upgrades as follows: 1.2 MW, 60 kt·year (red), 1.2 MW, 200 kt·years (blue) + 2.3 MW, 200 kt·years (green). The sensitivity for each higher exposure is in addition to that from all lower exposures.

While the constraint on θ_{13} from the reactor experiments will be important in the early stages of LBNE for determining CP violation, measuring $\delta_{\rm CP}$ and determining the θ_{23} octant, LBNE

itself will eventually be able to measure θ_{13} independently with a precision on par with the final precision expected from the reactor experiments. Whereas the reactor experiments measure θ_{13} using $\overline{\nu}_e$ disappearance, LBNE will measure it through ν_e and $\overline{\nu}_e$ appearance, thus providing an independent constraint on the three-flavor mixing matrix. Figure 4.20 demonstrates the precision with which LBNE can measure $\delta_{\rm CP}$ and θ_{13} simultaneously, with no external constraints on θ_{13}, as a function of increased exposure, for three different exposures. Both appearance and disappearance modes are included in the fit using the upgraded 80-GeV beam. Signal/background normalization uncertainties of 1%/5% are assumed.

Figure 4.21 shows the expected 1σ resolution on different three-flavor oscillation parameters as a function of exposure in kt · year in a 1.2-MW beam with LBNE alone and LBNE in combination with the expected performance from T2K and NOνA. It should be noted that LBNE alone could reach a precision on $\sin^2 2\theta_{13}$ of 0.005 with an exposure of $\sim$300 kt · MW · years. LBNE can also significantly improve the resolution on Δm^2_{32} beyond what the combination of NOνA and T2K can achieve, reaching a precision of 1×10^{-5} eV^2 with an exposure of $\sim$300 kt · MW · years. The precision on Δm^2_{32} will ultimately depend on tight control of energy-scale systematics. Initial studies of the systematics reveal that the measurement of ν_μ disappearance in LBNE over a full oscillation interval, with two oscillation peaks and two valleys (Figure 4.2), reduces the dependency of the Δm^2_{23} measurement on the energy-scale systematics, which limited the measurement precision in MINOS [42].

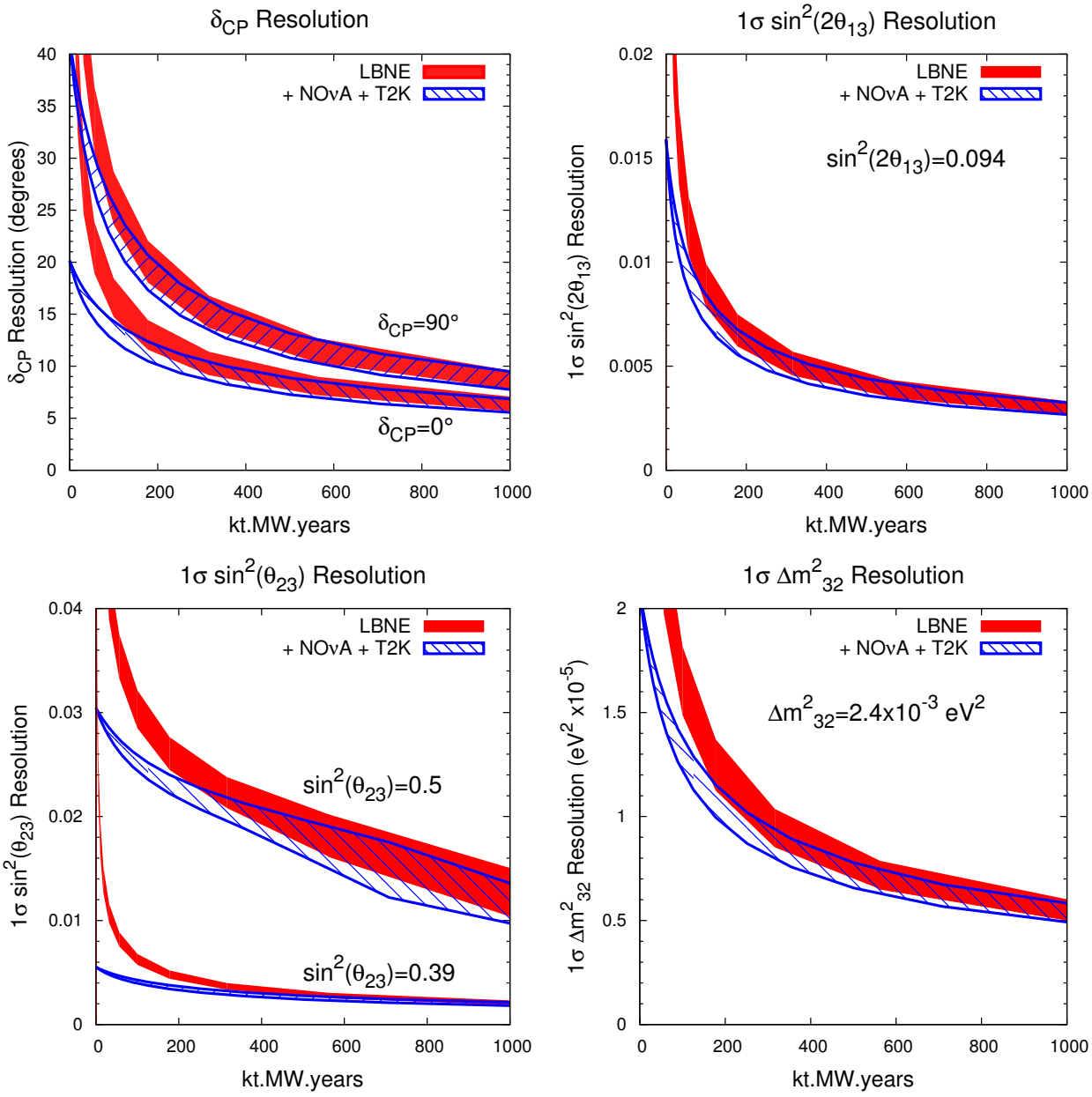

Figure 4.21: The expected 1σ resolution on different three-flavor oscillation parameters as a function of exposure in kt · MW · years, for true NH. The red curve indicates the precision that could be obtained from LBNE alone, and the blue curve represents the combined precision from LBNE and the T2K and NOνA experiments. The width of the bands represents the range of performance with the beam improvements under consideration.

4.6 Oscillation Studies Using Atmospheric Neutrinos

Atmospheric neutrinos are unique among sources used to study oscillations: the flux contains neutrinos and antineutrinos of all flavors, matter effects play a significant role, both Δm^2 values contribute, and the oscillation phenomenology occurs over several orders of magnitude each in energy (Figure 2.8) and path length. These characteristics make atmospheric neutrinos ideal for the study of oscillations (in principle sensitive to all of the remaining unmeasured quantities in the PMNS matrix) and provide a laboratory in which to search for exotic phenomena for which the dependence of the flavor-transition and survival probabilities on energy and path length can be defined. The large LBNE LArTPC far detector, placed at sufficient depth to shield against cosmic-ray background, provides a unique opportunity to study atmospheric neutrino interactions with excellent energy and path-length resolutions.

LBNE has obtained far detector physics sensitivities based on information from atmospheric neutrinos by using a Fast MC and a three-flavor analysis framework developed for the MINOS experiment [46]. Four-vector-level events are generated using the GENIE neutrino event generator [5]. For atmospheric neutrinos the Bartol [47] flux calculation for the Soudan, MN site was used, and for beam neutrinos the 80-GeV, 1.2-MW beamline design described in Section 3.4 was used. In this section, unless otherwise specified, the oscillation parameters are as specified in Table 4.10.

Table 4.10: Oscillation parameters used in the atmospheric-neutrino analysis.

Parameter	Value
$\Delta m^2 = 1/2(\Delta m^2_{32} + \Delta m^2_{31})$ (NH)	$+2.40 \times 10^{-3}$ eV^2
$\sin^2\theta_{23}$	0.40
Δm^2_{21}	7.54×10^{-5} eV^2
$\sin^2\theta_{12}$	0.307
$\sin^2\theta_{13}$	0.0242
δ_{CP}	0

The expected interaction rates in 100 kt · year are shown in Table 4.11. All interactions occur on argon and are distributed uniformly throughout a toy detector geometry consisting of two modules, each 14.0 m high, 23.3 m wide, and 45.4 m long. For this study, events with interaction vertices outside the detector volume (e.g., events that produce upward-going stopping or through-going muons) have not been considered. Cosmogenic background has not been studied in detail, but since atmospheric neutrinos are somewhat more tolerant of background than proton decay, a depth that is sufficient for a proton decay search is expected to also be suitable for studies of atmospheric

neutrinos. Given the detector's 4,850-ft depth, a veto should not be necessary and the full fiducial mass of the detector should be usable.

Table 4.11: Expected atmospheric ν interaction rates in a LArTPC with an exposure of 100 kt · years for the Bartol flux and GENIE argon cross sections (no oscillations).

Flavor	CC	NC	Total
ν_μ	10,069	4,240	14,309
$\overline{\nu}_\mu$	2,701	1,895	4,596
ν_e	5,754	2,098	7,852
$\overline{\nu}_e$	1,230	782	2,012
Total:	**19,754**	**9,015**	**28,769**

A Fast MC runs on the produced four-vectors, placing events into containment and flavor categories. Containment is evaluated by tracking leptons through the liquid argon detector box geometry and classifying events as either fully contained (FC) or partially contained (PC). A detection threshold of 50 MeV is assumed for all particles. Flavor determination, in which events are placed into electron-like or muon-like categories, is based on properties of the primary and secondary particles above detection threshold. Electrons are assumed to be correctly identified with 90% probability and other electromagnetic particles (e.g., π^0, γ) are misidentified as electrons 5% of the time. Muons are identified with 100% probability and charged pions are misidentified as muons 1% of the time. Events in which neither of the two leading particles is identified as a muon or electron are placed into an *NC-like* category. With these assumptions, the purities of the flavor-tagged samples are 97.8% for the FC electron-like sample, 99.7% for the FC muon-like sample, and 99.6% for the PC muon-like sample. The NC-like category is not used in this analysis, but would be useful for ν_τ appearance studies. The energy and direction of the event are then assigned by separately smearing these quantities of the leptonic and hadronic systems, where the width of the Gaussian resolution

Table 4.12: Detector performance assumptions for the atmospheric neutrino and the combined atmospheric+beam neutrino analyses.

Particle	Resolution
Angular Resolutions	
Electron	1°
Muon	1°
Hadronic System	10°
Energy Resolutions	
Stopping Muon	3%
Exiting Muon	15%
Electron	$1\%/\sqrt{E(GeV)} \oplus 1\%$
Hadronic System	$30\%/\sqrt{E(GeV)}$

functions for each flavor/containment category are given in Table 4.12. Detector performance assumptions are taken both from the LBNE CDR [13] and from published results from the ICARUS experiment [14,48,49,50]. Including oscillations, the expected number of events in 100 kt · year is summarized in Table 4.13.

Table 4.13: Atmospheric-neutrino event rates including oscillations in 100 kt · year with a LArTPC, fully or partially contained in the detector fiducial volume.

Sample	Event rate
fully contained electron-like sample	4,015
fully contained muon-like sample	5,958
partially contained muon-like sample	1,963

Figure 4.22 shows the expected L/E distribution for *high-resolution* muon-like events from a 350 kt · year exposure; the latest data from Super-Kamiokande are shown for comparison. LBNE defines high-resolution events similarly to Super-Kamiokande, i.e., either by excluding a region of low-energy events or events pointing toward the horizon where the baseline resolution is poor. The data provide excellent resolution of the first two oscillation nodes, even when taking into account the expected statistical uncertainty.

In performing oscillation fits, the data in each flavor/containment category are binned in energy and zenith angle. Figure 4.23 shows the zenith angle distributions for several ranges of reconstructed energy, where oscillation features are clearly evident.

The power to resolve the mass hierarchy (MH) with atmospheric neutrinos comes primarily from the MSW enhancement of few-GeV neutrinos at large zenith angles. This enhancement occurs for neutrinos in the normal hierarchy and antineutrinos in the inverted hierarchy. Figure 4.24 shows zenith angle distributions of events in the relevant energy range for each of the three flavor/containment categories. Small differences are evident in comparing the NH and IH predictions.

Since the resonance peak occurs for neutrinos in the NH and antineutrinos in the IH, the MH sensitivity can be greatly enhanced if neutrino and antineutrino events can be separated. The LBNE detector will not be magnetized; however, its high-resolution imaging offers possibilities for tagging features of events that provide statistical discrimination between neutrinos and antineutrinos. For the sensitivity calculations that follow, two such tags are included: a proton tag and a decay-electron tag. For low-multiplicity events, protons occur preferentially in neutrino interactions; protons are tagged with 100% efficiency if their kinetic energy is greater than 50 MeV. Decay electrons are assumed to be 100% identifiable and are assumed to occur 100% of the time for μ^+ and 25% of the time for μ^-, based on the $\mu^\pm$ capture probability on ^{40}Ar.

In the oscillation analysis, 18 nuisance parameters are included, with detector performance parameters correlated between beam and atmospheric data. In all cases, $\sin^2\theta_{12}$, $\Delta m^2 = 1/2(\Delta m^2_{32} + \Delta m^2_{31})$, and Δm^2_{21} are taken to be fixed at the values given in Table 4.10. The fits then range over

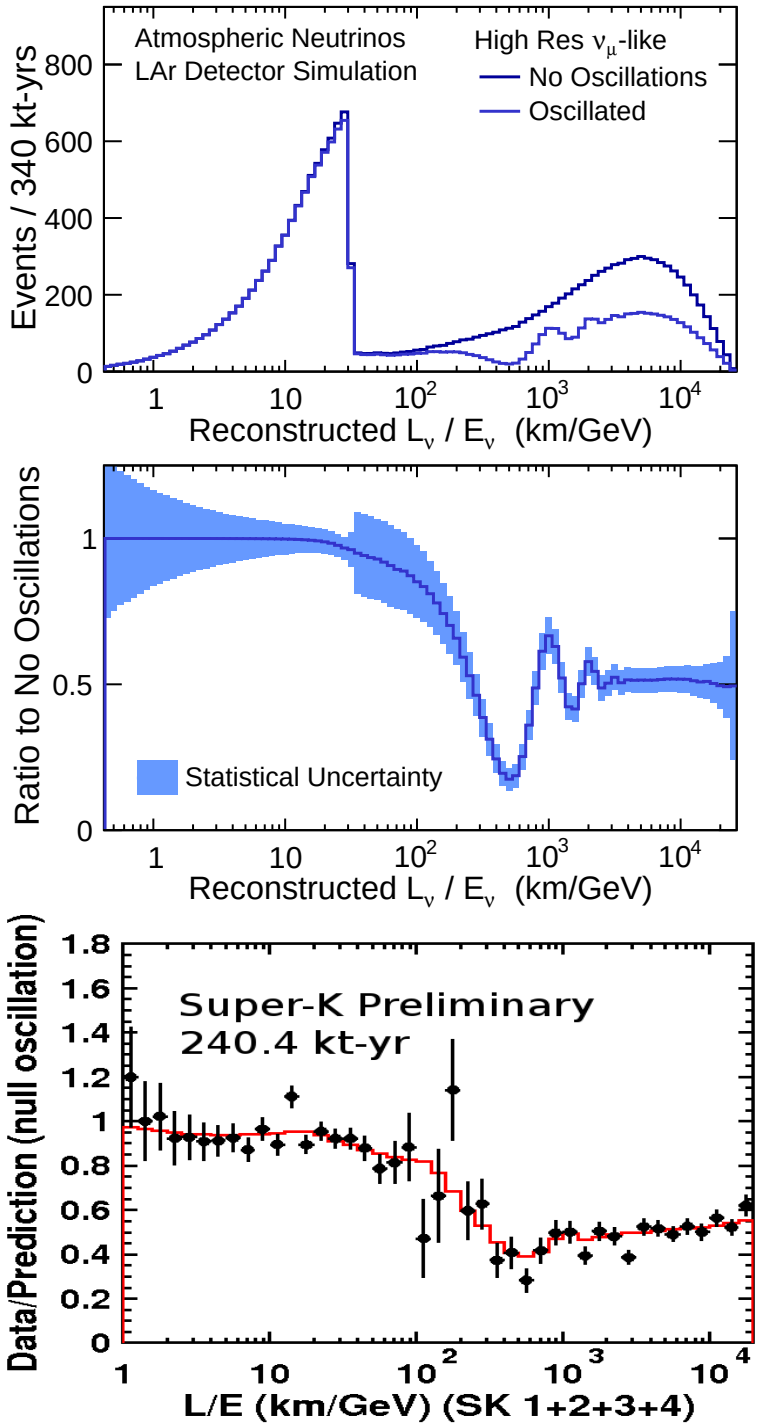

Figure 4.22: Reconstructed L/E distribution of *high-resolution* μ-like atmospheric neutrino events in LBNE with a 340 kt·MW·year exposure with and without oscillations (top); the ratio of the two, with the shaded band indicating the size of the statistical uncertainty (center); the ratio of observed data over the null oscillation prediction from the Super-Kamiokande detector with 240.4 kt · years of exposure (bottom).

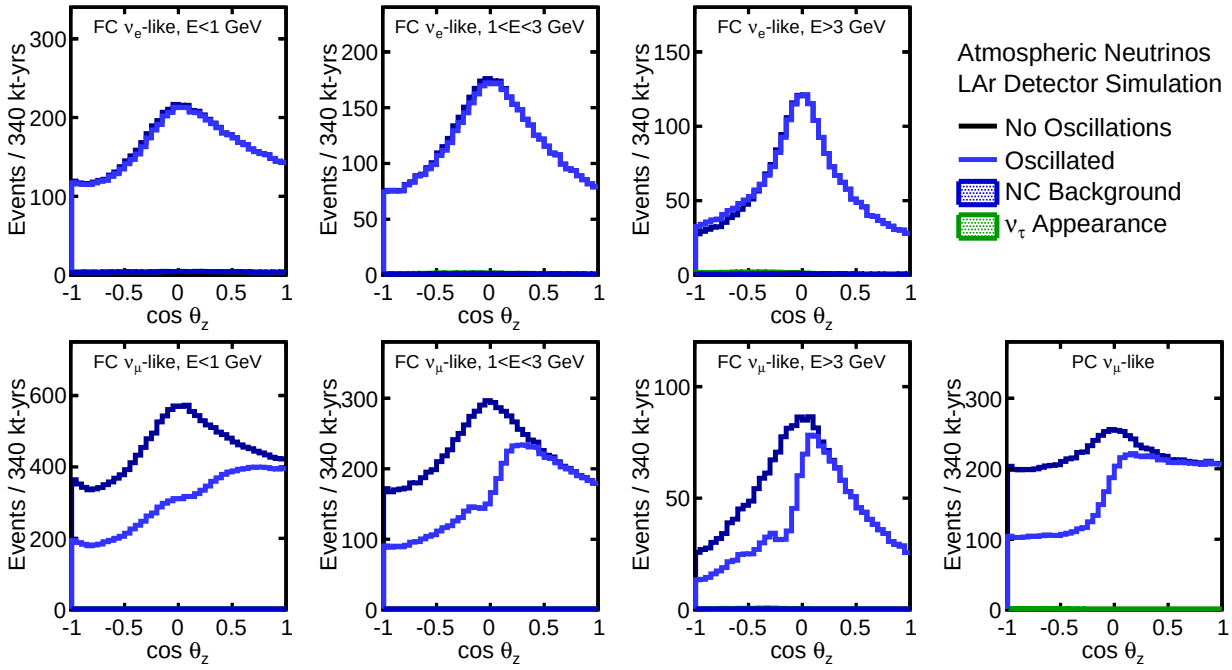

Figure 4.23: Reconstructed zenith angle distributions in several ranges of energy for the FC e-like, FC μ-like, and PC μ-like samples. The small contributions from NC background and ν_τ are also shown.

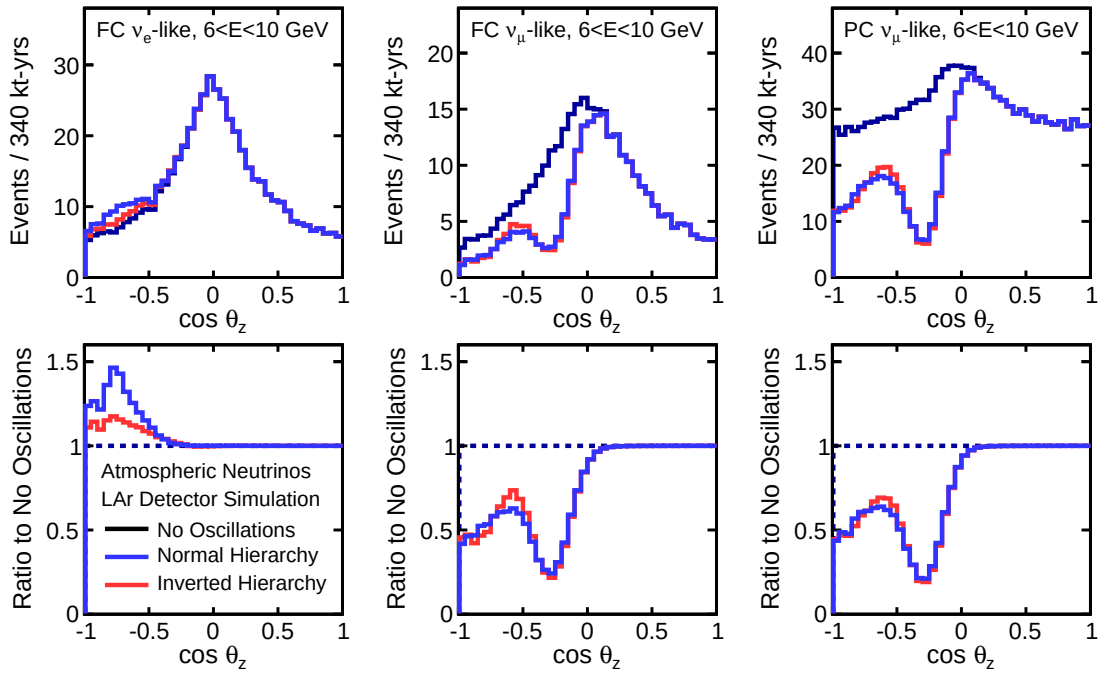

Figure 4.24: Reconstructed zenith angle distributions for 6 to 10-GeV events in the different FC and PC samples. Top plots show the expected distributions for no oscillations (black), oscillations with normal (blue), and inverted (red) hierarchy. Bottom plots show the ratio of the normal and inverted expectations to the no-oscillation distributions for each category.

θ_{23}, θ_{13}, $\delta_{\rm CP}$, and the MH. A 2% constraint is assumed on the value of θ_{13}; this value is chosen to reflect the expected ultimate precision of the current generation of reactor-neutrino experiments. The systematic errors included in this analysis are given in Table 4.14.

Table 4.14: Systematic errors included in the atmospheric and beam+atmospheric neutrino analysis. The beam values assume the existence of a near detector (ND). Atmospheric spectrum ratios include the combined effect of flux and detector uncertainties (e.g., the up/down flux uncertainty as well as the uncertainty on the detector performance for the up/down ratio). The atmospheric spectrum shape uncertainty functions are applied separately for $\nu_\mu, \nu_e, \overline{\nu}_\mu, \overline{\nu}_e$.

	Atmospheric	Beam (Assumes ND)
Normalization	Overall (15%)	μ-like (5%) e-like (1%)
NC Background	e-like (10%)	μ-like (10%) e-like (5%)
Spectrum Ratios	up/down (2%) ν_e/ν_μ (2%) $\overline{\nu}_\mu/\nu_\mu$ (5%) $\overline{\nu}_e/\nu_e$ (5%)	
Spectrum Shape	$f(E < E_0) = 1 + \alpha(E - E_0)/E_0$ $f(E > E_0) = 1 + \alpha \log(E/E_0)$ where σ_α=5%	
Energy Scales (Correlated)	Muons (stopping 1%, exiting 5%) Electrons (1%) Hadronic System (5%)	

For the determination of the MH, the $\overline{\Delta\chi^2}$ value is calculated between the best-fit points in the NH and IH where, at each, the nuisance parameters have been marginalized. The sensitivity in the plots that follow is given as $\sqrt{\overline{\Delta\chi^2}}$. Figure 4.25 shows the MH sensitivity from a 340-kt · year exposure of atmospheric neutrino data alone. For all values of the MH and $\delta_{\rm CP}$, the MH can be determined at $\sqrt{\overline{\Delta\chi^2}} > 3$. The resolution depends significantly on the true value of θ_{23}; the sensitivity for three θ_{23} values is shown. The sensitivity depends relatively weakly on the true hierarchy and the true value of $\delta_{\rm CP}$. This is in sharp contrast to the MH sensitivity of the beam, which has a strong dependence on the true value of $\delta_{\rm CP}$. Figure 4.26 shows the MH sensitivity as a function of the fiducial exposure. Over this range of fiducial exposures, the sensitivity goes essentially as the square root of the exposure, indicating that the measurement is not systematics-limited. Figure 4.27 shows the octant and CPV sensitivity from a 340-kt · year exposure of atmospheric neutrino data alone. For the determination of the octant of θ_{23}, the $\overline{\Delta\chi^2}$ value is calculated between the best-fit points in the lower ($\theta_{23} < 45°$) and higher ($\theta_{23} > 45°$) octants, where at each, the nuisance parameters have been marginalized. The discontinuities in the slopes of the octant sensitivity plot are real features, indicating points at which the best fit moves from one hierarchy to the other. For the detection of CP violation, the $\overline{\Delta\chi^2}$ exclusion is similarly computed for $\delta_{\rm CP} = (0, \pi)$.

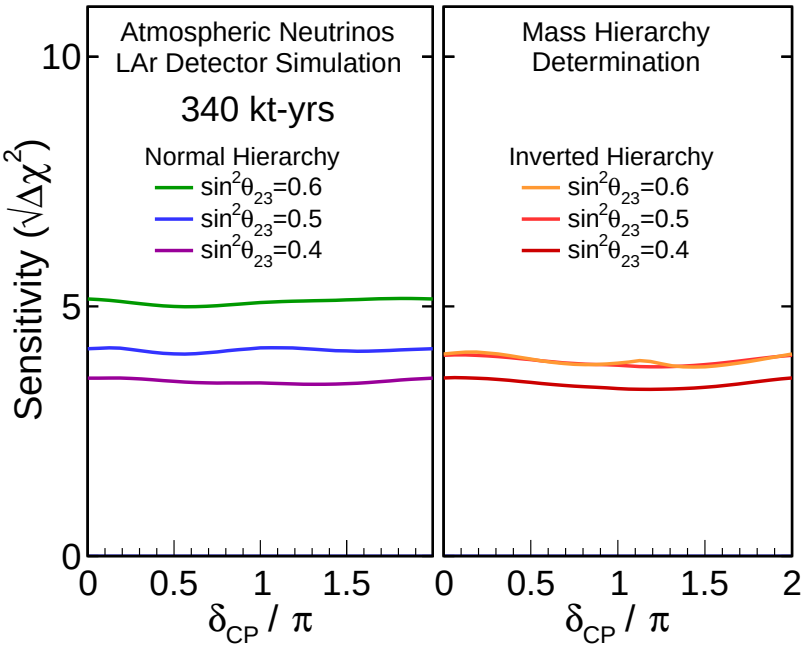

Figure 4.25: Sensitivity of 340 kt · years of atmospheric neutrino data to MH as a function of δ_{CP} for true normal (left) and inverted (right) hierarchy and different assumed values of $\sin^2\theta_{23}$.

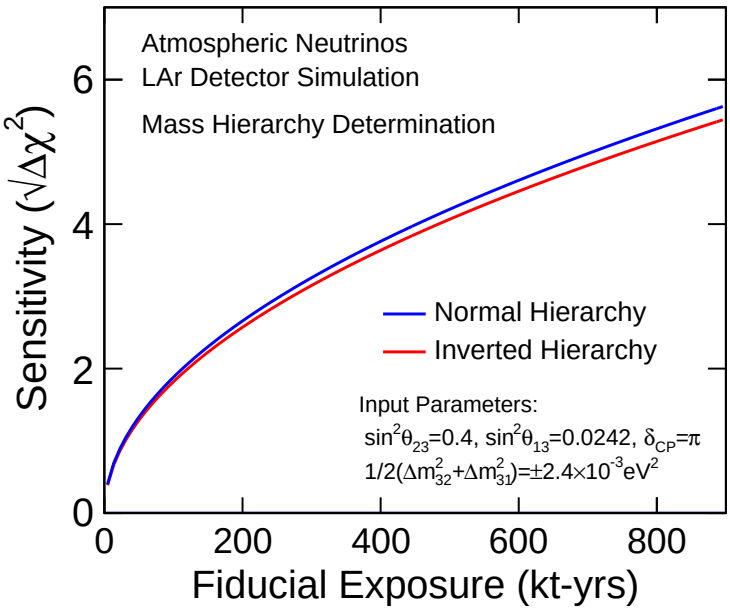

Figure 4.26: Sensitivity to mass hierarchy using atmospheric neutrinos as a function of fiducial exposure in a liquid argon detector.

Figure 4.28 shows the combined sensitivity to beam and atmospheric neutrinos for determination of the MH. This assumes a 10-year run with equal amounts of neutrino and antineutrino running in a 1.2-MW beam.

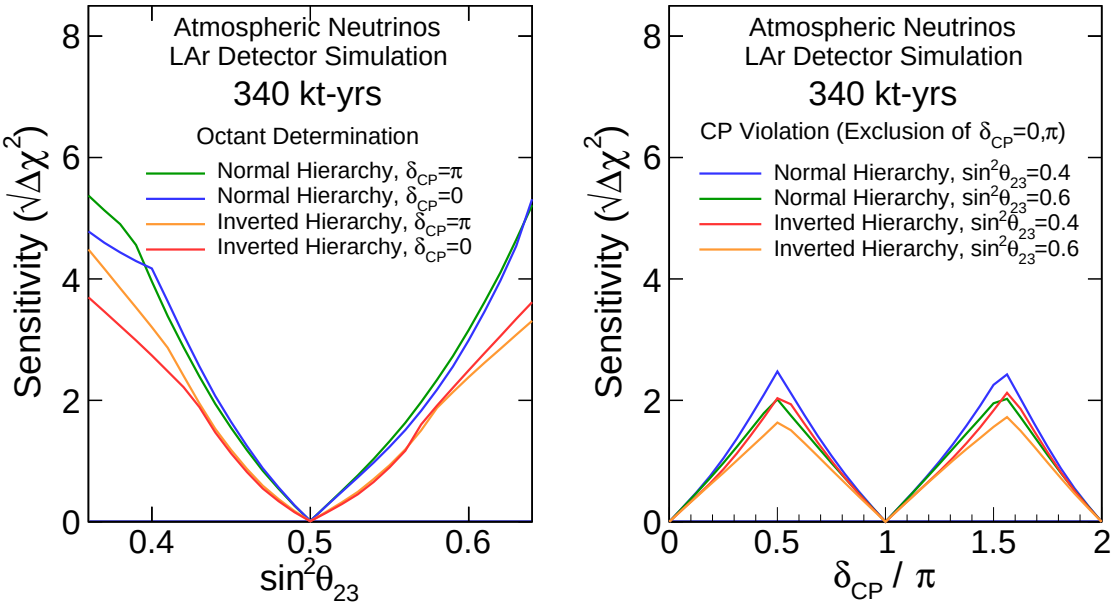

Figure 4.27: Sensitivity to θ_{23} octant (left) and CPV (right) using atmospheric neutrinos.

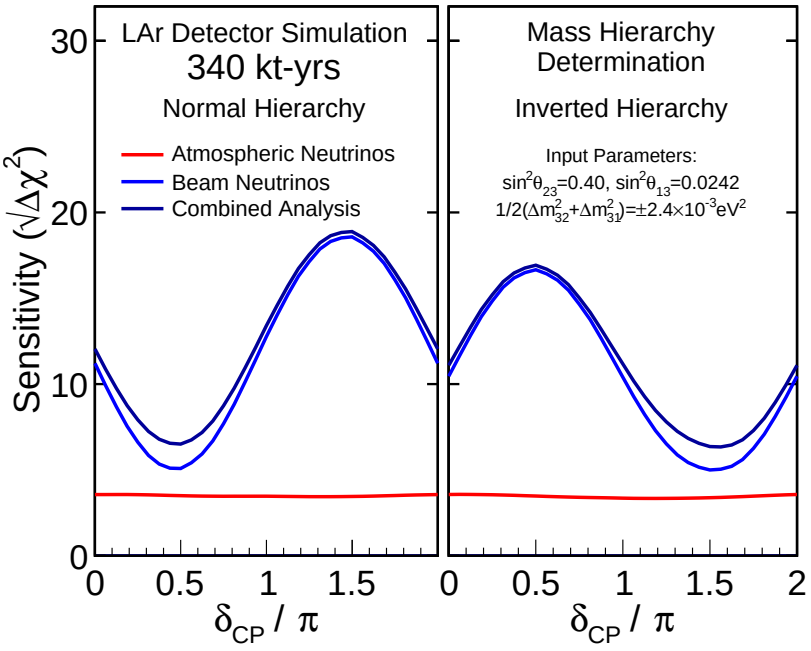

Figure 4.28: Sensitivity to mass hierarchy using atmospheric neutrinos combined with beam neutrinos with an exposure of 340 kt · year in a 1.2-MW beam for normal (left) and inverted (right) hierarchy.

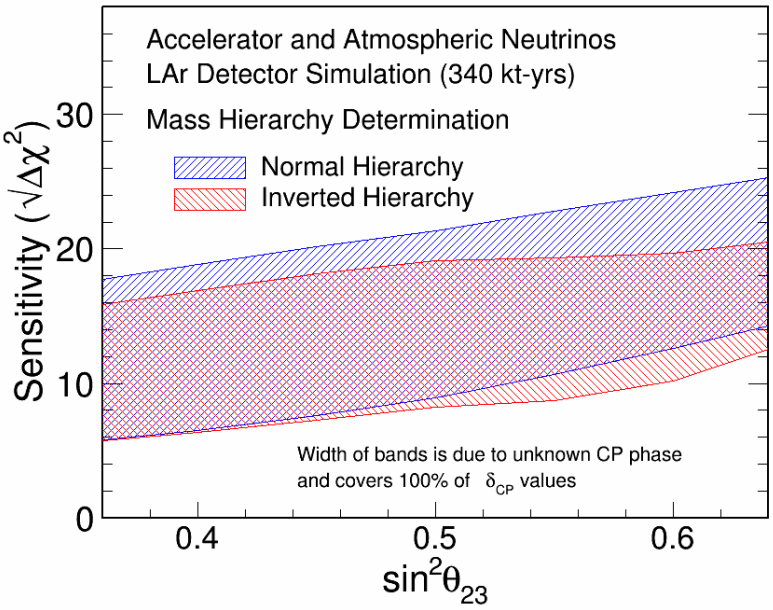

Figure 4.29: Sensitivity to mass hierarchy using atmospheric neutrinos combined with beam neutrinos as a function of the true value of $\sin^2\theta_{23}$, for true normal (blue) and inverted (red) hierarchy. The width of the band is due to the unknown value of $\delta_{\rm CP}$ and covers all possible values of $\delta_{\rm CP}$. Assumes an exposure of 340 kt · year in a 1.2-MW beam.

In the region of $\delta_{\rm CP}$ where the LBNE neutrino-beam-only analysis is least sensitive to the mass hierarchy, atmospheric neutrinos measured in the same experiment offer comparable sensitivity. The combined beam and atmospheric neutrino sensitivity to the mass hierarchy is $|\sqrt{\Delta\chi^2}| > 6$ for all values of $\delta_{\rm CP}$ ($\sin^2\theta_{23} = 0.4$) in a 34-kt detector, assuming a 1.2-MW beam running for ten years. It is important to note that the combined sensitivity is better than the sum of the separate $\Delta\chi^2$ values, as the atmospheric data help to remove degeneracies in the beam data.

Figure 4.29 shows the combined sensitivity to beam and atmospheric neutrinos for determination of MH as a function of the true value of $\sin^2\theta_{23}$, for the same 340-kt · year exposure in a 1.2-MW beam. This can be compared to Figure 4.14 in Section 4.3.3, which shows the same sensitivity using only beam neutrinos.

Figure 4.30 shows the combined sensitivity to beam and atmospheric neutrinos for the θ_{23} octant determination and CPV. The role played by atmospheric data in resolving beam-neutrino degeneracies is also clear from considering the combined and beam-only sensitivities in these plots.

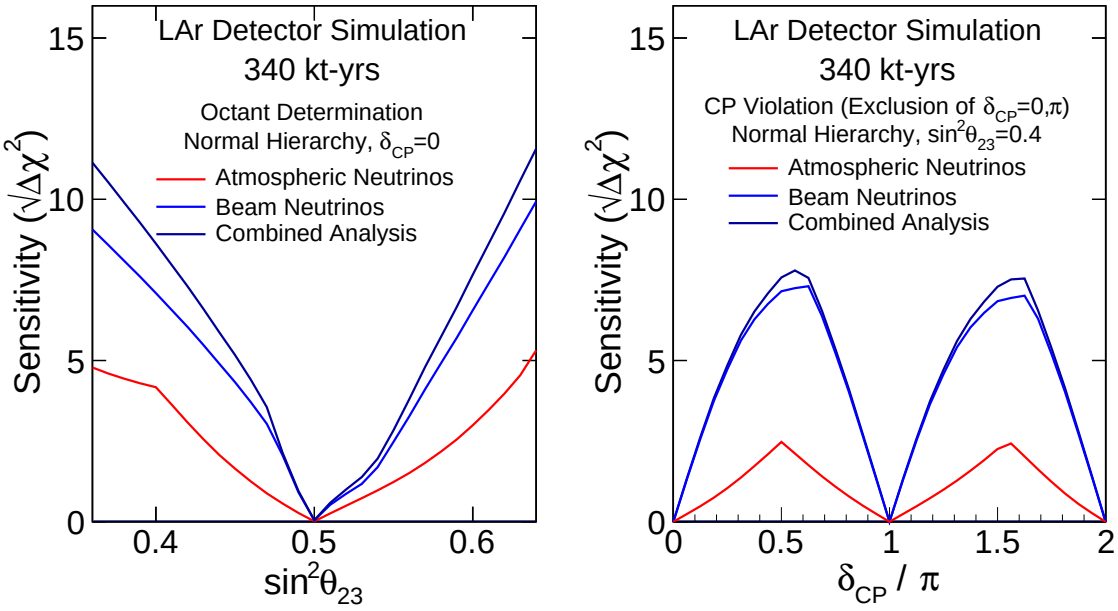

Figure 4.30: Sensitivity to θ_{23} octant (left) and CPV (right) using atmospheric neutrinos combined with beam neutrinos with an exposure of 340 kt · year in a 1.2-MW beam.

4.7 Searches for Physics Beyond the Standard Three-Flavor Neutrino Oscillation Model

Due to the very small masses and large mixing of neutrinos, their oscillations over a long distance act as an exquisitely precise interferometer with high sensitivity to very small perturbations caused by new physics phenomena, such as:

- nonstandard interactions in matter that manifest in long-baseline oscillations as deviations from the three-flavor mixing model
- new long-distance potentials arising from discrete symmetries that manifest as small perturbations on neutrino and antineutrino oscillations over a long baseline
- sterile neutrino states that mix with the three known active neutrino states
- large compactified extra dimensions from String Theory models that manifest through mixing between the Kaluza-Klein states and the three active neutrino states

Full exploitation of LBNE's sensitivity to such new phenomena will require higher-precision predictions of the unoscillated neutrino flux at the far detector and large exposures.

This section explores the potential of the full-scope LBNE design to pursue physics beyond the three-flavor neutrino oscillation model.

4.7.1 Search for Nonstandard Interactions

Neutral current (NC) nonstandard interactions (NSI) can be understood as nonstandard matter effects that are visible only in a far detector at a sufficiently long baseline. They can be parameterized as new contributions to the MSW matrix in the neutrino-propagation Hamiltonian:

$$H = U \begin{pmatrix} 0 & & \\ & \Delta m^2_{21}/2E & \\ & & \Delta m^2_{31}/2E \end{pmatrix} U^\dagger + \tilde{V}_{\rm MSW}\,, \tag{4.10}$$

with

$$\tilde{V}_{\rm MSW} = \sqrt{2} G_F N_e \begin{pmatrix} 1+\epsilon^m_{ee} & \epsilon^m_{e\mu} & \epsilon^m_{e\tau} \\ \epsilon^{m*}_{e\mu} & \epsilon^m_{\mu\mu} & \epsilon^m_{\mu\tau} \\ \epsilon^{m*}_{e\tau} & \epsilon^{m*}_{\mu\tau} & \epsilon^m_{\tau\tau} \end{pmatrix} \tag{4.11}$$

Here, U is the leptonic mixing matrix, and the ϵ-parameters give the magnitude of the NSI relative to standard weak interactions. For new physics scales of a few hundred GeV, a value of $|\epsilon| \lesssim 0.01$ is expected [51,52,53]. LBNE's 1,300-km baseline provides an advantage in the detection of NSI relative to existing beam-based experiments with shorter baselines. Only atmospheric-neutrino experiments have longer baselines, but the sensitivity of these experiments to NSI is limited by systematic effects.

To assess the sensitivity of LBNE to NC NSI, the NSI discovery reach is defined in the following way: the expected event spectra are simulated using GLoBeS, assuming *true* values for the NSI parameters, and a fit is then attempted assuming no NSI. If the fit is incompatible with the simulated data at a given confidence level, the chosen *true* values of the NSI parameters are considered to be within the experimental discovery reach. In Figure 4.31, the NSI discovery reach of LBNE is shown; only one of the $\epsilon^m_{\alpha\beta}$ parameters at a time is taken to be non-negligible.

4.7.2 Search for Long-Range Interactions

The small scale of neutrino-mass differences implies that minute differences in the interactions of neutrinos and antineutrinos with currently unknown particles or forces may be detected through perturbations to the time evolution of the flavor eigenstates. The longer the experimental baseline, the higher the sensitivity to a new long-distance potential acting on neutrinos. For example, some of the models for such long-range interactions (LRI) as described in [54] (Figure 4.32) could contain discrete symmetries that stabilize the proton and give rise to a dark-matter candidate particle, thus providing new connections between neutrino, proton decay and dark matter experiments. The

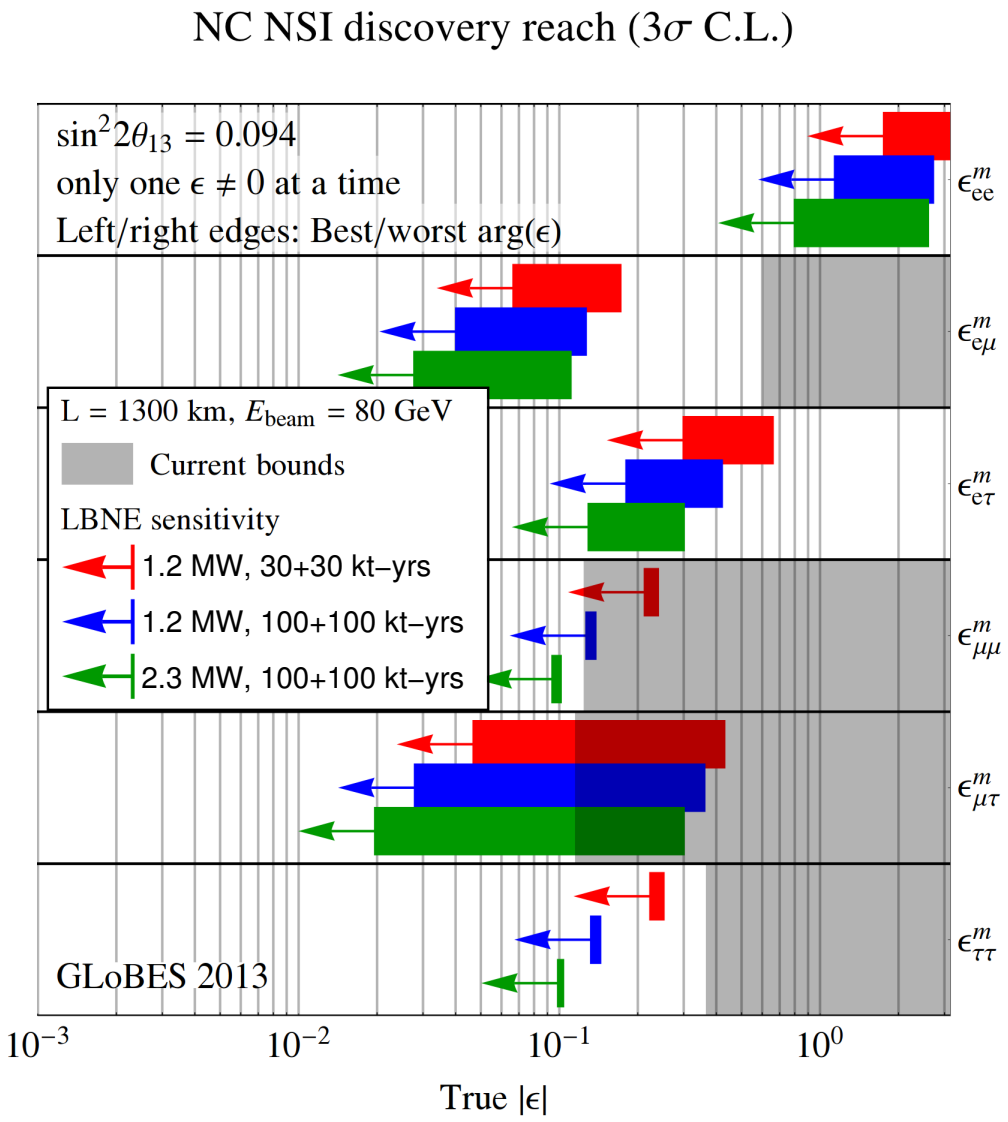

Figure 4.31: Nonstandard interaction discovery reach in LBNE with increasing exposure: 1.2 MW, 60 kt·years (red) + 1.2 MW, 200 kt · year (blue) + 2.3 MW, 200 kt · year (green). The left and right edges of the error bars correspond to the most favorable and the most unfavorable values for the complex phase of the respective NSI parameters. The gray shaded regions indicate the current model-independent limits on the different parameters at 3σ [51,52]. For this study the value of $\sin^2 2\theta_{13}$ was assumed to be 0.09. Figure courtesy of Joachim Kopp.

longer baseline of LBNE improves the sensitivity to LRI beyond that possible with the current generation of long-baseline neutrino experiments. The sensitivity will be determined by the amount of $\nu_\mu/\overline{\nu}_\mu$-CC statistics accumulated and the accuracy with which the unoscillated and oscillated ν_μ spectra can be determined.

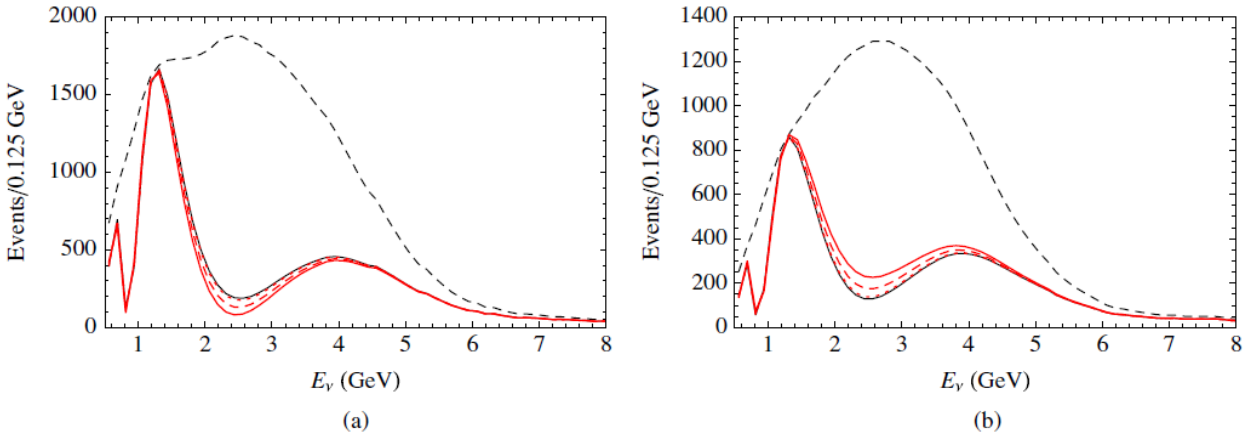

Figure 4.32: Long-range interactions in LBNE. The number of (a) neutrino and (b) antineutrino events versus E_ν, in a long-baseline experiment with a 1,300-km baseline. The unoscillated case (top black dashed curves) and the case of no new physics (thin black solid curves) are displayed, as well as the cases with $\alpha' = (1.0, 0.5, \text{and } 0.1) \times 10^{-52}$, corresponding to red solid, dashed, and dotted curves, respectively. α' is the *fine structure constant* of such interactions, which is constrained to be $\alpha' \leq 10^{-47}$ [54].

4.7.3 Search for Mixing between Active and Sterile Neutrinos

Searches for evidence of active-sterile neutrino mixing at LBNE can be conducted by examining the NC event rate at the far detector and comparing it to a precise estimate of the expected rate extrapolated from ν_μ flux measurements from the near detector and from beam and detector simulations. Observed deficits in the NC rate could be evidence for mixing between the active neutrino states and unknown sterile neutrino states. The most recent such search in a long-baseline experiment was conducted by the MINOS experiment [55].

LBNE will provide a unique opportunity to revisit this search with higher precision over a large range of neutrino energies and a longer baseline. The expected rate of NC interactions with visible energy > 0.5 GeV in a 10-kt detector over three years is approximately 2,000 events (Table 4.1) in the low-energy beam tune and 3,000 events in the medium-energy beam tune. The NC identification efficiency is high, with a low rate of ν_μ-CC background misidentification as shown in Table 4.2. The high-resolution LArTPC far detector will enable a coarse measurement of the incoming neutrino energy in a NC interaction by using the event topology and correcting for the missing energy of the invisible neutrino. This will greatly improve the sensitivity of LBNE to active-sterile mixing as compared to current long-baseline experiments such as MINOS+ since both the energy spectrum and the rate of NC interactions can be measured at both near and far detectors. Studies are currently underway to quantify LBNE's sensitivity to active-sterile mixing.

4.7.4 Search for Large Extra Dimensions

Several theoretical models propose that right-handed neutrinos propagate in large compactified extra dimensions, whereas the standard left-handed neutrinos are confined to the four-dimensional brane [56]. Mixing between the right-handed *Kaluza-Klein* modes and the standard neutrinos would change the mixing patterns predicted by the three-flavor model. The effects could manifest, for example, as distortions in the disappearance spectrum of ν_μ. The rich oscillation structure visible in LBNE, measured with its high-resolution detector using both beam and atmospheric oscillations, could provide further opportunities to probe for this type of new physics. Studies are underway to understand the limits that LBNE could impose relative to current limits and those expected from other experiments.

4.8 Comparison of LBNE Sensitivities to other Proposed Experiments

With tight control of systematics, LBNE will reach 5σ sensitivity to CP violation for a large fraction of $\delta_{\rm CP}$ values. LBNE delivers the best resolution of the value of $\delta_{\rm CP}$ with the lowest combination of power-on-target and far detector mass when compared to other future proposed neutrino oscillation experiments (Figure 4.33).

In Figure 4.33, the CP-violation sensitivity of LBNE is compared to that of other proposed neutrino oscillation experiments from an *independent study* with updated LBNE input based on [57]. The dashed black curve labeled "2020" is the expected sensitivity from the current generation of experiments that could be achieved by 2020. "LBNE-Full" represents a 34-kt LArTPC running in a 1.2-MW beam for 3 (ν) +3 ($\overline{\nu}$) years. "LBNE-PX" is LBNE staged with PIP-II and further upgraded beams with power up to 2.0 MW as shown in Figure 4.17. "T2HK" is a 560-kt (fiducial mass) water Cherenkov detector running in a 1.66-MW beam for 1.5 (ν) + 3.5 ($\overline{\nu}$) years [58]. "LBNO_{100}" is a 100-kt LArTPC at a baseline of 2,300 km running in a 0.8-MW beam from CERN for 5 (ν) + 5 ($\overline{\nu}$) years [59]. "IDS-NF" is the Neutrino Factory with a neutrino beam generated from muon decays in a 10-GeV muon storage ring produced from a 4-MW, 8-GeV Project X proton beam coupled with 100-kt magnetized iron detectors at a baseline of 2,000 km for 10 ($\nu + \overline{\nu}$) simultaneously) [60]. LBNE can reach 5σ sensitivity to CP violation for a large fraction of $\delta_{\rm CP}$ values with the lowest combination of power-on-target and far detector mass when compared to current and future proposed neutrino oscillation experiments.

Alone, LBNE can potentially reach a precision on $\delta_{\rm CP}$ between roughly 6° and 10°, i.e., close to the 4° CKM precision on $\delta_{\rm CP}^{\rm CKM}$ — but an exposure of $\sim$700 kt $\cdot$ MW $\cdot$ years is needed. Nevertheless, as shown in Figure 4.34, wide-band, long-baseline experiments such as LBNE (and LBNO) can

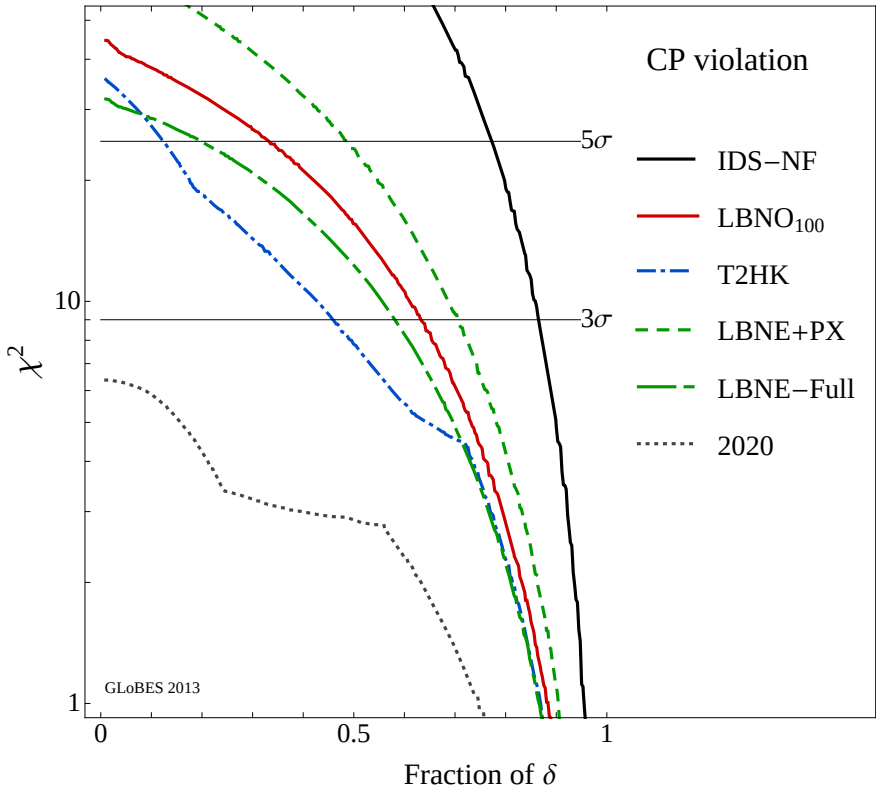

Figure 4.33: The minimal CP-violation sensitivity for a given fraction of $\delta_{\rm CP}$ values for different proposed neutrino oscillation experiments. The exposure and baseline of each experiment is described in the text. Figure is based on the studies detailed in [57].

achieve nearly CKM precision on $\delta_{\rm CP}$ with much less exposure than is required for existing experiments such as NOνA, T2K and proposed short-baseline, off-axis experiments such as T2HK. With the exception of the NuMAX sensitivity, which is taken from [61], the resolutions in the colored bands in Figure 4.34 are calculated independently by LBNE using GLoBES and found to be in good agreement with the values reported by the experiments themselves (T2HK [62], NOνA [63], LBNO [64]).

It is important to note that the precision on $\delta_{\rm CP}$ in the off-axis experiments shown in Figure 4.34 assumes the mass hierarchy (MH) is resolved. If the MH is unknown, the resolution of T2K, NOνA and T2HK will be much poorer than indicated. LBNE does not require external information on the MH to reach the precisions described in this section. Only a neutrino factory can possibly outperform a wide-band, long-baseline experiment — but not by much — for equivalent power, target mass and years of running. To achieve this precision, however, LBNE will need to tightly control the systematic uncertainties on the ν_e appearance signal. Its high-resolution near detector will enable it to reach this level of precision, as described in Section 3.5.

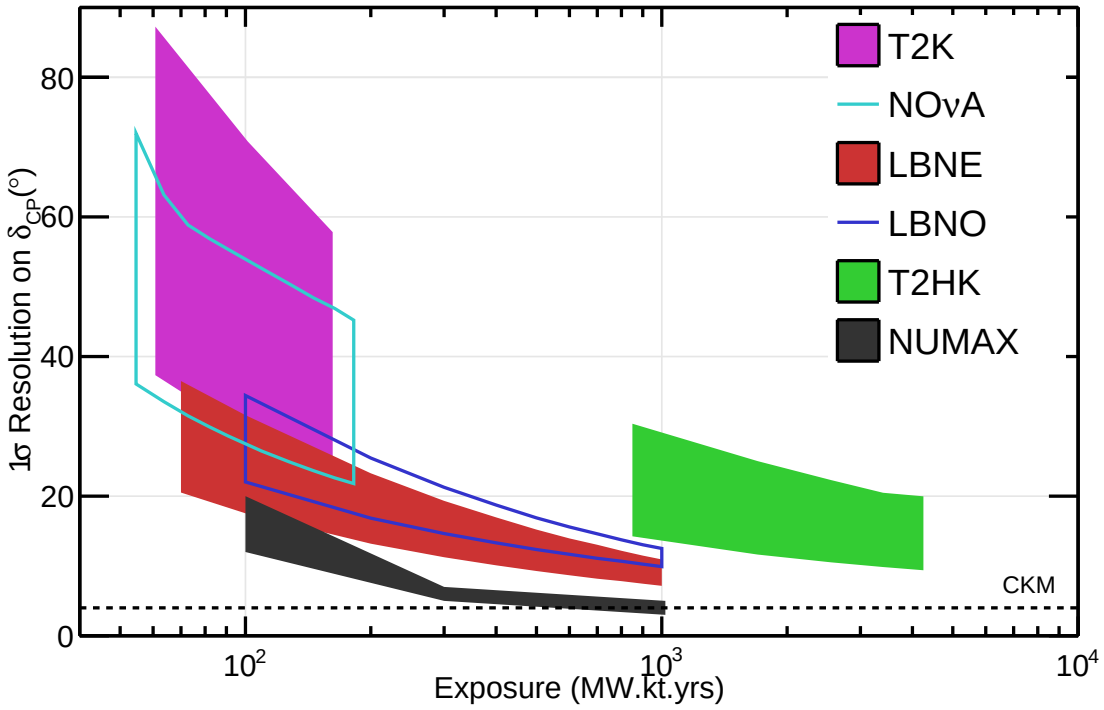

Figure 4.34: The 1σ resolution on $\delta_{\rm CP}$ that can be achieved by existing and proposed beamline neutrino oscillation experiments as a function of exposure in terms of mass $\times$ beam power $\times$ years of running. The band represents the variation in the resolution as a function of $\delta_{\rm CP}$ with the lower edge representing the best resolution and the upper edge the worst. The bands start and stop at particular milestones. For example, the LBNE band starts with the resolutions achieved by the 10-kt LBNE and ends with the full-scope LBNE running with the 2.3-MW upgrades beyond PIP-II. With the exception of the NuMAX sensitivity, which is taken from [61], the resolutions in the colored bands are calculated independently by LBNE using GLoBES. The dashed line denotes the 4° resolution point which is the resolution of $\delta_{\rm CP}^{\rm CKM}$ from the 2011 global fits.

An independent study comparing LBNE's sensitivity to the mass ordering to that of current and future proposed experiments highlights its potential [29]. The study uses frequentist methods of hypothesis testing to define sensitivities. The validity of the approach is tested using toy MC simulations of the various experiments. The comparison of expected MH sensitivities for a variety of current and proposed experiments using different approaches with reasonable estimates as to the start time of the different experiments is summarized in Figure 4.35.

Future upgrades to the Fermilab accelerator complex — in particular the prospect of high-power, low-energy proton beams such as the 3-MW, 8-GeV beam originally proposed as Stage 4 of Project X — could open up further unique opportunities for LBNE to probe CP violation using on-axis, low-energy beams specifically directed at the second oscillation maximum where CP effects dominate the asymmetries [65]. Such high-power, low-energy beams could even enable studies in ν_1-ν_2 mixing in very long-baseline experiments.

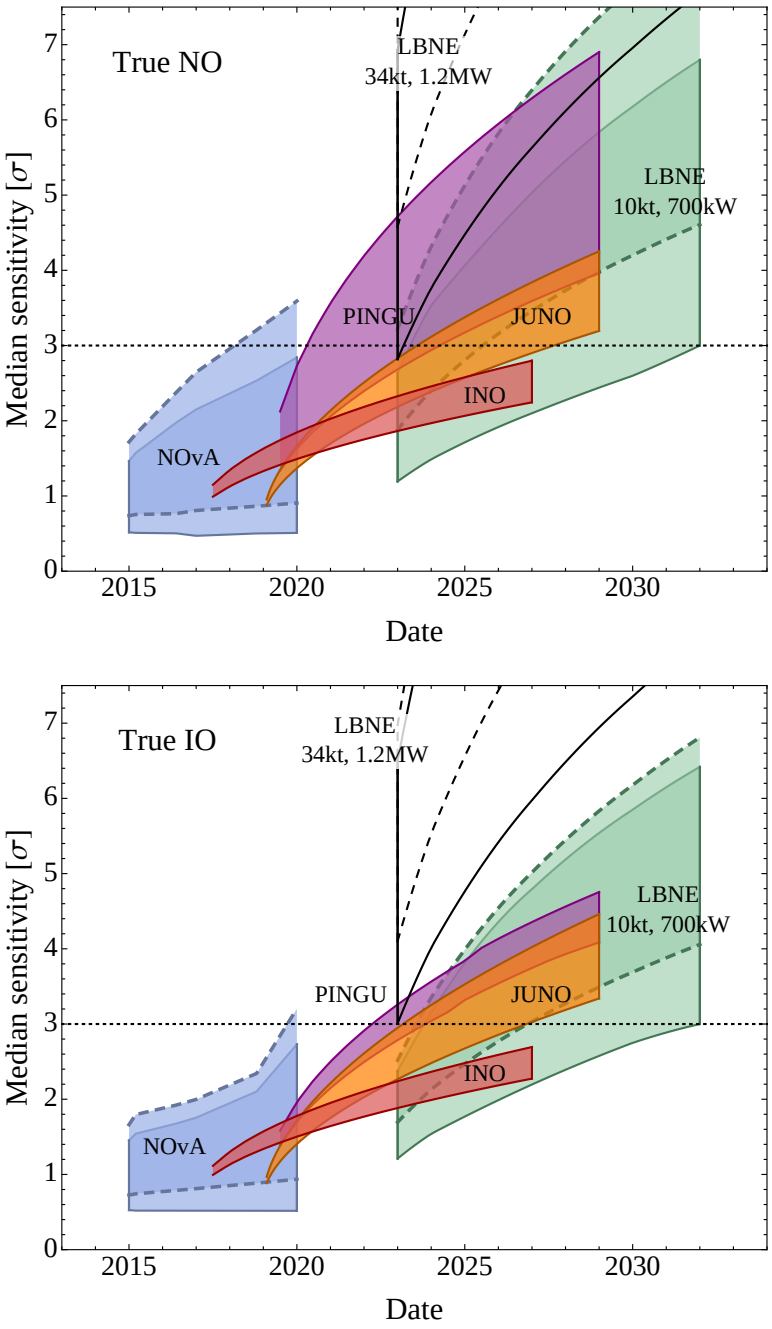

Figure 4.35: The top (bottom) figure shows the median sensitivity in number of sigmas for rejecting the inverted (normal) hierarchy if the normal (inverted) hierarchy is true for different facilities as a function of the date. The width of the bands corresponds to different true values of the CP phase $\delta_{\rm CP}$ for NOνA and LBNE, different true values of θ_{23} between 40° and 50° for INO and PINGU, and energy resolution between $3\%/\sqrt{E\ (\mathrm{MeV})}$ and $3.5\%/\sqrt{E\ (\mathrm{MeV})}$ for JUNO. For the long-baseline experiments, the bands with solid (dashed) contours correspond to a true value for θ_{23} of 40° (50°). In all cases, octant degeneracies are fully considered. This figure is from the analysis presented in [29], however, for the plots shown here, the beam power for the full-scope, 34-kt LBNE has been changed to 1.2 MW to reflect the Fermilab PIP-II upgrade plan.

References

1. P. Huber, M. Lindner, and W. Winter, "Simulation of long-baseline neutrino oscillation experiments with GLoBES (General Long Baseline Experiment Simulator)," *Comput.Phys.Commun.* **167** (2005) 195, arXiv:hep-ph/0407333 [hep-ph]. Cited in Sections 4.2 (pg.85), 4.2.1 (pg.86), and 4.2.2 (pg.88).
2. P. Huber, J. Kopp, M. Lindner, M. Rolinec, and W. Winter, "New features in the simulation of neutrino oscillation experiments with GLoBES 3.0: General Long Baseline Experiment Simulator," *Comput.Phys.Commun.* **177** (2007) 432–438, arXiv:hep-ph/0701187 [hep-ph]. Cited in Sections 4.2 (pg.85) and 4.2.2 (pg.88).
3. S. Agostinelli *et al.*, **GEANT4** , "GEANT4: A simulation toolkit," *Nucl. Instrum. Meth.* **A506** (2003) 250–303. Cited in Section 4.2.1 (pg.85).
4. Y. K. Kim *et al.*, "LBNE Reconfiguration: Steering Committee Report," 2012. http://www.fnal.gov/directorate/lbne_reconfiguration/index.shtml. Cited in Section 4.2.1 (pg.86).
5. C. Andreopoulos, **GENIE Collaboration** , "The GENIE neutrino Monte Carlo generator," *Acta Phys.Polon.* **B40** (2009) 2461–2475. Cited in Sections 4.2.1 (pg.88) and 4.6 (pg.122).
6. K. Abe *et al.*, **T2K Collaboration** , "The T2K Experiment," *Nucl.Instrum.Meth.* **A659** (2011) 106–135, arXiv:1106.1238 [physics.ins-det]. Cited in Section 4.2.1 (pg.88).
7. **NuMI-MINOS** . http://www-numi.fnal.gov/. Cited in Section 4.2.1 (pg.88).
8. D. Ayres *et al.*, **NOvA Collaboration** , "The NOvA Technical Design Report," FERMILAB-DESIGN-2007-01, 2007. http://lss.fnal.gov/archive/design/fermilab-design-2007-01.pdf. Cited in Section 4.2.1 (pg.88).
9. A. Rubbia, "LAGUNA-LBNO: Design of an underground neutrino observatory coupled to long baseline neutrino beams from CERN," *J.Phys.Conf.Ser.* **408** (2013) 012006. Cited in Section 4.2.1 (pg.88).
10. J.-P. Delahaye, C. Ankenbrandt, A. Bogacz, S. Brice, A. Bross, *et al.*, "Enabling Intensity and Energy Frontier Science with a Muon Accelerator Facility in the U.S.: A White Paper Submitted to the 2013 U.S. Community Summer Study of the Division of Particles and Fields of the American Physical Society," FERMILAB-CONF-13-307-APC, arXiv:1308.0494 [physics.acc-ph], 2013. Cited in Section 4.2.1 (pg.88).
11. A. Longhin, "Optimization of neutrino beams for underground sites in Europe," arXiv:1206.4294 [physics.ins-det], 2012. Cited in Section 4.2.1 (pg.88).
12. S. Holmes, R. Alber, B. Chase, K. Gollwitzer, D. Johnson, *et al.*, "Project X: Accelerator Reference Design," FERMILAB-TM-2557, BNL-101116-2013-BC-81834, JLAB-ACP-13-1725, PNNL-22523, SLAC-R-1020, UASLP-IF-13-001, arXiv:1306.5022 [physics.acc-ph], 2013. Cited in Section 4.2.1 (pg.88).

13. **LBNE Project Management Team** , "LBNE Conceptual Design Report, Volume 1: The LBNE Project," LBNE-doc-5235, 2012. Cited in Sections 4.2.2 (pg.88), 4.3 (pg.92), 4.3 (pg.95), and 4.6 (pg.124).
14. S. Amoruso *et al.*, **ICARUS Collaboration** , "Measurement of the mu decay spectrum with the ICARUS liquid argon TPC," *Eur.Phys.J.* **C33** (2004) 233–241, arXiv:hep-ex/0311040 [hep-ex]. Cited in Sections 4.2.2 (pg.88) and 4.6 (pg.124).
15. T2K Collaboration, "A Proposal for a Detector 2km Away from the T2K Neutrino Source.". 2005. http://www.phy.duke.edu/~cwalter/nusag-members/2km-proposal-05-05-30.pdf. Cited in Section 4.2.2 (pg.88).
16. A. Ankowski *et al.*, **ICARUS Collaboration** , "Measurement of through-going particle momentum by means of multiple scattering with the ICARUS T600 TPC," *Eur.Phys.J.* **C48** (2006) 667–676, arXiv:hep-ex/0606006 [hep-ex]. Cited in Section 4.2.2 (pg.88).
17. G. Fogli, E. Lisi, A. Marrone, D. Montanino, A. Palazzo, *et al.*, "Global analysis of neutrino masses, mixings and phases: entering the era of leptonic CP violation searches," *Phys.Rev.* **D86** (2012) 013012, arXiv:1205.5254 [hep-ph]. Cited in Sections 4.3 (pg.92), 4.3 (pg.93), 4.3.2 (pg.110), and 4.4 (pg.117).
18. **LBNE Project Management Team** , "LBNE Conceptual Design Report, Volume 2: The Beamline at the Near Site," LBNE-doc-4317, 2012. Cited in Section 4.3 (pg.93).
19. F. An *et al.*, **Daya Bay Collaboration** , "Spectral measurement of electron antineutrino oscillation amplitude and frequency at Daya Bay," arXiv:1310.6732 [hep-ex], 2013. Cited in Sections 4.3 (pg.93) and 4.5 (pg.119).
20. P. Adamson *et al.*, **MINOS Collaboration** , "Electron neutrino and antineutrino appearance in the full MINOS data sample," *Phys.Rev.Lett.* **110** no. 17, (2013) 171801, arXiv:1301.4581 [hep-ex]. Cited in Sections 4.3 (pg.93), 4.3.2 (pg.103), and 4.3.2 (pg.108).
21. M. J. Murtagh, **E734 Collaboration** , "A Search for muon-neutrino to electron-neutrino oscillations using the E734 detector," BNL-39667, 1987.
22. R. Seto, "BNL E776: A Search for neutrino oscillations," *AIP Conf.Proc.* **176** (1988) 957–963.
23. L. Borodovsky, C. Chi, Y. Ho, N. Kondakis, W.-Y. Lee, *et al.*, "Search for muon-neutrino oscillations muon-neutrino to electron-neutrino (anti-muon-neutrino to anti-electron-neutrino in a wide band neutrino beam," *Phys.Rev.Lett.* **68** (1992) 274–277.
24. P. Astier *et al.*, **NOMAD Collaboration** , "Search for nu(mu) –> nu(e) oscillations in the NOMAD experiment," *Phys.Lett.* **B570** (2003) 19–31, arXiv:hep-ex/0306037 [hep-ex].
25. A. Aguilar-Arevalo *et al.*, **MiniBooNE Collaboration** , "Unexplained Excess of Electron-Like Events From a 1-GeV Neutrino Beam," *Phys.Rev.Lett.* **102** (2009) 101802, arXiv:0812.2243 [hep-ex].

26. A. Aguilar-Arevalo *et al.*, **MiniBooNE Collaboration** , "Improved Search for $\overline{\nu_\mu} \to \overline{\nu_e}$ Oscillations in the MiniBooNE Experiment," *Phys.Rev.Lett.* **110** no. 16, (2013) 161801, arXiv:1207.4809 [hep-ex].
27. K. Abe *et al.*, **T2K Collaboration** , "Observation of Electron Neutrino Appearance in a Muon Neutrino Beam," arXiv:1311.4750 [hep-ex], 2013. Cited in Section 4.3.2 (pg.103).
28. X. Qian, A. Tan, W. Wang, J. Ling, R. McKeown, *et al.*, "Statistical Evaluation of Experimental Determinations of Neutrino Mass Hierarchy," *Phys.Rev.* **D86** (2012) 113011, arXiv:1210.3651 [hep-ph]. Cited in Sections 4.3.1 (pg.96), 4.3.1 (pg.97), 4.3.1 (pg.99), and 4.3.1 (pg.100).
29. M. Blennow, P. Coloma, P. Huber, and T. Schwetz, "Quantifying the sensitivity of oscillation experiments to the neutrino mass ordering," arXiv:1311.1822 [hep-ph], 2013. Cited in Sections 4.3.1 (pg.97), 4.3.1 (pg.98), 4.3.1 (pg.99), 4.3.1 (pg.100), and 4.8 (pg.137).
30. R. Cousins, "Private communication," 2013. Cited in Section 4.3.1 (pg.99).
31. R. Cousins, J. Mumford, J. Tucker, and V. Valuev, "Spin discrimination of new heavy resonances at the LHC," *JHEP* **0511** (2005) 046. Cited in Section 4.3.1 (pg.99).
32. F. Capozzi, G. Fogli, E. Lisi, A. Marrone, D. Montanino, *et al.*, "Status of three-neutrino oscillation parameters, circa 2013," arXiv:1312.2878 [hep-ph], 2013. Cited in Sections 4.3.1 (pg.99), 4.3.3 (pg.112), and 4.4 (pg.115).
33. P. Adamson *et al.*, **MINOS Collaboration** , "Improved search for muon-neutrino to electron-neutrino oscillations in MINOS," *Phys.Rev.Lett.* **107** (2011) 181802, arXiv:1108.0015 [hep-ex]. Cited in Section 4.3.2 (pg.103).
34. P. Adamson *et al.*, **MINOS Collaboration** , "Neutrino and Antineutrino Inclusive Charged-current Cross Section Measurements with the MINOS Near Detector," *Phys.Rev.* **D81** (2010) 072002, arXiv:0910.2201 [hep-ex]. Cited in Section 4.3.2 (pg.103).
35. Q. Wu *et al.*, **NOMAD Collaboration** , "A Precise measurement of the muon neutrino-nucleon inclusive charged current cross-section off an isoscalar target in the energy range 2.5 < E(nu) < 40-GeV by NOMAD," *Phys.Lett.* **B660** (2008) 19–25, arXiv:0711.1183 [hep-ex]. Cited in Section 4.3.2 (pg.103).
36. V. Lyubushkin *et al.*, **NOMAD Collaboration** , "A Study of quasi-elastic muon neutrino and antineutrino scattering in the NOMAD experiment," *Eur.Phys.J.* **C63** (2009) 355–381, arXiv:0812.4543 [hep-ex]. Cited in Section 4.3.2 (pg.103).
37. A. Bodek, U. Sarica, K. Kuzmin, and V. Naumov, "Extraction of Neutrino Flux with the Low ν Method at MiniBooNE Energies," *AIP Conf.Proc.* **1560** (2013) 193–197, arXiv:1207.1247 [hep-ex]. Cited in Section 4.3.2 (pg.103).
38. P. Adamson *et al.*, **MINOS Collaboration** , "A Study of Muon Neutrino Disappearance Using the Fermilab Main Injector Neutrino Beam," *Phys.Rev.* **D77** (2008) 072002, arXiv:0711.0769 [hep-ex]. Cited in Section 4.3.2 (pg.103).
39. M. Bishai, "Determining the Neutrino Flux from Accelerator Neutrino Beams," *Nucl.Phys.Proc.Suppl.* **229-232** (2012) 210–214. Cited in Section 4.3.2 (pg.103).

40. B. Osmanov, **MINERvA Collaboration** , "MINERvA Detector: Description and Performance," arXiv:1109.2855 [physics.ins-det], 2011. Cited in Section 4.3.2 (pg.104).
41. A. Korzenev, **NA61/SHINE** , "Hadron production measurement from NA61/SHINE," arXiv:1311.5719 [nucl-ex], 2013. Cited in Section 4.3.2 (pg.104).
42. P. Adamson *et al.*, **MINOS Collaboration** , "Measurement of the neutrino mass splitting and flavor mixing by MINOS," *Phys.Rev.Lett.* **106** (2011) 181801, arXiv:1103.0340 [hep-ex]. Cited in Sections 4.3.2 (pg.105) and 4.5 (pg.120).
43. T. Yang, **ArgoNeuT Collaboration** , "New Results from ArgoNeuT," FERMILAB-CONF-13-510-E, arXiv:1311.2096 [hep-ex], 2013. Cited in Section 4.3.2 (pg.107).
44. M. Day and K. S. McFarland, "Differences in Quasi-Elastic Cross-Sections of Muon and Electron Neutrinos," *Phys.Rev.* **D86** (2012) 053003, arXiv:1206.6745 [hep-ph]. Cited in Section 4.3.2 (pg.108).
45. K. Abe *et al.*, **Super-Kamiokande Collaboration** , "Search for Differences in Oscillation Parameters for Atmospheric Neutrinos and Antineutrinos at Super-Kamiokande," *Phys.Rev.Lett.* **107** (2011) 241801, arXiv:1109.1621 [hep-ex]. Cited in Section 4.4 (pg.115).
46. P. Adamson *et al.*, **MINOS Collaboration** , "Measurement of Neutrino and Antineutrino Oscillations Using Beam and Atmospheric Data in MINOS," *Phys.Rev.Lett.* **110** (2013) 251801, arXiv:1304.6335 [hep-ex]. Cited in Section 4.6 (pg.122).
47. V. Agrawal, T. Gaisser, P. Lipari, and T. Stanev, "Atmospheric neutrino flux above 1-GeV," *Phys.Rev.* **D53** (1996) 1314–1323, arXiv:hep-ph/9509423 [hep-ph]. Cited in Section 4.6 (pg.122).
48. A. Ankowski *et al.*, "Energy reconstruction of electromagnetic showers from pi0 decays with the icarus t600 liquid argon tpc," *Acta Physica Polonica B* **41** no. 1, (2010) 103, arXiv:0812.2373 [hep-ex]. Cited in Section 4.6 (pg.124).
49. F. Arneodo *et al.*, **The ICARUS-Milano Collaboration** , "Performance of a liquid argon time projection chamber exposed to the cern west area neutrino facility neutrino beam," *Phys. Rev. D* **74** (Dec, 2006) 112001. http://link.aps.org/doi/10.1103/PhysRevD.74.112001. Cited in Section 4.6 (pg.124).
50. C. Rubbia *et al.*, "Underground operation of the ICARUS T600 LAr-TPC: first results," *JINST* **6** (2011) P07011, arXiv:1106.0975 [hep-ex]. Cited in Section 4.6 (pg.124).
51. S. Davidson, C. Pena-Garay, N. Rius, and A. Santamaria, "Present and future bounds on nonstandard neutrino interactions," *JHEP* **0303** (2003) 011, arXiv:hep-ph/0302093 [hep-ph]. Cited in Section 4.7.1 (pg.132).
52. M. Gonzalez-Garcia and M. Maltoni, "Phenomenology with Massive Neutrinos," *Phys.Rept.* **460** (2008) 1–129, arXiv:0704.1800 [hep-ph]. Cited in Section 4.7.1 (pg.132).

53. C. Biggio, M. Blennow, and E. Fernandez-Martinez, "General bounds on non-standard neutrino interactions," *JHEP* **0908** (2009) 090, arXiv:0907.0097 [hep-ph]. Cited in Section 4.7.1 (pg.132).
54. H. Davoudiasl, H.-S. Lee, and W. J. Marciano, "Long-Range Lepton Flavor Interactions and Neutrino Oscillations," *Phys.Rev.* **D84** (2011) 013009, arXiv:1102.5352 [hep-ph]. Cited in Section 4.7.2 (pg.132).
55. P. Adamson *et al.*, **MINOS Collaboration** , "Search for sterile neutrino mixing in the MINOS long baseline experiment," *Phys.Rev.* **D81** (2010) 052004, arXiv:1001.0336 [hep-ex]. Cited in Section 4.7.3 (pg.134).
56. P. Machado, H. Nunokawa, F. P. d. Santos, and R. Z. Funchal, "Large Extra Dimensions and Neutrino Oscillations," arXiv:1110.1465 [hep-ph], 2011. Cited in Section 4.7.4 (pg.135).
57. P. Coloma, P. Huber, J. Kopp, and W. Winter, "Systematic uncertainties in long-baseline neutrino oscillations for large θ_{13}," *Phys.Rev.* **D87** no. 3, (2013) 033004, arXiv:1209.5973 [hep-ph]. Cited in Section 4.8 (pg.135).
58. K. Abe, T. Abe, H. Aihara, Y. Fukuda, Y. Hayato, *et al.*, "Letter of Intent: The Hyper-Kamiokande Experiment — Detector Design and Physics Potential —," arXiv:1109.3262 [hep-ex], 2011. Cited in Section 4.8 (pg.135).
59. A. Stahl, C. Wiebusch, A. Guler, M. Kamiscioglu, R. Sever, *et al.*, "Expression of Interest for a very long baseline neutrino oscillation experiment (LBNO)," CERN-SPSC-2012-021, SPSC-EOI-007, 2012. Cited in Section 4.8 (pg.135).
60. M. Apollonio, A. Bross, J. Kopp, and K. Long, **IDS-NF Collaboration** , "The International Design Study for the Neutrino Factory," *Nucl.Phys.Proc.Suppl.* **229-232** (2012) 515. Cited in Section 4.8 (pg.135).
61. E. Christensen, P. Coloma, and P. Huber, "Physics Performance of a Low-Luminosity Low Energy Neutrino Factory," arXiv:1301.7727 [hep-ph], 2013. Cited in Section 4.8 (pg.136).
62. E. Kearns *et al.*, **Hyper-Kamiokande Working Group** , "Hyper-Kamiokande Physics Opportunities," arXiv:1309.0184 [hep-ex], 2013. Cited in Section 4.8 (pg.136).
63. M. Messier, **NOvA Collaboration** , "Extending the NOvA Physics Program," FERMILAB-CONF-13-308-E, arXiv:1308.0106 [hep-ex], 2013. Cited in Section 4.8 (pg.136).
64. S. Agarwalla *et al.*, **LAGUNA-LBNO Collaboration** , "The mass-hierarchy and CP-violation discovery reach of the LBNO long-baseline neutrino experiment," arXiv:1312.6520 [hep-ph], 2013. Cited in Section 4.8 (pg.136).
65. M. Bishai, M. Diwan, S. Kettell, J. Stewart, B. Viren, *et al.*, "Precision Neutrino Oscillation Measurements using Simultaneous High-Power, Low-Energy Project-X Beams," BNL-101234-2013-CP, FERMILAB-FN-0962, arXiv:1307.0807 [hep-ex], 2013. Cited in Section 4.8 (pg.137).